

DESIGN OF HIGH-EFFICIENCY DYE-SENSITIZED NANOCRYSTALLINE  
SOLAR CELLS

A THESIS SUBMITTED TO  
THE GRADUATE SCHOOL OF NATURAL AND APPLIED SCIENCES  
OF  
MIDDLE EAST TECHNICAL UNIVERSITY

BY

HALİL İBRAHİM YAVUZ

IN PARTIAL FULFILLMENT OF THE REQUIREMENTS  
FOR  
THE DEGREE OF DOCTOR OF PHILOSOPHY  
IN  
METALLURGICAL AND MATERIALS ENGINEERING

SEPTEMBER 2014



Approval of the thesis:

**DESIGN OF HIGH-EFFICIENCY DYE-SENSITIZED NANOCRYSTALLINE  
SOLAR CELLS**

submitted by **HALİL İBRAHİM YAVUZ** in partial fulfillment of the requirements  
for the degree of **Doctor of Philosophy in Metallurgical and Materials Engineering  
Department, Middle East Technical University** by,

Prof. Dr. Canan Özgen  
Dean, Graduate School of **Natural and Applied Sciences**

\_\_\_\_\_

Prof. Dr. Cemil Hakan Gür  
Head of Department, **Metallurgical and Materials Eng.**

\_\_\_\_\_

Prof. Dr. Ahmet Macit Özenbaş  
Supervisor, **Metallurgical and Materials Eng. Dept., METU**

\_\_\_\_\_

Prof. Dr. A. Çiğdem Erçelebi  
Co-Supervisor, **Physics Dept., METU**

\_\_\_\_\_

**Examining Committee Members:**

Prof. Dr. Raşit Turan  
Physics Dept., METU

\_\_\_\_\_

Prof. Dr. Ahmet Macit Özenbaş  
Metallurgical and Materials Eng. Dept., METU

\_\_\_\_\_

Prof. Dr. Caner Durucan  
Metallurgical and Materials Eng. Dept., METU

\_\_\_\_\_

Prof. Dr. Mahmut Vedat Akdeniz  
Metallurgical and Materials Eng. Dept., METU

\_\_\_\_\_

Assoc. Prof. Dr. Jongee Park  
Metallurgical and Materials Eng. Dept., Atılım University

\_\_\_\_\_

**Date:**

\_\_\_\_\_

**I hereby declare that all information in this document has been obtained and presented in accordance with academic rules and ethical conduct. I also declare that, as required by these rules and conduct, I have fully cited and referenced all material and results that are not original to this work.**

Name, Last name : Halil Ibrahim Yavuz

Signature :

## ABSTRACT

### DESIGN OF HIGH-EFFICIENCY DYE-SENSITIZED NANOCRYSTALLINE SOLAR CELLS

Yavuz, Halil İbrahim

PhD, Department of Metallurgical and Materials Engineering

Supervisor: Prof. Dr. A. Macit Özenbaş

Co-Supervisor: Prof. Dr. A. Çiğdem Erçelebi

September 2014, 140 pages

Nanocrystalline dye sensitized solar cells (DSSC) technology continues to develop as a better alternative to the silicon based solar cells, which are commercialized. This study aims at finding low cost and highly efficient DSSC design and production methods via examination of effects of both photoanode structure and photon-electron generation mechanism on photoanode layers. This will contribute to the commercialization of DSSC technology. Photoanode structure is examined in four groups; transparent conductive glass (TCO), blocking layer (BL), absorber layer (AL) and scattering layer (SL) throughout this study. Firstly, indium doped SnO<sub>2</sub> (ITO) was synthesized by sol-gel method for the use in TCO part of the DSSCs. 4.32% conversion efficiency has been found by using those TCO's in the production of fully sol-gel based DSSCs. For the first time in the literature, 1D ITO structures were synthesized by sol-gel method and this synthesis was used on DSSCs in order to increase the interaction between TCO and AL. However, the commercialized fluorine doped SnO<sub>2</sub> (FTO) TCO's were used instead of ITO based ones in the rest of the study since their charge transport resistances are lower. ZrO<sub>2</sub> BL was found to have superior photovoltaic characteristics in prevention of back transfer reactions. In addition, ZrO<sub>2</sub> BL was found

to protect the conductivity of FTO based TCO's during heat treatment. AL, which is responsible for photon to electron generation, was synthesized using 5% Zr doped TiO<sub>2</sub> nanoparticles. This synthesis was found to have photon to energy conversion efficiency ( $\eta$ ) trice than bare TiO<sub>2</sub> absorber layer. Moreover, adding hydrothermal treatment step to the sol-gel method process was found to increase photon to energy conversion efficiency rate. The scattering layers enable to increase the light absorption ability of DSSC via unused photons scattering back to metal oxide sensitized interface. For this purpose, SL was produced by 10% Zr modified TiO<sub>2</sub> particles. These particles showed better performance rate than traditionally produced scattering layer. As a result of all these analyses, this Thesis found that the modifications made to the photoanode increased DSSC's photovoltaic characteristics. After the modifications 7.45% photon to energy conversion efficiency was obtained.

**Keywords:** Zirconium doped titanium oxide, transparent conductive glass (TCO), 1D ITO structures, blocking layer, absorber layer, scattering layer, dye sensitized solar cell

## ÖZ

### YÜKSEK VERİMLİ BOYA UYARIMLI NANOKRİSTAL GÜNEŞ HÜCRELERİ TASARIMI

Yavuz, Halil İbrahim

Doktora, Metalurji ve Malzeme Mühendisliği Bölümü

Tez Yöneticisi: Prof. Dr. A. Macit Özenbaş

Ortak Tez Yöneticisi: Prof. Dr. A. Çiğdem Erçelebi

Eylül 2014, 140 sayfa

Boya uyarımlı güneş hücreleri (DSSC) teknolojisi, ticari niteliğe sahip silisyum bazlı güneş hücreleri teknolojisine daha iyi bir alternatif olma yönünde gelişmeye devam etmektedir. Bu çalışmada, fotoanot yapısı ve fotoanot katmanlarının herbirinin foton-elektron üretim mekanizması üzerindeki etkilerinin incelenmesi suretiyle düşük maliyetli, yüksek verimli DSSC üretme yöntemlerinin saptanması amaçlanmaktadır. Böylece DSSC'nin ticari nitelik kazanmasına katkı sağlanacaktır. Bu çalışmada fotoanot yapısı; anot iletken cam tabakası (TCO), bloklama tabakası (BL), absorpsiyon tabakası (AL) ve saçılım tabakası (SL) olmak üzere 4 ana grupta incelenmiştir. İndiyum katkılanmış kalay oksit camlar (ITO) DSSC'de kullanılmak üzere sol-jel yöntemiyle sentezlenmiştir. Sol-jel metoduyla, % 4.32 verimli güneş hücresi, bu şekilde sentezlenmiş TCO'lar kullanılarak elde edilmiştir. Bu çalışmada ilk kez, 1D ITO yapıları sol jel yöntemiyle sentezlenmiştir ve bu sentez TCO ve absorpsiyon tabakası (AL) arasındaki etkileşimi artırmak için DSSC'de kullanılmıştır. Bununla birlikte, ticari olan flor katkılanmış kalay oksit camların (FTO) transfer direncinin daha düşük olması nedeniyle, bu camlar TCO olarak bu çalışmanın geri kalan kısmında kullanılmıştır. Bloklama tabakası (BL) ile ilgili çalışmalarda,  $ZrO_2$

BL'nin TCO üzerindeki geri reaksiyonların engellemesinde üstün fotovoltaiik özelliklere sahip olduđu saptanmıřtır. Ayrıca, ZrO<sub>2</sub> BL'nin yüksek sıcaklık altında FTO bazlı TCO iletkenliđini koruyucu bir özelliđi olduđu görülmüřtür. Fotondan güç üretilmesinden sorumlu olan AL'ye iliřkin alıřmalarda %5 Zr'un TiO<sub>2</sub>'ye katkılanmasıyla sentezlenen AL'nin, absorplayıcı tabakasında yalın TiO<sub>2</sub> tabakasına nazaran neredeyse üç kat daha fazla foton enerji çevrim yüzdesine ( $\eta$ ) sahip olduđu tespit edilmiřtir. Ayrıca, bu tabakanın üretiminde kullanılan sol-jel yöntemine hidrotermal basamađın eklenmesinin foton-elektrik çevrimi verimlilik oranını artırdıđı saptanmıřtır. Absorplanmamıř ışını geri çevirerek absorplayıcı tabakanın ışın sođurma özelliđini artıran SL'ye iliřkin alıřmalarda, TiO<sub>2</sub>'ye %10 Zr eklenerek, bu yapı saılım tabakası olarak kullanılmıřtır. Geleneksel yöntemlerle hazırlanan saılım tabakasına oranla daha yüksek verim elde edilmiřtir. Yapılan tüm bu incelemeler neticesinde bu Tez'de, fotoanot üzerinde yapılan modifikasyonların DSSC'nin fotovoltaiik özelliklerini artırdıđı saptanmıřtır. Fotoanot üzerinde yapılan modifikasyonlar sonucunda, %7.45 foton enerji çevrim verimine sahip güneř hücreleri elde edilmiřtir.

**Anahtar Sözcükler:** Zirkonyum katkılanmıř TiO<sub>2</sub>, boya uyarımlı güneř hücresi, yüksek geçirgenlikli iletken camlar, bloklama tabakası, absorpsiyon tabakası, saılım tabakası, 1D ITO yapılar.

*To my family, once again*

*To ıđdem. Until recently, I have not imagined I would add this line for someone*

## ACKNOWLEDGMENTS

I am very grateful to my supervisor Prof. Dr. A. Macit Özenbaş for his guidance and support during this work, and his great attention and patience on me from beginning until the end of my graduation.

It is great pleasure to thank my co-supervisor Prof. Dr. Çiğdem Erçelebi from Physics Department of METU.

I am very grateful to my laboratory colleagues Kerem Cağatay İçli, Murat Güneş and Bahadır Kocaoğlu, Mustafa Burak Çoşar and Berk Akbay, for their support and friendship at every stage of this work and my graduation.

I am very grateful to METU Metallurgical and Materials Engineering Department for all the support provided during this study. I want to thank to İdris Candan from Physics Department of METU and Dogukan Hazar Apaydin from Chemistry Department of METU for characterizations of solar cells. I want also to thank to METU Central Laboratory for their attention during analysis.

I am very grateful to ÖYP financial support during the thesis. This work was also supported by GÜNAM (Center for Solar Energy Research and Applications) at METU.

I want to thank to my family, for their great patience, not only during this work but also at every stage of my life. In addition, I'm sorry for my dad, I wish I had finished before he died.

## TABLE OF CONTENTS

ABSTRACT.....	v
ÖZ.....	vii
ACKNOWLEDGMENTS.....	x
TABLE OF CONTENTS.....	xvi
LIST OF TABLES.....	xvi
LIST OF FIGURES.....	xv
ABBREVIATIONS.....	xvii
CHAPTERS	
1. INTRODUCTION.....	1
REFERENCES.....	7
2. LITERATURE SURVEY.....	11
2.1. Solar Irradiance and Spectrum.....	11
2.2. Basic Structure of a Solar Cell.....	13
2.3. Brief overview on Photovoltaic Technologies and Market.....	15
2.3.1. Wafer Based Solar Cells.....	15
2.3.2. Concentrator Systems.....	16
2.3.3. Thin Film Technologies.....	17
2.3.4. Emerging Technologies.....	18
2.4. Dye Sensitized Solar Cells.....	19
2.4.1. Semiconductor Materials and Properties.....	24
2.4.2 Properties of The Interface of Electrolyte – Semiconductor.....	28

2.4.3 Mesoporous Oxide Films.....	30
2.4.4 Metal Oxides as Blocking Layer.....	32
2.4.5. Sensitizer.....	34
2.4.6. Electrolyte.....	35
2.4.7. Counter Electrode.....	36
REFERENCES.....	42
3. EXPERIMENTAL.....	43
3.1. Particle Synthesis.....	44
3.1.1. Polymerized Complex Combustion Method.....	44
3.1.2. Hydrothermal Modified Sol-gel Techniques.....	44
3.2. Thick Film Deposition.....	45
3.2.1. Preparation of Screen Printing Pastes.....	46
3.2.2. Substrate Cleaning.....	46
3.2.3. Screen Printing of Pastes.....	47
3.2.4. Heat Treatment of Films.....	49
3.2.5. Characterization.....	50
3.3. Electrical Characterizations of Films.....	50
3.4. Assembly of DSSC.....	50
3.4.1. Dye Staining.....	50
3.4.2. Preparation of Counter Electrode.....	51
3.4.3. Assembly and Characterization.....	51
3.5. Impedance Spectroscopy.....	53
REFERENCES.....	59
4. AN ALTERNATIVE PATH OF PRODUCING HIGHLY TRANSPARENT AND LOWER RESISTANCE INDIUM DOPED TIN OXIDE (ITO).....	61
4.1. Motivation of Chapter 4.....	61

4.2. Experimental .....	62
4.2.1. Synthesis of ITO Gel .....	63
4.2.2. Synthesis of ITO Film.....	64
4.2.3. Synthesis of TiO <sub>2</sub> nano Powders .....	64
4.2.4. Fabrication of the Nanocomposite ITO-TiO <sub>2</sub> Dye-sensitized Solar Cell .	64
4.3. Results of Discussion .....	65
4.3.1. ITO Films.....	65
4.4. Conclusion.....	75
REFERENCES.....	77
<b>5. PRODUCTION OF HIGHLY EFFICIENT FULLY SOL-GEL BASED 1D ITO NANO STRUCTURE - TiO<sub>2</sub> NANO POWDER COMPOSITE PHOTOANODE FOR DYE SENSITIZED SOLAR CELL .....</b>	<b>81</b>
5.1. Motivation of Chapter 5 .....	81
5.2.1. Synthesis of ITO gel .....	83
5.2.2. Synthesis of ITO film .....	83
5.2.3. Synthesis of ITO nanopowders.....	84
5.2.4. Synthesis of ITO nanowires.....	84
5.2.4. a. ITO seeding step .....	85
5.2.4. b. Growth Step of ITO Nanowires by Hydrothermal Method.....	85
5.2.5. Synthesis of TiO <sub>2</sub> Nanopowders.....	86
5.2.6. Fabrication of the Nanocomposite ITO-TiO <sub>2</sub> Dye-sensitized Solar Cell .	86
5.3. Results And Discussions .....	87
5.4. Conclusion.....	93
REFERENCES.....	95
<b>6. APPLICATION OF WIDE BAND GAP ZrO<sub>2</sub> BLOCKING LAYER ON DYE SENSITIZED SOLAR CELLS .....</b>	<b>99</b>
6.1. Motivation of Chapter 6 .....	99

6.2. Experimental.....	102
6.2.1. Production of Blocking Layers .....	102
6.2.1. DSSC Cell Production .....	102
6.3. Results and Discussion .....	103
6.3.1. FE-SEM and XPS Analysis of Coated and Uncoated FTO Surfaces .....	103
6.3.3.Uv- Vis Spectrophotometer Analysis of Coated and Uncoated FTO Surfaces.....	105
6.3.4. Photocurrent density–photo voltage measurements of DSSCs .....	106
6.3.5. Incident Photon to Current Efficiency (IPCE) Measurements of DSSCs .....	108
6.3.6. Electrochemical impedance spectroscopy of the DSSCs.....	110
6.4. Conclusion.....	113
REFERENCES.....	115
7. OPTIMIZING NEW TYPE NANO-COMPOSITE Zr DOPED TiO <sub>2</sub> SCATTERING LAYER FOR EFFICIENT DYE SENSITIZED SOLAR CELLS.	119
7.1. Motivation of Chapter 8 .....	119
7.2. Experimental.....	121
7.2.1. Scattering Particle Preparation.....	121
7.2.2. DSSC Sample Preparation .....	122
7.3. Result and Discussions .....	123
7.4. Conclusion.....	131
REFERENCES.....	133
8. CONCLUSION AND SUGGESTIONS .....	137
CURRICULUM VITAE .....	141

## LIST OF TABLES

### TABLES

<b>Table 3.1.</b> The equivalent circuit elements on EIS have the following meaning.....	57
<b>Table 4.1.</b> Efficiency analysis of DSSCs employing based on 160 nm ITO, 300 nm ITO and 480 nm ITO substrates.....	71
<b>Table 4.2.</b> Kinetic Parameters of the DSSCs with and without blocking layers.....	74
<b>Table 5.1.</b> Efficiency analysis of ITO nanowire and TiO <sub>2</sub> nano powder composite dye sensitized solar cells.....	89
<b>Table 5.2.</b> Kinetic Parameters of ITO nanowire and TiO <sub>2</sub> nano powder composite dye sensitized solar cells.....	92
<b>Table 6.1.</b> Sheet resistance analysis of electrodes produced using bare FTO, ZrO <sub>2</sub> /FTO and TiO <sub>2</sub> /FTO layers before and after heat treatment.....	106
<b>Table 6.2.</b> Efficiency analysis of DSSCs employing bare FTO, ZrO <sub>2</sub> /FTO and TiO <sub>2</sub> /FTO layer electrodes with front and backside illumination.....	108
<b>Table 6.3.</b> Kinetic parameters of the DSSCs with and without blocking layers. ...	112
<b>Table 7.1.</b> Efficiency analysis of devices with T-SL, ZDT-SL and 0-SL electrodes .....	128
<b>Table 7.2.</b> Kinetic Parameters of devices with T-SL, ZDT-SL and 0-SL electrodes .....	131

## LIST OF FIGURES

### FIGURES

<b>Figure 1.1</b> DSSC and its photoanode layers.....	3
<b>Figure 2.1</b> Solar spectrum. ....	12
<b>Figure 2.2</b> Schematic of an ideal solar energy conversion arrangement (a), conversion efficiency of solar radiation to work with that arrangement (b) ....	13
<b>Figure 2.3</b> Top: Schematic of a p-n junction in equilibrium. Energy band diagram of a p-n junction under illumination is shown at the bottom .....	14
<b>Figure 2.4</b> Schematic of the basic structure of a silicon solar cell . ....	16
<b>Figure 2.5</b> III–V multijunction solar cells for concentrating photovoltaics .....	17
<b>Figure 2.6</b> Schematic of the basic structure of a CIGS solar cell .....	18
<b>Figure 2.7</b> Schematic of the basic structures of (a) bilayer and (b) bulk- heterojunction organic solar cells .....	19
<b>Figure 2.8</b> Schematic working principle of a dye sensitized solar cell .....	20
<b>Figure 2.9</b> Charge injection sensitization: a) electron injection b) hole injection ....	21
<b>Figure 2.10</b> Representation of conduction band (CB) and valence band (VB) in terms of band theory for a metal (a), a semiconductor (b), and an insulator (c) 25	25
<b>Figure 2.11</b> Diagram of the energy levels of an n-type semiconductor (a) and of a p- type semiconductor (b).....	26
<b>Figure 2.12</b> Fermi level in an intrinsic semiconductor (a), Fermi level in an n-type semiconductor (b) and in a p-type semiconductor (c).....	28
<b>Figure 2.13</b> Fermi level in an n-type semiconductor (a) and in a p-type semiconductor (b).....	29
<b>Figure 2.15</b> A nanocrystalline TiO <sub>2</sub> layer .....	31
<b>Figure 2.16</b> Structure of N719, N3 and black dye respectively .....	35
<b>Figure 3.1</b> Titanium autoclave used in hydrothermal treatments (AmAr Equipments). .....	45
<b>Figure 3.2</b> Stages of screen printing deposition process .....	48

<b>Figure 3.3</b> Wooden screen used during screen printing deposition .....	49
<b>Figure 3.4</b> A typical dye sensitized solar cell.....	52
<b>Figure 3.5</b> Simple Nyquist plot a) and schematic for an impedance device (b). ....	54
<b>Figure 3.6</b> Impedance spectra of a dye-sensitized solar cell, at different applied potentials. ....	55
<b>Figure 3.7</b> The schematic description of possible electrochemical modeling on DSSC: (a) Equivalent circuit for a complete solar cell. (b) Simplified circuit for insulating TiO <sub>2</sub> (potentials around 0 V) as currents are low, Z <sub>d</sub> may be neglected, (c) Simplified circuit for TiO <sub>2</sub> in the conductive state .....	56
<b>Figure 3.8</b> Schematic description differences from Nyquist and Bode plots.....	58
<b>Figure 4.1</b> Schematic description of chapter 4. ....	62
<b>Figure 4.2</b> The results for the gel formation as a function of H <sub>2</sub> O /PG for two HA/PG weight ratios. ....	63
<b>Figure 4.3</b> Cross-sectional FE-SEM images of 160 nm ITO (a), 300 nm ITO (b), and 480 nm ITO (c), top view of SEM images of 160 nm ITO (d), 300 nm ITO (e), and 480 nm ITO (f). ....	65
<b>Figure 4.4</b> Transmittance spectra for 160 nm ITO, 300 nm ITO, and 480 nm layers in IR - UV visible region from 300 to 2500 nm (a) and linear portion of the (ahv) <sup>2</sup> vs photon energy E(eV) graph of 160 nm ITO, 300 nm ITO, and 480 nm (b) and reflectance spectra for 160 nm ITO, 300 nm ITO, and 480 nm layers in IR - UV visible region from 300 to 2500 nm (c).....	66
<b>Figure 4.5</b> Sheet resistance versus temperature spectra for 300 nm ITO (a), and the variation in sheet resistance, before and after heat treatment, with respect to the ITO film thickness (b). ....	68
<b>Figure 4.6</b> XRD spectra for 160 nm ITO, 300 nm ITO, and 480 nm ITO films.....	69
<b>Figure 4.7</b> J-V curves of DSSCs based on 160 nm ITO, 300 nm ITO and 480 nm ITO substrates under illumination AM 1.5, 100 mW/cm <sup>2</sup> . ....	70
<b>Figure 4.8</b> IPCE spectra for the DSSCs based on 160 nm ITO, 300 nm ITO and 480 nm ITO substrates. ....	72
<b>Figure 4.9</b> Comparison of the resultant Nyquist plots of the symmetrical cells produced using different ITO thicknesses (a) and magnified version of the region between RS and RCT boundary (b). ....	73

<b>Figure 5.1</b> Schematic description of chapter 5 .....	83
<b>Figure 5.2</b> Schematic reaction vessel for the production of ITO nanowires (a). Schematic of nanowire growth steps (b). .....	84
<b>Figure 5.3</b> a) SEM micrograph of ITO nanowires obtained by hydrothermal treatment at 85oC for 24 h. b) a magnified view of same nanowires. ....	86
<b>Figure 5.4</b> XRD spectra for ITO, ITO NW, and TiO <sub>2</sub> particles obtained by sol-gel method. ....	87
<b>Figure 5.5</b> Current density-voltage characteristics of DSSCs based on bare ITO and ITO NW.....	88
<b>Figure. 5.6</b> IPCE spectra of DSSCs based on bare ITO and ITO NW.....	90
<b>Figure 5.7</b> EIS data analysis of ITO NW based DSSC and bare ITO based DSSC. Nyquist plots and EIS fitting system (in the inset) (a) and Bode plots (b). ....	91
<b>Figure 6.1</b> Schematic illustration of blocking layer modified photoanode. ....	100
<b>Figure 6.2</b> Schematic description of chapter 6 .....	101
<b>Figure 6.3</b> Top view FE-SEM images of bare FTO (a), ZrO <sub>2</sub> / FTO (b), and TiO <sub>2</sub> / FTO (c); cross-sectional FE-SEM images of bare FTO (d), ZrO <sub>2</sub> / FTO (e), and TiO <sub>2</sub> / FTO (f). ....	103
<b>Figure 6.4</b> XPS survey spectrum with surface composition of ZrO <sub>2</sub> /FTO sample (a) and Zr 3d XPS spectra of ZrO <sub>2</sub> /FTO sample (b).....	104
<b>Figure 6.5</b> Transmittance spectra for bare FTO, 48 nm ZrO <sub>2</sub> /FTO and 56 nm TiO <sub>2</sub> /FTO layers in visible region from 300 to 800 nm (a) and linear portion of the $(\alpha h\nu)^2$ vs photon energy E (eV) graph of bare FTO, 48 nm ZrO <sub>2</sub> /FTO and 56 nm TiO <sub>2</sub> /FTO layers (b). ....	105
<b>Figure 6.6</b> J-V curves of DSSCs employing bare FTO, ZrO <sub>2</sub> /FTO and TiO <sub>2</sub> /FTO layers electrodes with <b>front</b> (a) and backside (b) illumination (AM 1.5, 100 mW/cm <sup>2</sup> ).....	107
<b>Figure 6.7</b> IPCE spectra for the DSSCs with and without blocking layers. ....	109
<b>Figure 6.8</b> Representative Nyquist plots displaying impedance data taken at open circuit potential (a), equivalent circuit of DSSC used for fitting impedance data (b), and Bode plots displaying impedance data (c) .....	111
<b>Figure 7.1</b> Comparison of DSSC schematics. DSSC with an absorber layer of anatase (a), DSSC with an absorber layer and scattering particles (b).Figure	120

<b>Figure 7.2</b> Schematic description of chapter 7 .....	121
<b>Figure 7.3</b> FE-SEM image of cross sectional view of double-layer film containing P25 TiO <sub>2</sub> particles as the under-layer and ZDT particles as the over-layer (a), and top view of ZDT (b) and T (c) scattering particles.....	123
<b>Figure 7.5</b> XPS survey spectrum of ZDT photo electrode (a) and high-resolution XPS spectrum of O 1s peak (b), Zr 3d peak (c), and comparison of T-SL Ti 2p peak (d) and ZDT-SL Ti 2p peak (e). .....	125
<b>Figure 7.6</b> Diffuse reflectance spectra of the photoanode without dye loading.....	126
<b>Figure 7.7</b> Current density-voltage characteristics of devices with T-SL, ZDT-SL and 0-SL electrodes.....	127
<b>Figure 7.8</b> Incident photon-to-current efficiency measurements of devices with T-SL, ZDT-SL and 0-SL electrodes. ....	129
<b>Figure 7.9</b> EIS spectra of the solar cells fabricated using 0-SL, T-SL and ZDT-SL photoanode: Nyquist (a) and Bode (b) plots. ....	130
<b>Figure 8.1</b> Comparison between modified and classical photoanode PV performance results. ....	139

## ABBREVIATIONS

<b>TCO</b>	: Transparent Conductive Glass
<b>DSSC</b>	: Dye Sensitized Solar Cells
<b>ITO</b>	: Tin-doped Indium Oxide
<b>FTO</b>	: Fluorine-doped Tin Oxide
<b>AZO</b>	: Aluminum-doped Zinc Oxide
<b>BL</b>	: Blocking Layer
<b>EBL</b>	: Electron Blocking Layer
<b>AL</b>	: Absorber Layer
<b>SL</b>	: Scattering Layer
<b>ZDT</b>	: 10% Zr doped TiO <sub>2</sub>
<b>IPCE</b>	: Incident Photon-to-Current Conversion Efficiency
<b>EIS</b>	: Electrochemical Impedance Spectroscopy
<b>SEM</b>	: Scanning Electron Microscope
<b>XPS</b>	: X-ray photoelectron spectroscopy
<b>Jsc</b>	: Short Circuit Current
<b>Voc</b>	: Open Circuit Voltage
<b>FF</b>	: Fill Factor

## CHAPTER 1

### INTRODUCTION

*“If we knew what it was we were doing, it would not be called research, would it?”*

*Albert Einstein*

From the ancient ages, humanity carried out various renewable energy forms like biomass, wind, hydropower, solar energy. The habitat of planet depends on solar radiation that is the most ample or abundant renewable energy source to enough demand of our planet. Solar radiation is a foundation of life. The plants and animals need it to grow and increase the popularity. For many years, humanity strives to survive against nature by using of direct and indirect solar energy renewable forms. However, with the huge explosion of the world population at the beginning of the twenty century, the energy demand has been growth [1]. The humans started to turn towards usage of fossil fuels such as renewable forms of ancient biomass like coal, gas, and oil widely, due to its storage and transportation being easily and having higher energy density than alternative sources. However, the fossil fuels has caused anxiety about environmental damage, geopolitical tensions and tragically puts our climate and our sustenance at stake when it's burned [2]. Therefore, the people canalize toward sustainable energy. In this century, 15 TW energy is consumed a day, while  $174 \times 10^3$  TW energy is received from sun in a day. The solar energy would replace the well-known unrenewable sources if only small fraction of this energy could be harvested [2]. Nearly 13 % of total global energy consumption is provided from renewable sources such as hydropower, biomass, solar, wind, and geothermal currently. The

largest share comes from hydropower energy as 20 % of total renewable sources which has remained constant since 1990 [3]. If the population is constantly growing, hydropower will not be a key for the solution of energy demand from renewable sources. Because the deployment of renewables will be accelerated, therefore progressive green energy policies are implemented in many developed countries. Germany, for example, has declared these policies as green economy, it addresses 51 % of its total energy demand from renewable energy such as photovoltaics and wind power. Wind energy was popular, outperformed photovoltaics in terms of installed capacity, but photovoltaics are now popular, and it has the fastest improvements as power generation technology. In 2030, about 50 % of the total energy will be used from photovoltaic produced electricity if the sector keeps its growth rate annually [4]. The photovoltaic resources try to investigate a decrease in the prices of photovoltaic devices due to economies of large-scale production, and the development of new less expensive thin film technology. Therefore, it is significantly important that the electricity produced by photovoltaics technology has to be harvested by high efficient low-cost solar cells fabricated by abundant non-toxic materials with simple manufacturing processes. Nowadays, silicon based photovoltaic panels recently dominated commercial photovoltaic technology. Their cost of photovoltaic energy production per watt is 4 USD when it was 7.5 USD since 1990 [5]. However, the costs are still away from fossil fuel energy production costs. The dye sensitized solar cell (DSSC) which has been introduced in 1991 by M.Gratzel is an alternative technology for silicon based solar cells due to higher efficiency/cost ratio and shows significant potential for usage as commercial photovoltaic technology portfolio in future [6]. Although, it was popular for not suffering from elevated working temperatures, it is also independent of angle of incidence and intensity of light compared to conventional solar cells, which are silicon based. DSSC has achieved 11 % conversion efficiency after several works [7].

When compared in terms of photon to electron conversion mechanism, conventional p-n junction solar cells can produce electricity in semiconductor matrix where charge separation and conduction occurs in the same material. When DSSC has excitation, charge separation and electronic conduction mechanisms happen to be in different matrices which discussed and given in the chapter of literature survey. The main part

responsible from photo generation is photoanode in DSSCs. Therefore, each part of photoanode of DSSC has to be investigated to achieve high efficiency [7-10]. The highly efficient photoanodes are composed of transparent conductive glass (TCO), blocking layer, absorber layer, and scattering layer which are given in Figure 1.1.

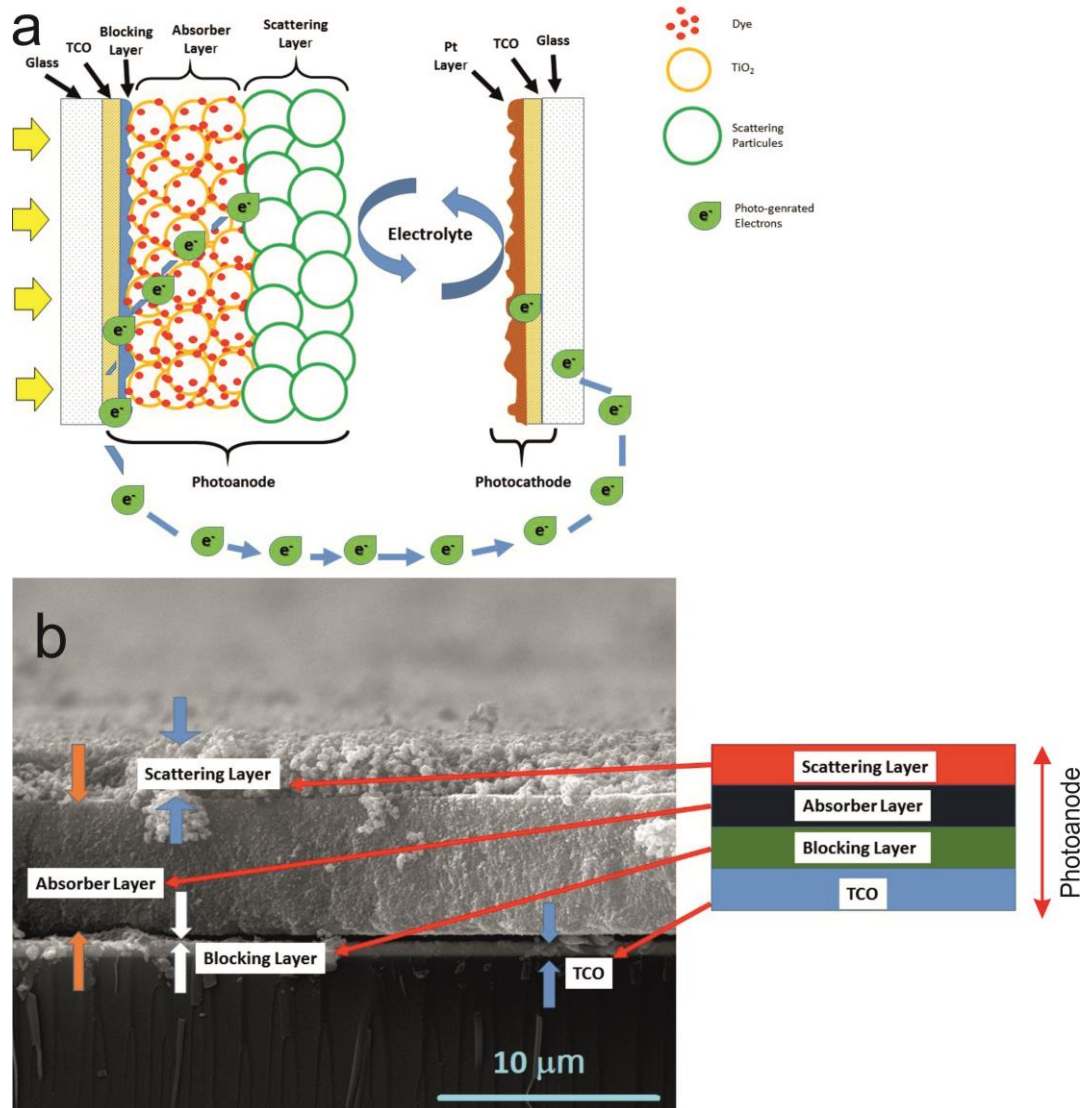


**Figure 1.1** DSSC and its photoanode layers

ITO (tin doped indium oxide) and FTO (fluorine doped-tin oxide) can be potential TCO layers and they are produced by different methods. TCO is responsible for incident light quantity [11]. Nevertheless, there are two problems stemming from TCO

usage on DSSC applications. One of them is the production cost of TCO that could be solved by sol-gel processing method, which is one of the basic techniques that gives the most economical solution. The second one is the maximization of interaction in the interface area between TCO and the photoanodic TiO<sub>2</sub> layer. For this purpose, several studies have been focused on the development of this interface area using 1D nanostructure of ITO nanowires. To produce high efficient interfacial area between ITO-TiO<sub>2</sub>, cross like 1-D nanostructure of ITO is thought to be used. Up till today, there is not any clue about the advantage of using 1D nanostructure of ITO nanowires reported in the literature. In order to reform the conversion efficiency of DSSC, different absorber layer materials can be employed such as SnO<sub>2</sub>, Nb<sub>2</sub>O<sub>5</sub>, ZnO, ZrO<sub>2</sub> rather than P25 (P25 is commercially used photoanode material and produced by Evonik<sup>®</sup> with TiO<sub>2</sub> anatase 95%- rutile 5%) [9, 12-14]. Different metal oxide materials on DSSC have been tried but they did not perform as good as TiO<sub>2</sub>. Because open circuit voltage (V<sub>oc</sub>), which is the difference in the electron energies between the level of  $E_c$  of an electrode and redox potential level, should be higher to reduce the recombination rate of photoinjected electrons. An alternative path to obtain higher V<sub>oc</sub> is to use an absorber layer having more negative conduction band energy ( $E_c$ ) [15-17]. Cation modification that is a type of absorber layer modification resulted in a shift of TiO<sub>2</sub> conduction band in the negative direction. Therefore Zr modified TiO<sub>2</sub> electrodes increase the open circuit photovoltage. In addition, increase in the optical and electrical properties of absorber layer is established by Zr doping on TiO<sub>2</sub> matrix which caused inhibition of rutile. Rutile is an unwanted phase for photovoltaic applications. Therefore, Zr modification decreases recombination rates and increases photon to current efficiency value compared to bare TiO<sub>2</sub> due to high electron mobilities. For these reasons, Zr<sup>+4</sup> cation modification was applied on absorber layer to enhance better photovoltaic performance. Electron Blocking Layer (EBL), which is typically composed of a thin film coating on TCO is significant for reducing of undesired recombinations [18]. Optimizing the thickness and quality of EBL is significant for photovoltaic performance. Generally, to prevent the backward recombination reaction, a TiO<sub>2</sub> thin layer as EBL is coated using TiCl<sub>4</sub> hydrothermal treatment or by spray pyrolysis of TiO<sub>2</sub> alcoholic solvents on TCO. However, TiO<sub>2</sub> layer deposited on TCO causes a decrease in the transparency values resulting in reduced interior light inside the cell. In order to obtain highly efficient cell, EBL performance of ZrO<sub>2</sub> has been realized in this thesis for the first time in the literature. The work also highlighted the

experimental conditions for the production of highly transparent  $\text{ZrO}_2$  EBL that has low charge carrier resistance for the minimization of DSSC efficiency loss. The scattering layers enable to increase the light absorption ability of DSSC via unused photons scattering back to metal oxide sensitized interface. A suitable scattering layer (SL) has different characteristics like higher particle size ( $>100$  nm) than absorber layer and it should not have any reducing effect on dye loading characteristics of absorber layer [19-21]. Nevertheless, traditional scattering layers reduce the dye loading capacity of the absorber layer, which is a challenge to achieve highly efficient cells [22]. In working out this problem, production of scattering layer that has positive effect on dye loading capacity of DSSC is important [15, 23-25]. To produce a suitable effective Scattering Layer, it can be modified by Zr doping of  $\text{TiO}_2$ . In the chapter 9 of this thesis, 10% Zr doped  $\text{TiO}_2$  (ZTO) has been synthesized by hydrothermal method and used as a SL to improve photo conversion efficiency of DSSC. The aim of this work is to enhance low cost - efficiency ratio by modification of each part of dye-sensitized solar cell. Each of modifications is given in results and discussion chapters.

“I gain inspiration from Thomas Edison who is a genius inventor of many electric and electronic devices. In 1931, not long before he died, he said his friends Harvey Firestone and Henry Ford: *“I’d put my money on the sun and solar energy. What a source of power! I hope we don’t have to wait until oil and coal run out before we tackle that.”* The thesis intends to support the design and development of the nanocrystalline dye sensitized solar cell by academic optimization process on photoanode materials and device architecture. Our world is still under the sunshine and we can harvest and profit from it easily”.



## REFERENCES

1. Century, R.E.P.N.f.t.s., *Renewable's Global Status Report: Update 2009*. 2009.
2. BP, *BP Statistical Review of World Energy*. 2010.
3. Agency, I.E., *Trends in Photovoltaic Applications: Survey report of selected IEA countries between 1992 and 2008*. Photovoltaic Power Systems Programme, 2009.
4. Solomon, S., *Climate change 2007-the physical science basis: Working group I contribution to the fourth assessment report of the IPCC*. Cambridge University Press, **4**. 2007
5. Umwelt, B.f., *Erneuerbare Energie in Zahlen: Nationale und internationale Entwicklung Berlin*. Naturschutz und Reaktorsicherheit, 2009.
6. Oregan, B. and M. Gratzel, *A Low-Cost, High-Efficiency Solar-Cell Based on Dye-Sensitized Colloidal TiO<sub>2</sub> Films*. *Nature*, **353**(6346): p. 737-740. 1991.
7. Ito, S., et al., *Fabrication of thin film dye sensitized solar cells with solar to electric power conversion efficiency over 10%*. *Thin Solid Films*, **516**(14): p. 4613-4619. 2008
8. Bisquert, J., et al., *Physical chemical principles of photovoltaic conversion with nanoparticulate, mesoporous dye-sensitized solar cells*. *Journal of Physical Chemistry B*, **108**(24): p. 8106-8118. 2004.
9. Wang, P., et al., *High efficiency dye-sensitized nanocrystalline solar cells based on ionic liquid polymer gel electrolyte*. *Chemical Communications*, (24): p. 2972-2973. 2002.
10. Snaith, H.J., et al., *Efficiency enhancements in solid-state hybrid solar cells via reduced charge recombination and increased light capture*. *Nano Letters*, **7**(11): p. 3372-3376. 2007.
11. Gao, F., et al., *Enhance the optical absorptivity of nanocrystalline TiO<sub>2</sub> film with high molar extinction coefficient ruthenium sensitizers for high performance dye-sensitized solar cells*. *Journal of the American Chemical Society*, **130**(32): p. 10720-10728. 2008.

12. Zakeeruddin, S.M., et al., *Design, synthesis, and application of amphiphilic ruthenium polypyridyl photosensitizers in solar cells based on nanocrystalline TiO<sub>2</sub> films*. Langmuir, **18**(3): p. 952-954. 2002.
13. Snaith, H.J. and M. Gratzel, *Electron and hole transport through mesoporous TiO<sub>2</sub> infiltrated with spiro-MeOTAD*. Advanced Materials, **19**(21): p. 3643-3653. 2007.
14. Barbe, C.J., et al., *Nanocrystalline titanium oxide electrodes for photovoltaic applications*. Journal of the American Ceramic Society, **80**(12): p. 3157-3171. 1997.
15. Cherepy, N.J., et al., *Ultrafast electron injection: Implications for a photoelectrochemical cell utilizing an anthocyanin dye-sensitized TiO<sub>2</sub> nanocrystalline electrode*. Journal of Physical Chemistry B, **101**(45): p. 9342-9351. 1997.
16. Kitiyanan, A., et al., *The preparation and characterization of nanostructured TiO<sub>2</sub>-ZrO<sub>2</sub> mixed oxide electrode for efficient dye-sensitized solar cells*. Journal of Solid State Chemistry, **178**(4): p. 1044-1048. 2005.
17. Kitiyanan, A. and S. Yoshikawa, *The use of ZrO<sub>2</sub> mixed TiO<sub>2</sub> nanostructures as efficient dye-sensitized solar cells' electrodes*. Materials Letters, **59**(29-30): p. 4038-4040. 2005.
18. Cameron, P.J., L.M. Peter, and S. Hore, *How important is the back reaction of electrons via the substrate in dye-sensitized nanocrystalline solar cells?* Journal of Physical Chemistry B, **109**(2): p. 930-936. 2005.
19. Ferber, J. and J. Luther, *Computer simulations of light scattering and absorption in dye-sensitized solar cells*. Solar Energy Materials and Solar Cells, **54**(1-4): p. 265-275. 1998.
20. Nitz, P., et al., *Simulation of multiply scattering media*. Solar Energy Materials and Solar Cells, **54**(1-4): p. 297-307. 1998.
21. Usami, A., *A theoretical simulation of light scattering of nanocrystalline films in photoelectrochemical solar cells*. Solar Energy Materials and Solar Cells, **62**(3): p. 239-246. 2000.
22. Toyoda, T., et al., *Outdoor performance of large scale DSC modules*. Journal of Photochemistry and Photobiology a-Chemistry, **164**(1-3): p. 203-207. 2004.

23. Dai, S., et al., *Dye-sensitized solar cells, from cell to module*. Solar Energy Materials and Solar Cells, **84**(1-4): p. 125-133. 2004.
24. Eppler, A.A., I.N. Ballard, and J. Nelson, *Charge transport in porous nanocrystalline titanium dioxide*. Physica E-Low-Dimensional Systems & Nanostructures, **14**(1-2): p. 197-202. 2002.
25. Gratzel, M., *Conversion of sunlight to electric power by nanocrystalline dye-sensitized solar cells*. Journal of Photochemistry and Photobiology a-Chemistry, **168**(3): p. 235-235. 2004.



## CHAPTER 2

### LITERATURE SURVEY

Solar energy can be transformed into various energy forms such as chemical energy, bioenergy, electricity, or heat. We are focusing on photovoltaic (PV) conversion. Solar cell or photovoltaic device is composed of two parts including cathode and anode. Edmon Bequerel discovered the photovoltaic effect in 1839 [1]. After almost half a century, Charles notified a first solar cell made from selenium and gold, which had nearly 1% photon to electricity conversion efficiency. However, Albert Einstein is a pioneer theoretical worker about photovoltaic effect [2]. He insists that electrons were emitted from materials due to absorption of photons (light quanta). Nowadays, physics of photovoltaic conversion by the solar cell devices is barely well explained. Although, silicon solar cells are commercial products in the photovoltaic market, the less expensive semiconductor solar cells, which are CdTe and Cu(In,Ga)Se and amorphous or crystalline thin silicon solar cells are growing in the market shares. Organic and inorganic solar cells such as dye-sensitized solar cells and organic solar cells, which are new type PV devices, are potential solar cells for the PV market.

#### 2.1. Solar Irradiance and Spectrum

According to Planck's distribution, electromagnetic radiation coming from sun or any light source can be well approximated by a black body at a temperature of 5800 K [3]. Photons show wave-like behavior and characterized by formula where  $c$  and  $h$  are the speed of light including wavelength  $\lambda$ , and the Planck constant carrying an energy  $E$  associated to its wavelength is given by:

$$E = \frac{h\nu}{\lambda} \dots\dots\dots(2.1)$$

The solar energy is homogeneous on the surface of sun. Its total spectrum is decomposed by atmospheric effects such as light absorption of oxygen (O<sub>2</sub>), ozone (O<sub>3</sub>), nitrous oxide (N<sub>2</sub>O), methane (CH<sub>4</sub>), water vapor (H<sub>2</sub>O), and carbon dioxide (CO<sub>2</sub>) because of the mileage between sun and the earth, and tailor available solar energy on earth. The effect of atmosphere on solar spectrum distribution can be given by

$$Air\ Mass = \frac{1}{\cos\theta} \dots\dots\dots(2.2)$$

where  $\theta$  is the angle of incidence.

Solar radiation on top of the atmosphere (AM0 1.37 kW/m<sup>2</sup>) and solar radiation on sea level (AM 1.5G 1.0 kW/m<sup>2</sup>) are compared in Figure 2.1 which demonstrates solar energy with different wavelengths versus intensities of solar irradiances [4].

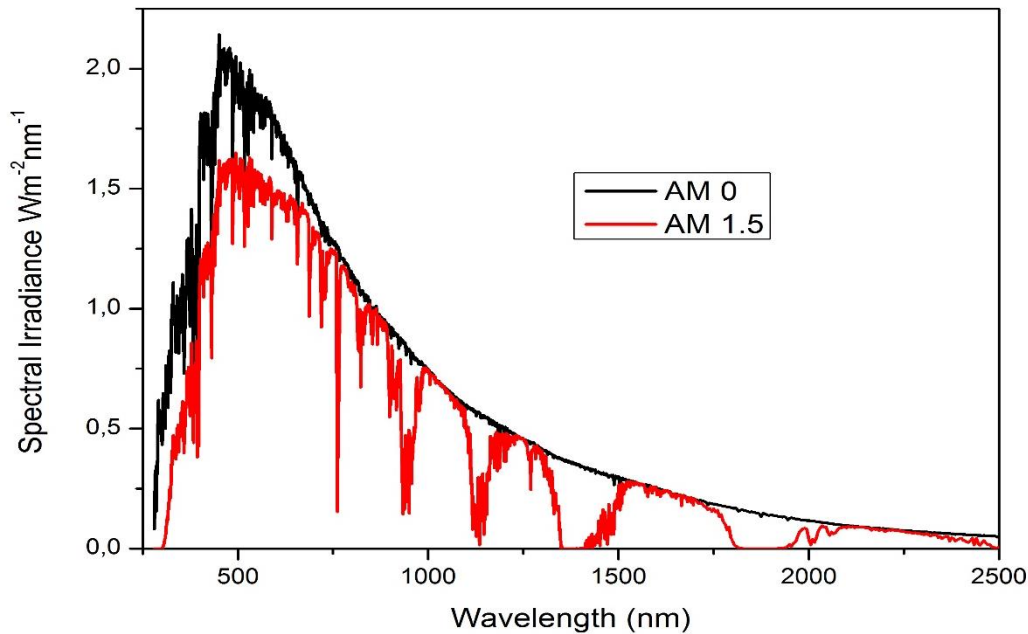


**Figure 2.1** Sun solar spectrum.

Due to solar energy conversion depending on the nature and working mechanisms of semiconductor, available sun energy which is incident on earth cannot be completely converted to electricity. It can be described according to Würfel's works on photovoltaic thermodynamic properties. Maximum solar energy conversion efficiency is an ideal thermodynamic converter machine, which is an ideal heat engine (Carnot), given in Figure 2.2 [5].

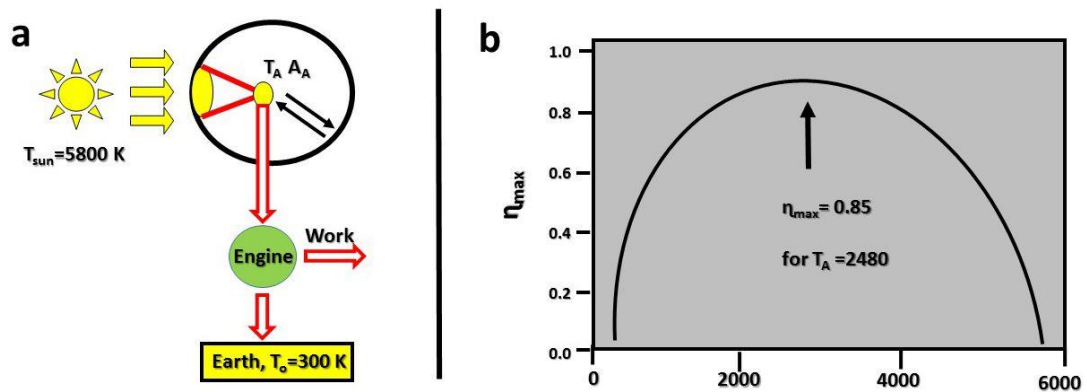


**Figure 2.2** Schematic of an ideal solar energy conversion arrangement (a), conversion efficiency of solar radiation to work with that arrangement (b) [6].

According to the Stefan-Boltzmann law, the Carnot engine is in contingency with at temperature of earth ( $T_0$ ). Other parameters are received energy current on absorber ( $I_{\text{abs}}$ ) from the sun and emitted current of energy ( $I_{\text{em}}$ ). The theoretical overall efficiency for photovoltaic conversion to work by an absorber of black-body included with a Carnot engine after it is 85 % procured with a temperature of absorber ( $T_A$ ) is nearly 2500 °K.

## 2.2. Structure of Basic Solar Cell

A basic solar cell is composed of an intrinsic electronic band gap that absorbs photon energy equal or higher than this gap to produce extinction where electron and hole pair occurs. Excitation is described as separated electron–hole pair. The extinction is produced with a favorable energetic alignment of materials where holes move to cathode and electrons to anode. a photovoltage builds up when the accumulation of

charges at the contacts,. If external circuit is connected to the contacts of electrode, the cell is able to produce electrical energy at an external load. Commercial solar cells are mostly composed of p-n semiconductor junctions to achieve maximum conversion efficiency. An n-doped and a p-doped close contacted semiconductor material create p-n junction where donor and acceptor ions create an electric field. The depletion layer that is a space charge region forms, due to inter diffusion and recombination of free holes and electrons at the contact (Figure 2.3). In this region, the electric field counterattack causes the drift force that at equilibrium conditions, no net current flows [5].

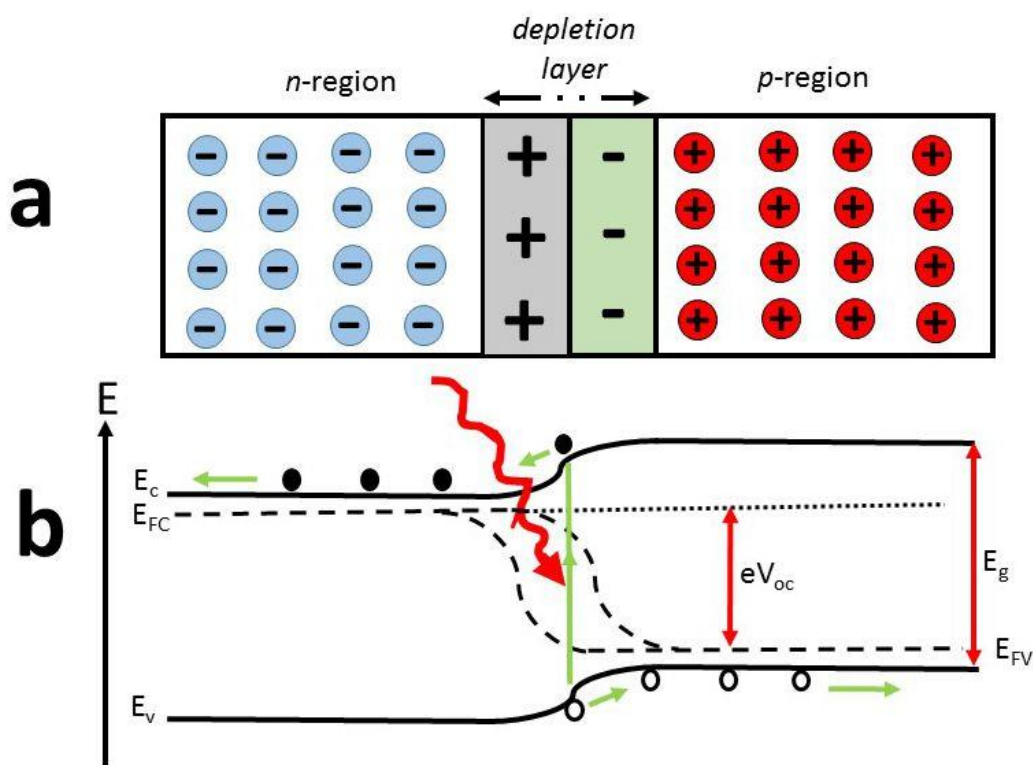


**Figure 2.3** Top: Schematic of a p-n semiconductor junction in equilibrium (a), diagram of energy band of a p-n junction under illumination (b) [6].

An electron – hole pair can be formed under illumination that has enough or higher energy to exceed the semiconductor band gap. The electron and holes have differences in electrochemical potential in p and n semiconductor regions, which result different conductivities and carrier concentrations [7].

## 2.3. Brief Overview on Photovoltaic Technologies and Market

The photovoltaic technology can be divided into four classes [8].

- Wafer-based silicon : classical Si based systems as amorphous, poly or single crystalline silicon cells
- Concentrator systems : multi junction technology such as GaInP/GaInAs/Ge
- Thin film technologies : (CIGS), CdTe, and lately  $\text{Cu}_2\text{ZnSn}(\text{S},\text{Se})_4$  (CZTS), a-Si
- Emerging technologies : organic and dye sensitized solar cells

### 2.3.1. Wafer Based Solar Cells

Commercial silicon cells are known as wafer-based solar cells (Figure 2.4). They can be produced from crystalline and multi-crystalline-silicon substates. Maximum photon to electricity conversion efficiency is about 25% for c-Si and 20.4 % for mc-Si. The sc-Si has indirect band gap, therefore it has low absorption coefficient. For this purpose, the p-n junction is composed of 300  $\mu\text{m}$  p-type silicon and 1  $\mu\text{m}$  n-type silicon. The single crystalline silicon wafers are produced by Czochralski method. It is a highly expensive and energy consuming semiconductor production technique. Multi crystalline silicon wafers are less expensive than c-Si. The production procedure includes that large pots of molted silicon carefully cooled and solidified. However, both techniques have disadvantages such as large material losses during sawing process [9].

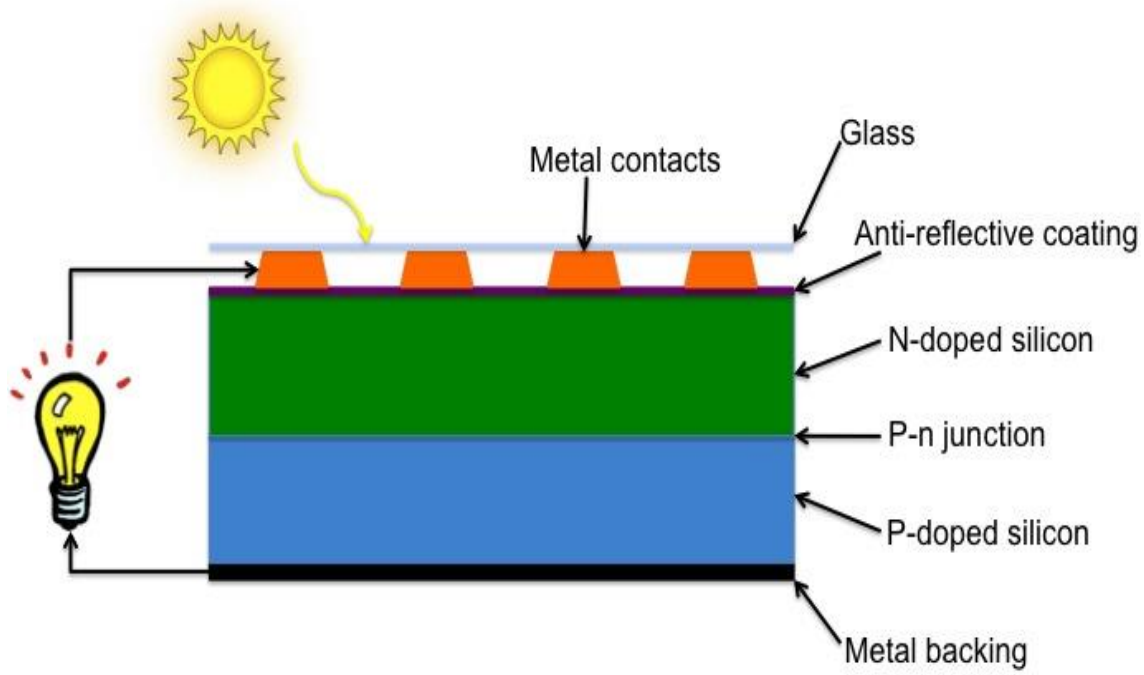


**Figure 2.4** The basic structure of a wafer silicon-based solar cell [10].

### 2.3.2. Concentrator Systems

The concentrator systems (Figure 2.5) are composed of different thin film junctions that are grown on top of each other (multi junction) in order to absorb large fraction of the solar irradiation than a single-layered solar cell [11, 12]. III-IV semiconductors epitaxially grown are used as solar cell absorber layer. Nowadays, it has been reached a record efficiency of 41.6% [13].

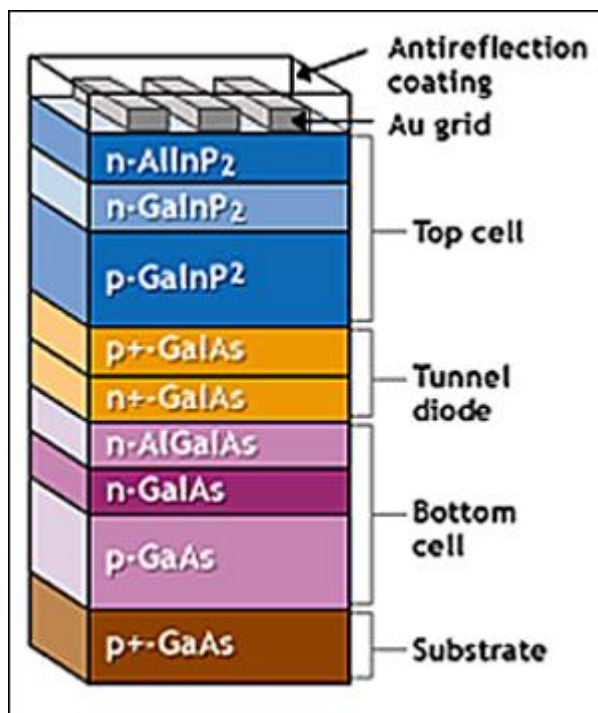


**Figure 2.5** III–V multijunction solar cells for concentrating photovoltaics [14].

### 2.3.3. Thin Film Technologies

The solar cells based on polycrystalline compounds like CdTe,  $\text{Cu}_2\text{ZnSn}(\text{S},\text{Se})_4$  (CZTS),  $\text{Cu}(\text{In},\text{Ga})\text{Se}_2$  (CIGS), or amorphous silicon and short range order silicon can be given as different types of thin film solar cells. The polycrystalline absorber materials have direct band gap transitions which allow for thinner absorber layers. The best suitable material is CIGS (Figure 2.6) having 20 % photon to electricity conversion efficiency [15]. CIGSs are produced under high vacuum evaporation conditions. In addition, it has toxic material such as Se, Te, Cd. Therefore, they have a true concern for large-scale production. The thin film amorphous silicon cells are produced by chemical vapor deposition with decomposition of  $\text{SiH}_4$  gases on the substrate surface. However it is produced easily than c-Si, it has structural defects, which are illustrated with dangling-bonds that must be hydrogenated to decrease recombination rates at dangling-bonds and its absorption coefficient is higher than c-Si because of structural disorder. It has reached 10.1 % efficiency in lab scale [16, 17].

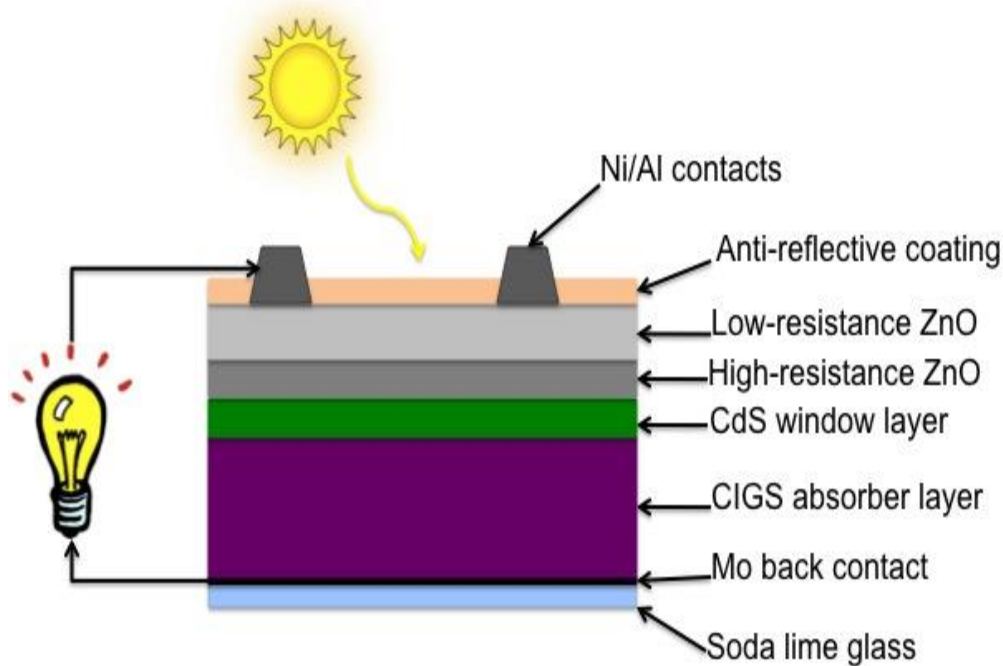


**Figure 2.6** the basic description of a CIGS based solar cell [10].

#### 2.3.4. Emerging Technologies

Emerging technologies as organic (Figure 2.7) and dye sensitized solar cells might be expected as a potential leader of photovoltaic technology in 20 years. Although modules of them have less efficiency than commercial solar cells, their cost or per watt production is trice or fourth times lower than the silicon wafer based solar cells. However, some of companies such as Sharp and Sony start to invest on these technologies and develop industrially pilot plants. The other small companies such as Dyesol, Konarka, Solaronix, G24i and Heliatek are close to the commercialization of small consumer and end user applications. In addition, new excitonic concepts that include multiple excitonic, multibanding and quantum structured cells having higher efficiencies are growing in scientific resources and are produced in lab scale. These type solar cells can be alternatives to commercial wafer based solar cells (silicon) due to their high efficiency cost ratio.

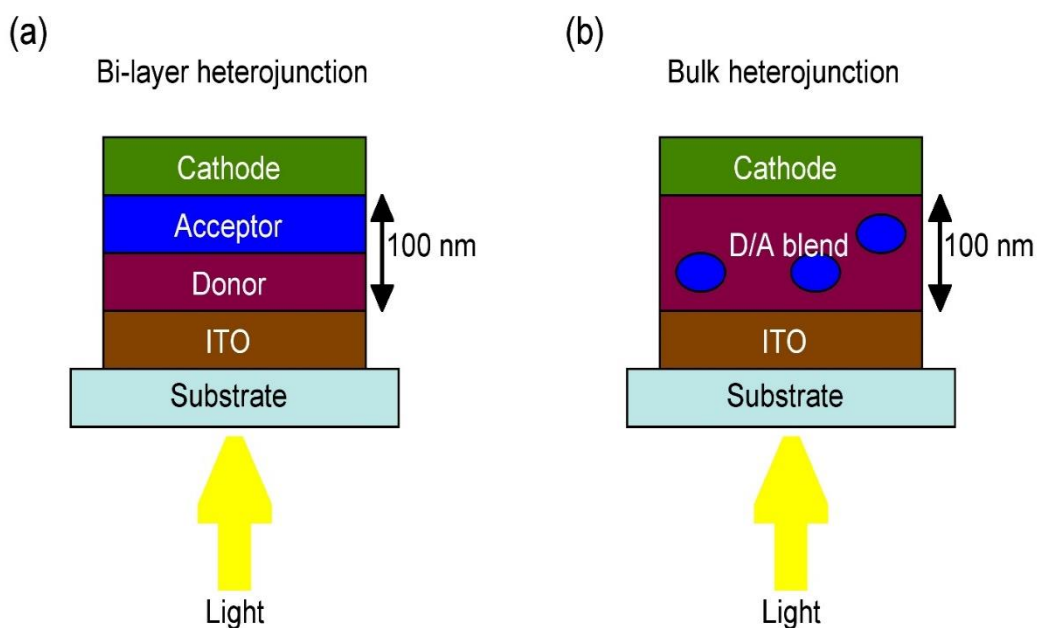


**Figure 2.7** The basic structures of organic cells, bilayered (a) and heterojunction (b) [18].

#### 2.4. Dye Sensitized Solar Cells

Dye sensitized solar cells (DSSCs) can be defined as photo-electrochemical solar cells; it is highly popular subject in research in renewable energies due to its economic photovoltaic cells. DSSCs are composed of the visible light of molecular dyes sensitization. Simple working principles of DSSCs are showed in Figure 2.8. The cell is composed of sandwich electrodes, which are photoanode, photocathode, and a redox electrolyte system. Both electrodes are mainly made from a transparent conductive glass (TCO). Fluorine-doped tin oxide (FTO) or tin-doped indium oxide (ITO) on glass substrate are well known materials as TCO applications due to having few  $\Omega$ /square surface electrical resistivity and well optical transmission on the whole solar spectrum.

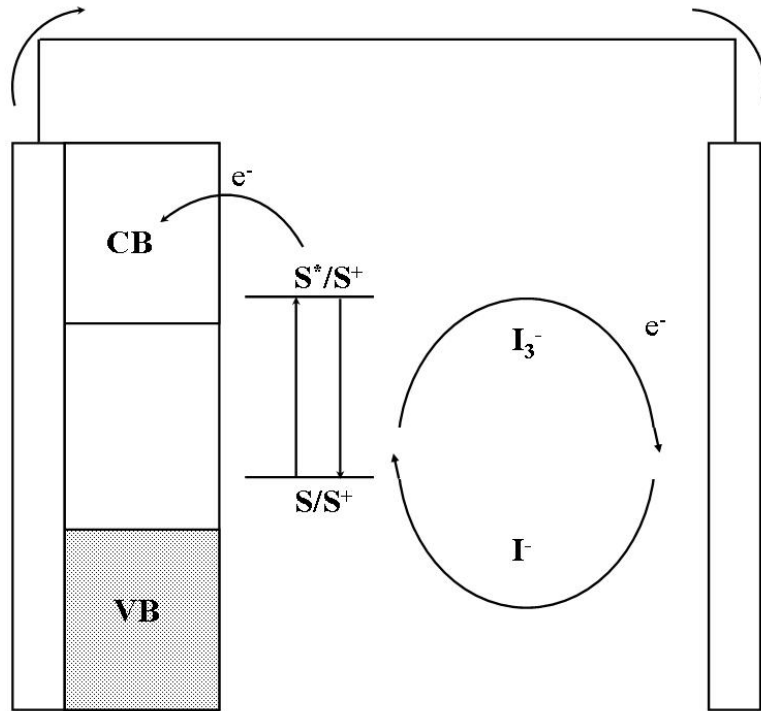


**Figure 2.8** Schematic working principle of a dye sensitized solar cell [19].

The photoanode can be described simply as follows; the TCO is coated with a 7-15  $\mu\text{m}$  thick film of a mesoporous semiconductor oxide, which is generally  $\text{TiO}_2$ , obtained via a sol-gel or hydrothermal technique. This mesoporous semiconductor oxide, which is known as absorber layer (AL), can be deposited by several methods on TCO substrate such as spraying, screen printing, doctor blade technique, dip coating, and spin coating. The coated layer is sintered in open atmosphere oven since an interconnected network should be created for percolation of photo-generated electrons through the TCO [20].

“Sensitization mechanism is obtained by photo-excited sensitizer. Its electronically excited state can promote a heterogeneous charge transfer reactions with the semiconductor metal oxide. If the sensitizer’s the excited state energy level is higher than the bottom of the conduction band, an electron will be injected with no thermal activation barrier in the semiconductor, leaving the sensitizer in its one electron oxidized form (Figure 2.9.a). if the excited state has lower energy than the top of the

valence band, an electron transfer (formally a hole transfer) between the semiconductor and the sensitizer will occur leaving the molecule in its one electron reduced form (Figure 2.9.b) [21]’.

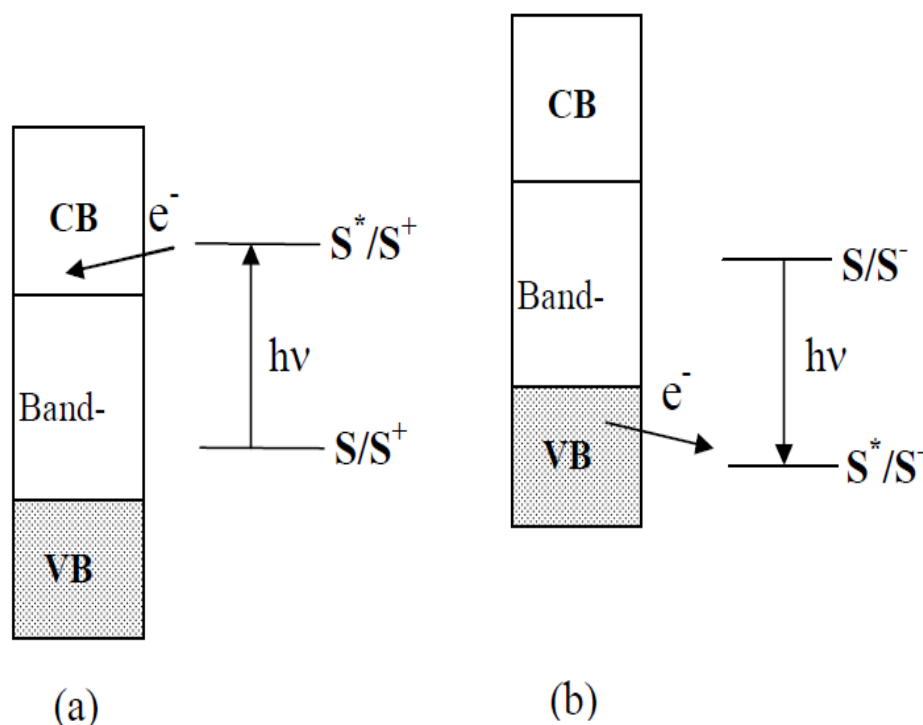


**Figure 2.9** injection of charge mechanism in sensitization process electron (a), hole injection (b) [21].

Suitable anchoring groups on dye molecules bond the sensitizer to semiconductor surface for better electron accumulating efficiency. Generally, dye loading of semiconductor is obtained from semiconductor film left immersed in dye solution. A good sensitizer should have functional groups such as  $-\text{COOH}$ , in order to adsorb better onto the semiconductor substrate [22, 23]. The electrolyte solution, which is defined as a redox couple in a suitable solvent, penetrates semiconductor film to reduce quickly the oxidized sensitizer. The counter electrode which has a role on the catalytic effect in the reduction process of redox couple is placed across the photoanode. It is generally composed of a metallic platinum film coated on TCO glass or metal substrates.

The photo electrochemical cycle of dye sensitized solar cells can be described as follows;

The sensitizer molecules absorb the incident light photons. The photon absorption moves the dye molecules into their excited state.



The excited dyes inject the photo-generated electrons to the empty conduction band of semiconductors (TiO<sub>2</sub>).



The injected photo-generated electrons percolate through the network of nanoparticles. The conductive transparent oxide layer of photoanode collects the photo-generated electrons.

Oxidized sensitizer (Dye<sup>+</sup>) can be reduced to its ground state rapidly by I<sup>-</sup> ions in the electrolyte solution.



Photo-generated electrons used on an electrical circuit produce the electric work, they reach the counter electrode and reduce I<sub>3</sub><sup>-</sup> to I<sup>-</sup>. The entire cycle is used as the quantum conversion of photons to electrons.



Photo-generated electrons should be prevented from any recombination process to harvest a higher solar cell efficiency. The three major recombination processes in a DSC are due to

**i)** Electron recombination transfer occurring at the electrolyte- metal oxide semiconductor interface between excited dye molecules and electrons in the conduction band of the semiconductors.



**ii)** Electron capture from mediator; semiconductor nanoparticles reduce  $\text{I}_3^-$  to  $\text{I}^-$ .



**iii)** Electron recombination on TCO substrate, the photo-generated electrons reduce  $\text{I}_3^-$  to  $\text{I}^-$  on TCO surface.



According to kinetic parameters, the performance of dye-sensitized solar cell depends on kinetic competition between various redox couples processes during photon to electricity conversion [24, 25]. The regeneration of excited sensitizer is nearly  $10^7$ - $10^9$   $\text{s}^{-1}$ , while electron injection to semiconductor is nearly seen in femto second or pico second range ( $10^{-15}$ - $10^{-12}$  s) [25]. This means that; electron injection is more than 1000 times faster than recombination of excited dye semiconductor - redox couple boundary region interaction. According to literature, electron transport in nanoparticles network to TCO is nearly one order of magnitude rapid than recombination. The electron transfer dynamics in DSSC has important role on optimized cells in terms of charge collection efficiency [26].

The several photo-electron generation and electron injection processes have been widely studied since 1991. After the discovery of photo-electrochemical techniques, the effect of dye regeneration and back transfer reactions on electron transfer boundaries (resistance of cell parts) could be understood better. Principles of main components of dye-sensitized solar cells are the electron transfer processes, the

properties of the semiconductor materials, and the sensitization of the semiconductor and the kinetic requirements of the electron transfer mediators.

### **2.4.1. Semiconductor Materials and Properties**

A semiconductor is a material that has conductivity between metal and insulator (Figure 2.10). In general terms, solids are grouped as semiconductors if they have conductivities in the range of  $10^{-9}$  to  $10^3 \text{ ohm}^{-1} \text{ cm}^{-1}$ . The differences between semiconductor electrodes and metallic electrodes lie on electronic structure of these materials [27]. “The solid is regarded as a big molecule that has valence electrons ranging over the whole solid. One approach to the electronic levels in solids is to consider assembly of isolated atoms to bring together to form a crystal. Because of infinite number of atoms, the electronic structure of solids is discussed as energy bands, which are made up of atomic orbitals of the individual atoms. Moreover, because of the large numbers of interacting orbitals the spacing of electronic energies within a band, arising from a given quantum state, becomes so small that the band can be effectively considered as a continuum of energy levels; however, the energy gap between the groups of levels corresponding to different atomic quantum states is preserved. Thus, we see that the allowed electronic energies fall into energy bands of closely spaced levels, with forbidden gaps between these bands. The molecular orbitals, often the energy levels that are the highest occupied called the valence band (VB) and the highest unoccupied called the conduction band (CB). The energy difference between the upper edge of the valence band and the lower edge of the conduction band called as energy gap and it determines the properties of the material [27]”.

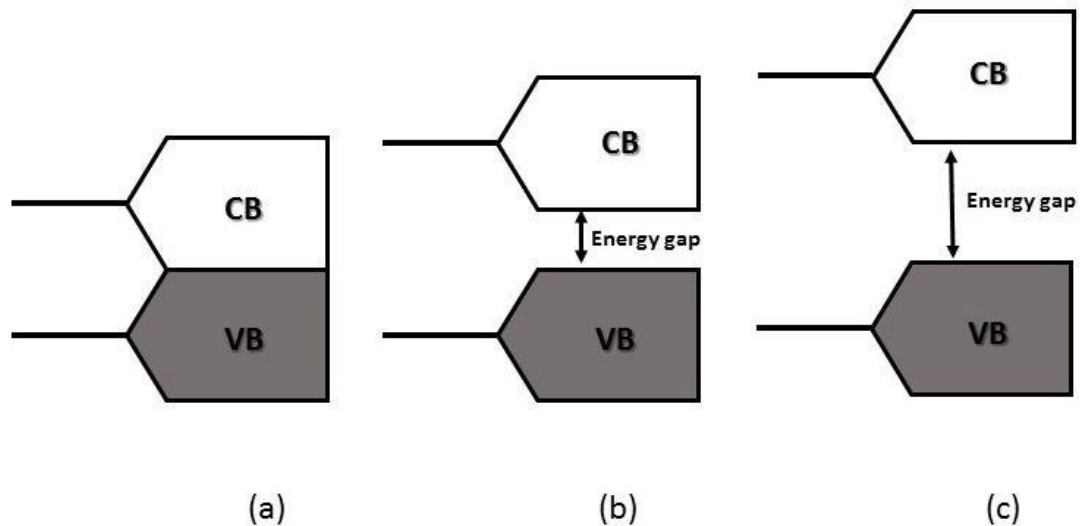


**Figure 2.10** Representation of conduction band (CB) and valence band (VB) in terms of band theory for a metal (a), a semiconductor (b), and an insulator (c) [28].

In an insulator, the valence band is full of electrons, the conduction band is empty, and no motion of charge results from the application of an electric field. In a metal, the valence band electrons can only partially fill the band, or a filled valence band overlaps an empty conduction band. An electric field can move these electrons, because of their large numbers, high conductivities can be achieved. In semiconductors the band gap is smaller and electrons in valence band can be promoted to the upper band thermally or optically that results in an electrical conductivity which is smaller compared to metals because of the fewer number of charge carriers. A positively charged vacancy that is named as a hole is formed by exciting of an electron from the VB to the CB. Holes are considered as mobile and they can be moved by the transfer of one electron to the vacancy. On the other hand, there is doping method for generating charge carriers within a semiconductor material. Doping is the method of adding a different elements to the semiconductor. Most common applications of doping involve the introduction of a 5A element or of a 3A element to a 4A element. For example, doping Si with P introduces new energy levels in the band gap which are occupied and they are close in terms of energy to the CB allowing easy excitement of electrons into the CB (Figure 2.11.a). The addition of an electron deficiency to the lattice results in the formation of vacant energy levels close to the upper edge of the valence band. That makes easy excitement of electrons from the VB (Figure 2.11.b). Doped

semiconductors are named as extrinsic semiconductors. If the electrons are majority charge carriers, semiconductor is indicated as *n-type*, and if the dominant charge carriers are holes, SC is referred as *p-type*.

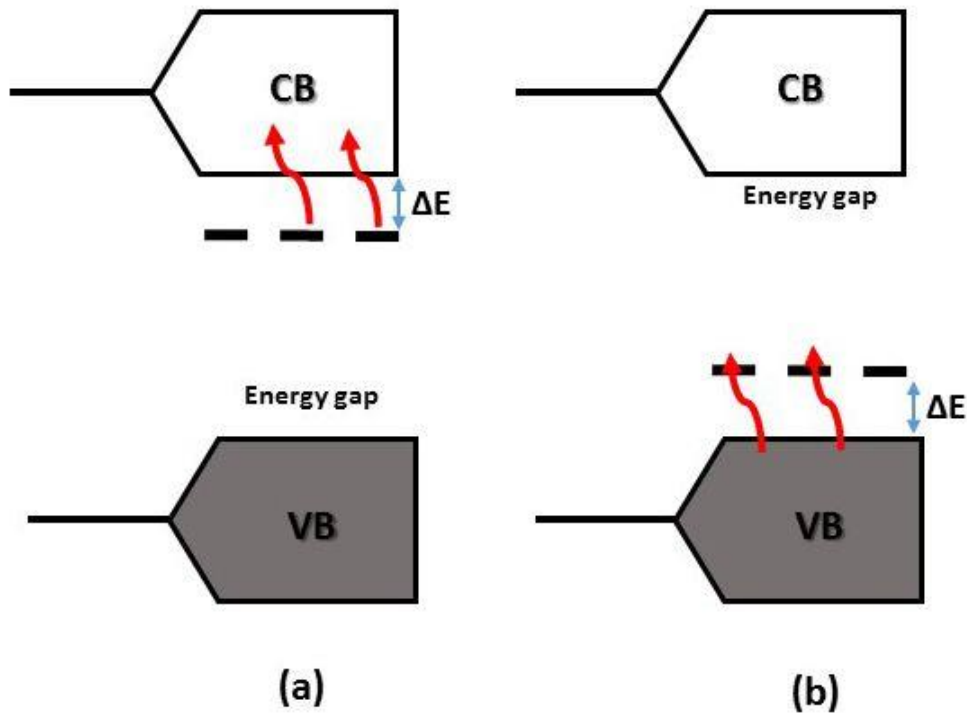


**Figure 2.11** Schematic description of the energy levels of an n-type semiconductor (a) and of a p-type semiconductor (b) [28].

Fermi Level is another important concept of the solid-state materials. The Fermi – Dirac distribution can be given as,

$$f(E) = \frac{1}{1 + e^{\frac{E-E_f}{kt}}} \dots \dots \dots (2.3)$$

Here  $f(E)$  is the probability that a state of energy  $E$  is occupied,  $k$  is the Boltzmann’s constant,  $E_F$  is a parameter called the Fermi energy and  $T$  is the absolute temperature.

As it is seen in Equation (2.3),  $E_F$  is the energy for which  $f(E) = 1/2$ . It is a virtual energy level which has 50% of probability to be occupied by the electrons.

The entropy of the system  $S$  statistically is given by:

$$S = k \ln W \dots\dots\dots(2.4)$$

$W$  is the thermodynamic probability of the state of the system that is defined by the number of ways of distributing the particles in the available states. For a Fermi-Dirac system, entropy change resulting from the addition of one particle to a state of energy  $E$  is:

$$dS = k \ln\left(\frac{f-1}{f}\right) \dots\dots\dots(2.5)$$

$$dS = k \frac{Ef-E}{T} \dots\dots\dots(2.6)$$

Moreover, the total differential for the entropy change for the addition of  $dN$  particles at energy  $E$  is written as:

$$dS = \left(\frac{\partial S}{\partial N}\right)_{E,\nu} dN + \left(\frac{\partial S}{\partial E}\right)_{N,\nu} dE \dots\dots\dots(2.7)$$

$N$  is the total number of particles. If energy resulting from the addition of one electron to the system is calculated, we see that:

$$\left(\frac{\partial S}{\partial N}\right)_{E,\nu} = \frac{Ef}{T} \dots\dots\dots(2.8)$$

By definition the electrochemical potential  $\mu$  is

$$\mu = \left(\frac{\partial G}{\partial N}\right)_{p,T} = -T \left(\frac{\partial S}{\partial N}\right)_{E,\nu} \dots\dots\dots(2.9)$$

Thus comparing (2.8) and (2.9) shows that the Fermi energy is the electrochemical potential, or partial molar free energy per electron. If two systems are in equilibrium the result is physically understandable. Thermodynamically it is expected that they exchange electrons until their electrochemical potentials become equal. In case of Fermi statistics, particle transfer from one system to another that fills lower energy states in one system emptying the higher filled states in the other system will continue

until the distributions over energy in the two systems get equal or until the Fermi levels are equal.

For intrinsic semiconductors the place of Fermi level is at the midpoint of energy band gap (Figure 2.12.a). Fermi energy and the distributions of electrons within the solid are changed by doping. In an n-type semiconductor the Fermi level (Figure 2.12.b) lies just below the conduction band, on the other hand for a p-type semiconductor it is just above the valence band (Figure 2.12.c). Furthermore, as can be seen with metal electrodes, the Fermi energy of semiconductor electrodes varies with the applied potential. As an instance applied positive potential lowers the Fermi level.

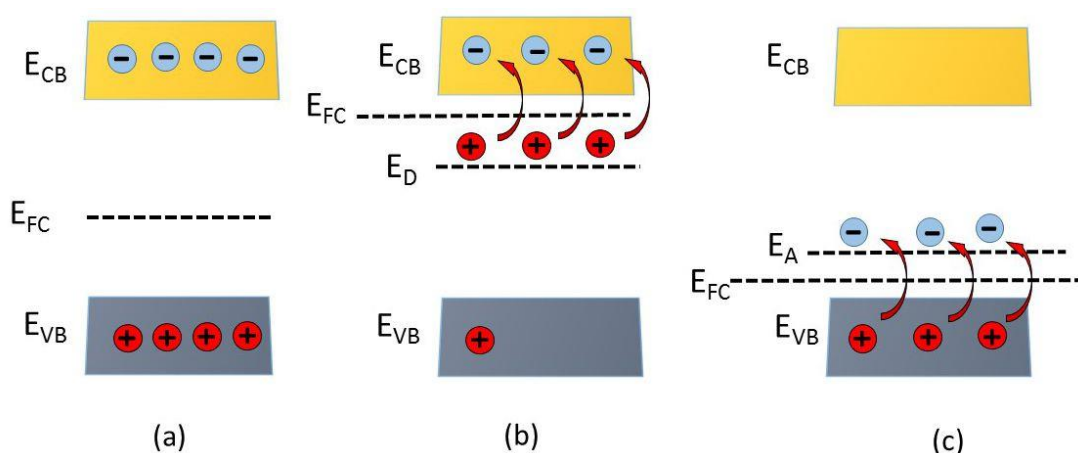


**Figure 2.12** Fermi level in an semiconductor (a), Fermi level in an n-type semiconductor (b) and in a p-type semiconductor (c) [28].

#### 2.4.2 Properties of Electrolyte – Semiconductor Interface

“As in the previous, for the two conditions being in equilibrium, electrochemical potentials have to be equal. In this respect, the interfaces of photoanode and electrolyte systems needs to be described properly. The the solution’s electrochemical potential might be stated as the electrolyte redox the semiconductor the electrochemical potentials are stated as its Fermi level. When the solution’s redox potential and the the

semiconductor Fermi level are not equal in terms of energy, a charge movement between the semiconductor and the solution provides the equilibrium. Because of the relatively low density of charge carriers, the excess charges located on the semiconductors extend to the photoelectrode from separate distance (10-100 nm) forming *space charge region*”.

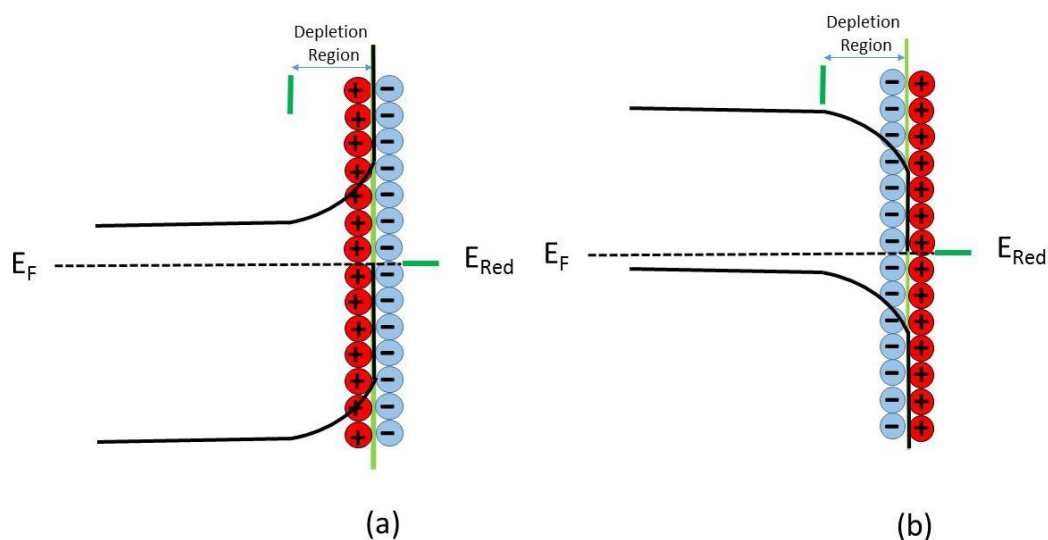


**Figure 2.13** Fermi level in an n-type semiconductor (a) and in a p-type semiconductor (b) [28].

For Fermi Energy level of n-type semiconductor at open circuit must be generally larger than the redox potential of the electrolyte, therefore electrons will move from the electrode to the electrolyte. Hence, there is a positive charge associated with the space charge region that is showed as an upward bending of the band edges (Figure 2.13.a). Since the majority of charge carriers are removed from this region, this is also called depletion layer. On the other hand, a p-type semiconductor has a Fermi level that is typically lower than the redox potential of the electrolyte, thus an electron flow occurs that is from the solution to the electrode. This case generates a negatively charged space that causes a downward bending of the bands. Since the majority of carriers (holes) are removed from this region, the term depletion layer is also used in this case (Figure 2.13.b).

The formation of a space charge region and the band bending is important when the photovoltaic effect is considered. If the semiconductor electrode is exposed to radiation that has required energy, electrons can be excited to the conduction band. When this process occurs in the interior of the semiconductor, recombination of the excited electron and the hole generally occurs, together with the production of heat. On the other hand, at the time it occurs in the space charge region, the existing electrical field will provide the charge separation. For example for an n-type semiconductor, which band edges curve upwards, electron moves to the interior of the semiconductor, at the same time hole moves towards the other side. The hole generally has high energy that can extract an electron from a redox couple present in the electrolyte solution. This case makes n-type semiconductor electrode to act as a photoanode.

Despite the semiconductors are assumed to have both the task of light absorption and charge carrier transportation, in the DSSCs these two functions are separate. Firstly, a sensitizer at the surface of a wide band gap semiconductor absorbs light. Secondly, charge separation takes place in the dye via photo-induced electron injection from the dye into the conduction band of the solid. Carriers are transported through the conduction band of the semiconductor to the charge collector, while the original state of the dye is restored by an electron donor, usually  $I^-/I_3^-$  couple, dissolved in a low volatility organic solvent. Using of transition metal complex based sensitizers having a broad absorption band in conjunction with oxide films of nanocrystalline morphology provides an increase in light harvesting efficiency. It allows achieving near quantitative conversions of incident photons into electric current over a wide spectral range.

### **2.4.3 Mesoporous Oxide Films**

“TiO<sub>2</sub> is a wide band gap semiconductor that has a band gap of 3-3.2 eV, furthermore it is transparent to the visible region of light. TiO<sub>2</sub> is chosen for DSSC applications which is in anatase phase, moreover other wide band gap oxides such as ZnO and Nb<sub>2</sub>O<sub>5</sub> have also given promising results [29, 30]. There are three common phases of

TiO<sub>2</sub> as rutile, anatase and brookite. Rutile has tetragonal lattice in which six oxygen atoms form a distorted octahedral around the titanium with four shorter and two longer Ti-O bonds. Anatase has a slightly different octahedral structure. Anatase to rutile transformation occurs in the temperature range of 700-1000 °C depending on crystal size and impurities. The difference between the two allotropic forms is the band gap which is 3 eV for rutile and 3.2 eV for anatase [31, 32]. The valence band is composed of oxygen 2p orbitals hybridized with titanium 3d orbitals, whereas the conduction band is composed primarily of titanium 3d orbitals [33, 34]. Titanium dioxide is chemically inert, non-toxic and biocompatible. It is easy to produce in large scale at low cost. Due to the high surface affinity toward carboxylates, salicylates, phosphonates and boronates it can be used in dyes, some of them allowing an incident photon/electron conversion efficiency close to unity. TiO<sub>2</sub> mesoporous films are commonly produced via a sol-gel type process involving a hydrothermal step (see experimental section). Figure 2.15 illustrates the morphology of a nanocrystalline TiO<sub>2</sub> layer deposited on a TCO glass and sintered at 450 C° for 30 min produced in this work”.

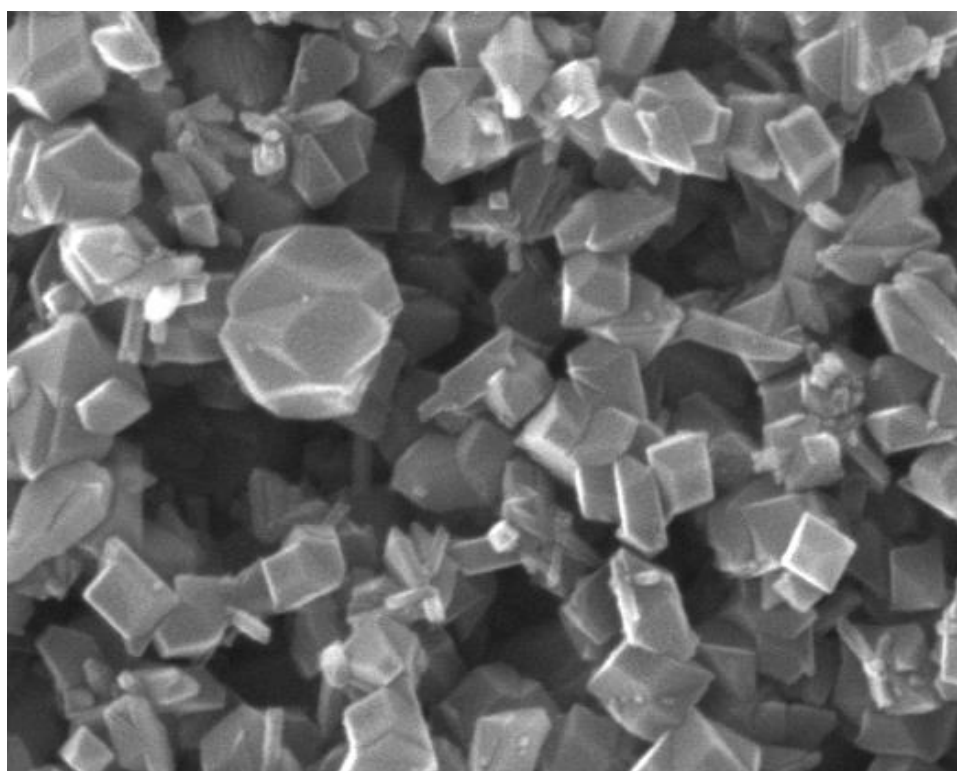


**Figure 2.15** A nanocrystalline TiO<sub>2</sub> layer.

Nanocrystalline morphology of  $\text{TiO}_2$  is a fundamental requirement in determining the solar conversion efficiency. The use of a porous nanostructured film that has high surface roughness affects the light harvesting efficiency. If light penetrates the photo-sensitized porous semiconductor, it interacts with hundreds of adsorbed dye monolayers.

“Therefore photons which has energy close to the absorption maximum of the dye are almost completely absorbed [35]. So that the mesoporous morphology of the film, that consists of nanocrystalline oxide particles with a diameter of 10-20 nm sintered together in order to allow electronic conduction has an important role in the harvesting of sunlight [36]. Depending on the film thickness, their real surface area can be made 100-1000 times larger” [37].

#### **2.4.4 Metal Oxides as Blocking Layer**

The most efficient DSSCs to date are based on Ru(II) made with metal-organic dyes adsorbed on nanocrystalline  $\text{TiO}_2$  and they have an efficiency around 10-11% [38]. The nanocrystalline morphology of the semiconductor metal oxide is not enough, moreover, photoanode have to fulfill a good electron collection capability. For optimizing the electron collection, ratio between the rates of injection and recombination of electron transfer reactions are important.

In order to get a better clarification on electron transfer mechanisms from photo-excited dye to the conduction band of the semiconductor, several studies have been performed on electronic density spatial distribution of Ru(II) polipyridyl compounds [39, 40]. The N3 sensitizer widely used as higher energy conversion efficient sensitizer and other including Ru(II) polipyridyl complexes derives from the spatial separation of the donor LUMO orbital, which is close to the  $\text{TiO}_2$  surface, and the acceptor HOMO level, resulting in injection which is much faster than recombination. Forward

and back electron transfer reactions at the semiconductor – electrolyte interface have been studied by electrochemical methods [41] or by spectroscopic techniques which involve the optical excitation of the sensitizer [42].

“Although these intrinsic properties of Ru(II) based dyes, several efforts have been performed for a long time in order to replace these rare and expensive Ru(II) complexes with the cheaper and environmentally friendly natural dyes [43]”.

However, in natural dyes, this charge density separation is not present and recombination reaction of the photo-injected electrons with oxidized dyes becomes a significant contribution to the loss of efficiency of these devices. In this case, the use of a compact layer between conductive glass and TiO<sub>2</sub> or between TiO<sub>2</sub> and the sensitizer is very useful to minimize the effect of the back recombination reactions on the overall photo conversion efficiency.

Blocking layer of TiO<sub>2</sub> as underlayer was used in order to block the recombination reaction with the back contact. Its function was previously studied by Cameron et al. [44] who verified that the introduction of compact TiO<sub>2</sub> in polipyridyl Ru(II) based dye sensitized solar cells has only marginal effects on conversion efficiencies. More evidences of the effect of this compact layer on the back recombination reaction have been seen using the natural dyes as sensitizers. Graetzel et al. [45] verified that the introduction of a compact layer induces an increase of the overall efficiency from 7 % to 8.6 % under one sun illumination and more than doubled at lower intensities. This is a strong evidence that blocking layer is an insulator against recombination losses.

Moreover the introduction of metal oxides, such as Al<sub>2</sub>O<sub>3</sub>, as over layer between the dye and TiO<sub>2</sub> film was studied in order to block the back recombination not only from the back contact but also from the conduction band of TiO<sub>2</sub> [46, 47]. Al<sub>2</sub>O<sub>3</sub> is an oxide with a band gap of 9 eV and a conduction band level at -4.45 V vs SCE (Standard

Calomel Electrode). Its function is to induce a retardation of interfacial recombination dynamics leading to an improvement in device performances.

“Several studies have also been previously reported that treatment of nanocrystalline TiO<sub>2</sub> with TiCl<sub>4</sub> solutions results in a significant improvement in device performance [48]. This treatment typically results in a significant increase in J<sub>sc</sub> and dye absorption coefficient and ability of electron transport [49]. The enhancement in J<sub>sc</sub> widely observed with the use of this film treatment may derive from a retardation of interfacial recombination process due to the formation of an interfacial blocking layer”.

“All these treatments of photoanode are most effective for improving the efficiency of relatively inefficient devices, with minimal effect on efficient devices in which electron transport through the TiO<sub>2</sub> film is already optimized, thereby preventing significant recombination losses under short circuit conditions. As it will be shown in the results section, these different treatments of the photoanode will be performed (to optimize the performances of the studied dye sensitized solar cells) depending on the sensitizer or the electron transfer mediator that will be tested [50]”.

#### **2.4.5. Dye (Sensitizer)**

In DSSC, excitation of electrons by absorbed photons is produced in sensitizer materials, which are known as dye molecules. If remembering the working principles of DSSC, the sensitizer dye may be expected to not only absorb most of the solar spectrum but also inject all of the photo-generated electrons to the end of photoanode efficiently. Due to most of energy from sun related in the visible region of solar spectrum, sensitizer should have a high incident photon to current efficiency in the range between 400-800 nm. In addition, it is expect to dye sensitizers having higher molar extinction coefficient, that means dye may absorb all incoming light. In order to obtain efficient charge injection to photoanode, energy of the excited state of the dye have to be above conduction band of the metal oxide. Organometallic complexes of ruthenium dyes are mostly used in DSSC.

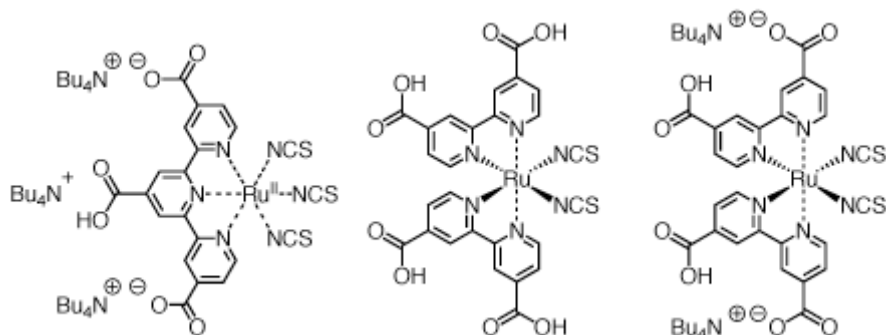


**Figure 2.16** Line-angle chemical structure of black dye, N3 and N719 [51].

Figure 2.16 represents popular molecular structures of different ruthenium based dyes. Adsorption process of dye molecules takes place by chemisorption. The dyes attach to  $\text{TiO}_2$  surface by carboxyl groups. Excitation of electrons occurs from highest occupied molecular orbital (HOMO) of sensitizer, which is close to the metal atom, to the lowest unoccupied molecular orbital (LUMO) which is close to the bipyridine ligands. This configuration is believed to be the reason of ultrafast efficient charge transfer from molecular orbitals of the dye to  $\text{TiO}_2$  conduction band. Another important parameter concerned with dye is the stability of these materials. A suitable sensitizer, which has 20 years life time, should have highest oxidation reduction reaction rate. The new issues about replacement expensive rare earth metal Ru with organic counter parts or quantum dots applications to well absorption of full solar spectrum [52].

#### 2.4.6. Redox Electrolyte System

The simple description usage of electrolyte in DSSC is the medium regeneration material for sensitizer to be ready the next excitation-injection reaction. It acts as a hole conductor as analogous to p-n junction cells. For this purpose, the redox potential must has not only higher vacuum level from HOMO level of sensitizer but also lower the LUMO state than metal oxide's conduction band edge to enhance higher photovoltage due to maximum open circuit voltage is obtained by difference between fermi level of electrons and the redox potential. The redox couple rate of reduction has

to be faster than reduction reactions rate via conduction band electrons or excited state of the dye.

Most common electrolytes include  $I^-/I_3^-$  redox couple where iodide compounds like NaI, KI, LiI up to 0.5 M with iodine  $I_2$  up to 0.1 M are dissolved in organic nitrile solvents. Electrolyte sufficient mobility, ionic conductivity, and solvent's viscosity are three important issue for an efficient electronic transportation due to protection limited diffusion current during the photon to electricity operation. Most solvents used in electrolytes are low viscosity low boiling point solvents. The stability of electrolyte under elevated temperatures limited the cell lifetime due to thermal degradation of it. To prevent thermal degradation and improve stability of DSSC of electrolyte, many studies have been interest to replace volatile solvents with gel electrolytes or ionic liquids. However the highest efficient DSSC are still constructed by low viscosity electrolytes [24, 38, 53].

#### **2.4.7. Photocathode (Counter Electrode)**

Photocathode is an important part of DSSC where Iodide ions are regenerated by recombining with photoelectrons coming over the external load. Rate of regeneration reaction must be very fast to prevent maximum. Therefore, a catalytic thin film might be applied to counter electrode surface that is the interface between electrolyte and TCO. Mostly, a catalytic thin film surface is obtained by a thin film platinum coated on TCO, it is sometimes produced by carbon, nickel or gold. The thickness of film is nearly 100 nm and it can be coated by sputtering, spraying, screen printing or evaporation techniques. To reduce the production cost of DSS, carbon can be used as an alternative photocathode material, in addition due to carbon materials having highly surface area, it can be easily compare its catalytic activity to platinum [20, 54].

## REFERENCES

1. Becquerel, E., *Recherche sur les e est de la radiation chimique de la lumi ere solaire, au moyen des courants electriques*. Comptes rendus hebdomadaires des s eances de l'Acad emie des Sciences, (9): p. 4. 1839.
2. Cohen, I.B. and A. Einstein, *An Interview with Einstein*. Scientific American, **193**(1): p. 69-73. 1955.
3. Planck M., *Ueber das Gesetz der Energieverteilung im Normalspectrum*. Annalen der Physik, **4**: p. 10. 1901
4. Luque, A., *Handbook of Photovoltaic Science and Engineering*. John Wiley & Sons, 2003.
5. Wurfel, P., *Weinheim 2nd edition Wiley-Vch*, 2009.
6. Wenger, S., *Strategies to Optimizing Dye-Sensitized Solar Cells: Organic Sensitizers, Tandem Device Structures, and Numerical Device Modeling*. PhD thesis École Polytechnique Federale De Lausanne, 2010.
7. Shockley, W. and H.J. Queisser, *Detailed Balance Limit of Efficiency of P-N Junction Solar Cells*. Journal of Applied Physics, **32**(3): p. 510.1961.
8. Green, M.A., et al., *Solar cell efficiency tables (version 36)*. Progress in Photovoltaics, **18**(5): p. 346-352. 2010.
9. Goetzberger, A., C. Hebling, and H.W. Schock, *Photovoltaic materials, history, status and outlook*. Materials Science & Engineering R-Reports, **40**(1): p. 1-46. 2003.
10. Reddy, P.J., *Science and Technology of Photovoltaics, 2nd edition*. CRC Press, 2010.
11. Brown, A.S. and M.A. Green, *Detailed balance limit for the series constrained two terminal tandem solar cell*. Physica E-Low-Dimensional Systems & Nanostructures, **14**(1-2): p. 96-100. 2002.
12. Marti, A. and G.L. Araujo, *Limiting efficiencies for photovoltaic energy conversion in multigap systems*. Solar Energy Materials and Solar Cells, **43**(2): p. 203-222. 1996.

13. King, R.R., *Proceedings. 24th European Photovoltaic Solar Energy Conference*, 2009.
14. Cotal, H., et al., *III-V multijunction solar cells for concentrating photovoltaics*. *Energy & Environmental Science*, **2**(2): p. 174-192.2009.
15. Romeo, A., et al., *Development of thin-film Cu(In,Ga)Se<sub>2</sub> and CdTe solar cells*. *Progress in Photovoltaics*, **12**(2-3): p. 93-111. 2004.
16. Shah, A.V., et al., *Thin-film silicon solar cell technology*. *Progress in Photovoltaics*, **12**(2-3): p. 113-142. 2004.
17. Todorov, R., et al., *Multilayer As<sub>2</sub>Se<sub>3</sub>/GeS<sub>2</sub> quarter wave structures for photonic applications*. *Journal of Physics D-Applied Physics*, **43**(50). 2010.
18. Kietzke, T., et al., *Effect of annealing on the characteristics of organic solar cells: Polymer blends with a 2-vinyl-4,5-dicyanoimidazole derivative*. *Macromolecules*, **40**(13): p. 4424-4428. 2007.
19. Gratzel, M., *Solar energy conversion by dye-sensitized photovoltaic cells*. *Inorganic Chemistry*, **44**(20): p. 6841-6851. 2005.
20. Cosar, B., et al., *Photovoltaic performance of bifacial dye sensitized solar cell using chemically healed binary ionic liquid electrolyte solidified with SiO<sub>2</sub> nanoparticles*. *Electrochimica Acta*, **87**: p. 425-431. 2013.
21. Memming, R., *Electron-Transfer Process with Excited Molecules at Semiconductor Electrodes*. *Progress in Surface Science*, **17**(1): p. 7-73. 1984.
22. Zabri, H., et al., *Efficient osmium sensitizers containing 2,2'-bipyridine-4,4'-bisphosphonic acid ligand*. *Journal of Photochemistry and Photobiology a-Chemistry*, **166**(1-3): p. 99-106. 2004.
23. Altobello, S., et al., *Sensitization of TiO<sub>2</sub> with ruthenium complexes containing boronic acid functions*. *Journal of Photochemistry and Photobiology a-Chemistry*, **166**(1-3): p. 91-98. 2004.
24. Nazeeruddin, M.K., et al., *Engineering of efficient panchromatic sensitizers for nanocrystalline TiO<sub>2</sub>-based solar cells*. *Journal of the American Chemical Society*, **123**(8): p. 1613-1624. 2001.
25. Nusbaumer, H., et al., *Co-II(dbbiP)(2)(2+) complex rivals tri-iodide/iodide redox mediator in dye-sensitized photovoltaic cells*. *Journal of Physical Chemistry B*, **105**(43): p. 10461-10464. 2001.

26. Anderson, N.A. and T. Lian, *Ultrafast electron injection from metal polypyridyl complexes to metal-oxide nanocrystalline thin films*. Coordination Chemistry Reviews, **248**(13-14): p. 1231-1246. 2004.
27. Hannay, N.B., *Semiconductors*. Reinhold Publishing Corporation, 1959.
28. Cazzanti, S., [eprints.unife.it/125/7/Chapter2.pdf](http://eprints.unife.it/125/7/Chapter2.pdf). 2009.
29. Tennakone, K., et al., *An efficient dye-sensitized photoelectrochemical solar cell made from oxides of tin and zinc*. Chemical Communications, (1): p. 15-16. 1999.
30. Sayama, K., H. Sugihara, and H. Arakawa, *Photoelectrochemical properties of a porous Nb<sub>2</sub>O<sub>5</sub> electrode sensitized by a ruthenium dye*. Chemistry of Materials, **10**(12): p. 3825-3832. 1998.
31. Bickley, R.I. and L.P. Metcalfe, *Interaction of Oxygen with Zinc Surfaces*. Journal of the Chemical Society-Faraday Transactions I, **74**: p. 869-882. 1978.
32. Glassford, K.M. and J.R. Chelikowsky, *Optical-Properties of Titanium-Dioxide in the Rutile Structure*. Physical Review B, **45**(7): p. 3874-3877. 1992.
33. Silvi, B., et al., *Pseudopotential Periodic Hartree-Fock Study of Rutile TiO<sub>2</sub>*. Journal of Physics and Chemistry of Solids, **52**(8): p. 1005-1009. 1991.
34. Glassford, K.M. and J.R. Chelikowsky, *Structural and Electronic-Properties of Titanium-Dioxide*. Physical Review B, **46**(3): p. 1284-1298. 1992.
35. Oregan, B. and M. Gratzel, *A Low-Cost, High-Efficiency Solar-Cell Based on Dye-Sensitized Colloidal TiO<sub>2</sub> Films*. Nature, **353**(6346): p. 737-740. 1991.
36. Barbe, C.J. and M. Graetzel, *Mesoporous TiO<sub>2</sub> electrodes for photoelectrochemical applications*. Abstracts of Papers of the American Chemical Society, **213**: p. 316. 1997.
37. Barbe, C.J., et al., *Nanocrystalline titanium oxide electrodes for photovoltaic applications*. Journal of the American Ceramic Society, **80**(12): p. 3157-3171. 1997.
38. Nazeeruddin, M.K., et al., *Raman Characterization of Charge-Transfer Transitions in Ligand-Bridged Binuclear Polypyridyl Complexes of Ruthenium(II)*. Journal of the Chemical Society-Dalton Transactions, (2): p. 323-325. 1993.

39. Fantacci, S., et al., *Photophysical properties of [Ru(phen)(2)(dppz)](2+) intercalated into DNA: An integrated Car-Parrinello and TDDFT study*. Journal of the American Chemical Society, **127**(41): p. 14144-14145. 2005.
40. Fantacci, S., F. De Angelis, and A. Selloni, *Absorption spectrum and solvatochromism of the [Ru(4,4 '-COOH-2,2 '-bPY)(2)(NCS)(2)] molecular dye by time dependent density functional theory*. Journal of the American Chemical Society, **125**(14): p. 4381-4387. 2003.
41. Peter, L.M., et al., *Transport and interfacial transfer of electrons in dye-sensitized nanocrystalline solar cells*. Journal of Electroanalytical Chemistry, **524**: p. 127-136. 2002.
42. Haque, S.A., et al., *Parameters influencing charge recombination kinetics in dye-sensitized nanocrystalline titanium dioxide films*. Journal of Physical Chemistry B, **104**(3): p. 538-547. 2000.
43. Cherepy, N.J., et al., *Ultrafast electron injection: Implications for a photoelectrochemical cell utilizing an anthocyanin dye-sensitized TiO<sub>2</sub> nanocrystalline electrode*. Journal of Physical Chemistry B, **101**(45): p. 9342-9351. 1997.
44. Cameron, P.J., L.M. Peter, and S. Hore, *How important is the back reaction of electrons via the substrate in dye-sensitized nanocrystalline solar cells?* Journal of Physical Chemistry B, **109**(2): p. 930-936. 2005.
45. Burke, A., et al., *The function of a TiO<sub>2</sub> compact layer in dye-sensitized solar cells incorporating "Planar" organic dyes*. Nano Letters, **8**(4): p. 977-981. 2008.
46. Palomares, E., et al., *Slow charge recombination in dye-sensitised solar cells (DSSC) using Al<sub>2</sub>O<sub>3</sub> coated nanoporous TiO<sub>2</sub> films*. Chemical Communications, (14): p. 1464-1465. 2002.
47. Palomares, E., et al., *Control of charge recombination dynamics in dye sensitized solar cells by the use of conformally deposited metal oxide blocking layers*. Journal of the American Chemical Society, **125**(2): p. 475-482. 2003.
48. Zhang, D.S., et al., *Nanocrystalline TiO<sub>2</sub> electrodes prepared by water-medium screen printing technique*. Chemistry Letters, (10): p. 1042-1043. 2001.

49. Kambe, S., et al., *Effects of crystal structure, size, shape and surface structural differences on photo-induced electron transport in TiO<sub>2</sub> mesoporous electrodes*. Journal of Materials Chemistry, **12**(3): p. 723-728. 2002.
50. Park, N.G., et al., *Dye-sensitized TiO<sub>2</sub> solar cells: Structural and photoelectrochemical characterization of nanocrystalline electrodes formed from the hydrolysis of TiCl<sub>4</sub>*. Journal of Physical Chemistry B, **103**(17): p. 3308-3314. 1999.
51. İçli, K.Ç., *Core- Shell Type Nanocrystalline FTO Photoanodes For DSSC*, Msc. Thesis, FBE-METU, 2010.
52. Gratzel, M., *Conversion of sunlight to electric power by nanocrystalline dye-sensitized solar cells (vol 164, pg 3, 2004)*. Journal of Photochemistry and Photobiology a-Chemistry, **168**(3): p. 235-235. 2004.
53. Nazeeruddin, M.K., et al., *Investigation of sensitizer adsorption and the influence of protons on current and voltage of a dye-sensitized nanocrystalline TiO<sub>2</sub> solar cell*. Journal of Physical Chemistry B, **107**(34): p. 8981-8987. 2003.
54. Bisquert, J., *Chemical diffusion coefficient of electrons in nanostructured semiconductor electrodes and dye-sensitized solar cells*. Journal of Physical Chemistry B, **108**(7): p. 2323-2332. 2004.



## CHAPTER 3

### EXPERIMENTAL

During this work, in order to obtain high efficient dye sensitized solar cells (DSSC) by low cost chemical process, all of the parts of photoanode were synthesized by sol-gel methods. Polymerized complex combustion method and hydrothermal modified sol gel techniques were used to produce conductive thin film coated glass, nanowires, nanosized particles and scattering particles with desired morphologies.

In order to obtain Zr-modified TiO<sub>2</sub> nanoparticles, modified hydrothermal sol gel method was used containing solutions of different Zr-TiO<sub>2</sub> concentrations. For comparison with Zr modified based cells, bare titanium dioxide films are also produced using commercial nanoparticles purchased from Evonik®. After paste production steps, the procedure of which is given in this chapter, screen-printing technique is performed to obtain nanoporous thick films on TCO. Experimental procedures could be categorized under the following steps:

- TCO synthesis
- TCO medication
- Absorber, scattering particle synthesis
- Thick film deposition
- Scattering layer deposition
- Dye sensitized solar cell assembly

Characterizations of the powders and films include XPS, SEM, four probe resistivity measurements, BET, X-ray diffraction and chemical impedance spectroscopy. After

production of DSSCs, photovoltaic performances were measured under simulated AM 1.5 light.

### **3.1. Particle Synthesis**

To produce modified and bare semiconductor particles for DSSC, an appropriate particle synthesis technique to obtain nanopowders with enhanced surface morphologies and composition is essential. Economic chemistry methods such as Sol-gel are a key for low cost production to synthesize semiconductor nanoparticles of various compounds. In this study, two different sol gel techniques such as polymerized complex combustion method and hydrothermal modified sol-gel techniques are used.

#### **3.1.1. Polymerized Complex Combustion Method**

Modified Pechini technique is known as polymerized complex combustion method (PCCM) different from other wet chemical techniques which consists of inorganic complex chelated agents with the organic or inorganic precursor (PCS). After mixing dissolved ions with PCS, the nano pre-particles are obtained including metal oxide nanoparticles. To produce dried powders, heat treatment was applied until a roasted powders formed. They are heat treated at a higher temperature (450°C) to decompose organic polymers and reach the crystallization of the powders [1].

#### **3.1.2. Hydrothermal Modified Sol-Gel Techniques**

Hydrothermal modified sol-gel technique is a new type sol-gel method to produce nanoparticles from organic or inorganic raw materials. Hydrothermal modified sol-gel techniques have many advantages compared to basic wet chemical techniques due to its having extreme higher pressures with higher temperatures and allows many compounds to be synthesized in solvents having low boiling points from chlorides, alkoxides etc [2,3]. For hydrothermal treatments applied, a titanium Gr95 pressure vessel (AmAr equipments) was used as an autoclave (Figure 3.1). All parts of autoclave including the connectors are coated with Teflon. A thermo well and a port connected to a manometer are on the top and the autoclave is sealed via titanium clamps to measure temperature and pressure inside the vessel. The autoclave is conducted by an auto control heating unit and a mechanical stirrer.



**Figure 3.1** Titanium autoclave used in hydrothermal technique (AmAr Equipments).

In this study, hydrothermal treatment and modified sol-gel method were carried out to obtain semiconductor nanoparticles which will be discussed in chapters 5, 6, 7, and 8.

### **3.2. Deposition of Thick Films**

Thick films of semiconductor nanopowders were deposited on TCO by screen printing technique. The type of TCO glasses are used in chapter 6 and 7 are fluorine doped tin dioxide purchased from Pilkington (TEC 15) which have a sheet resistance of 15 ohm/sq and a visible-light transparency values nearly 90% according to our experiments given in chapter 6. The other TCOs which are ITO substrates were produced in our lab using spin coater by sol-gel techniques.

Deposition of thick films can be done in several steps:

- Cleaning of the TCO glasses
- Blocking layer applied on TCO
- Screen printing pastes production
- Screen printing of absorber layer
- Screen printing of scattering layer
- Annealing (heat treatment)
- Characterization

### **3.2.1. Screen Printing Pastes Production**

Deposition of synthesized nanopowders was achieved by screen printing the pastes containing the powders of covetable nanoparticles. The screen printing pastes are composed of semiconductor nanopowders in dispersion in an organic based high viscosity fluid. The particles and fluid are blended together to form a mechanically and chemically stable material before sintering. In this study, semiconductor metal oxide nanoparticles were dispersed with ethyl cellulose binder and carrier mixture (ethanol) in terpineol.

The steps used in the production of paste are given as follows:

- 2 gr of semiconductor nanopowders are grinded in mortar
- 100 ml ethanol and 1 ml acetic acid mixture are added in mortar
- The homogenous colloid is transferred to Teflon beaker
- The solution is sonicated and stirred for 30 min
- 1 gr ethyl cellulose and 7 gr terpineol are added to solution
- Excess ethanol is evaporated at 40°C for 6 h
- A highly viscous paste containing semiconductor metal oxide nanopowders is obtained.

### **3.2.2. Substrate Cleaning**

In order to provide the adhesion of thick films on TCO substrate, the TCO should be cleaned properly to remove organic contaminants and dust. The cleaning of substrate is given in the following steps:

- TCOs are sonicated in detergent solution for 20 min in ultrasonic bath
- TCOs are rinsed thrice in ultrasonic bath
- TCOs are sonicated in acetone for 10 min
- TCOs are rinsed twice in ultrasonic bath
- TCOs are treated in ethanol twice in ultrasonic bath
- TCOs are kept in ethanol solution until deposition to have clean and inclusion free surfaces

### **3.2.3. Screen Printing of Pastes**

Screen printing that is economical and reproducible technique to manufacture thick films, is a well-recognized deposition technique for a long time and is also referred as serigraphy where a silk screen is used. It can be a favorable method to coat thick films on different substrates quickly such as the ones used in sensor technology.

Amounts of paste deposited on substrate depend on the thickness of the fabrics. However, the final thickness of the film illustrated with the concentration of desired powders. Figure 3.2 shows stages of screen printing deposition.

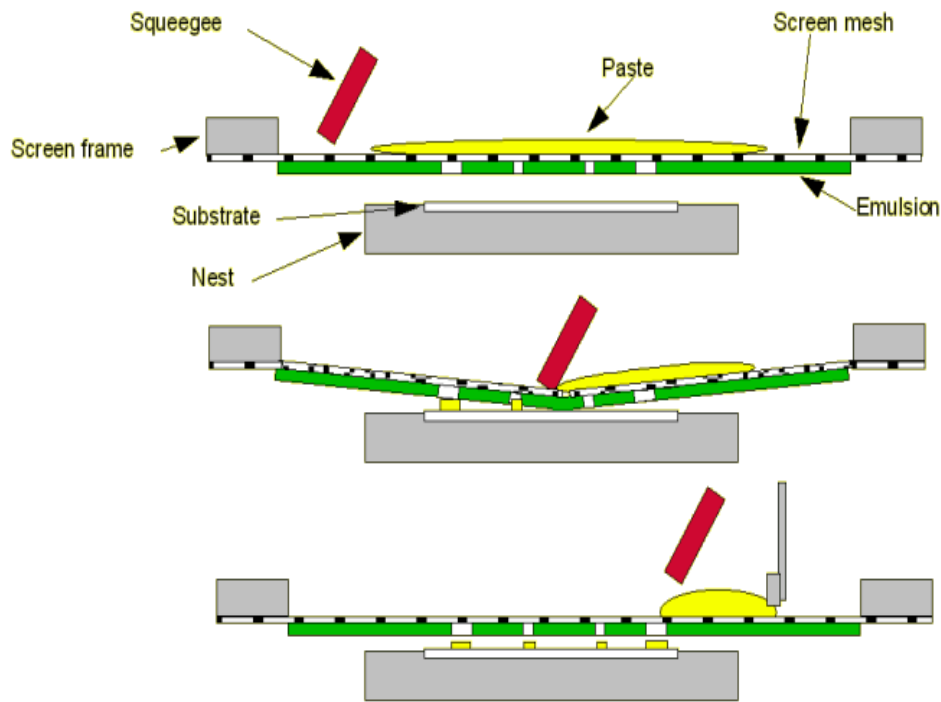


**Figure 3.2** Steps of screen printing deposition process [4].

In this work, a polyester based 90 mesh material stretched in a aluminum frame is used as the screen for deposition of absorber layer (Figure 3.2). 10x10 mm and 5x5 mm square patterns used as the template for film deposition, were manufactured by photo emulsion technique on the screen, as shown in Figure 3.3. The thick film deposition by screen printing technique can be done on TCO by rubber squeegee to obtain the desired thickness. All deposition processes were performed in a dust free clean room conditions to reduce surface irregularities caused by the fabrics. The deposition can be repeated to achieve the desired thickness. The deposited samples are dried at 120°C for 15 min in a vacuum oven after each paste deposition to remove volatile components of the pastes and this drying procedure was applied before each coating step and final heat treatment.



**Figure 3.3** aluminium screen used during screen printing deposition [5].

#### **3.2.4. Heat Treatment of Films**

Screen printed thick films must be heat treated to remove organic compounds in the film and to obtain the desired semiconductor network by sintering of particles. Heat treatment programs must be chosen carefully to prevent over-sintering which results in softening of soda lime glass, particle growth and reduction of porosity. The maximum temperature has to be limited around 500°C for sintering of titanium and zirconium oxides. The heating rate of the films is another important parameter. The samples should be prevented from sudden changes in temperature, because the thermal stress can cause cracks on the film and peeling off from surface. Organic binders have to burn completely to prevent from organic residues being trapped between interconnected particles which are known as a reason of recombination. The heat treatment applied in 4 zone oven (Dyesol Company) under open atmosphere using the following program:

- Films were first heated to 325°C with a heating rate of 10°C /min
- Films kept at 325°C for 15 minutes.
- Films kept at 375°C for 15 minutes
- Films kept at 500°C for an hour.

### **3.2.5. Characterization**

Surface morphology of the films and their cross sections for thickness measurements were studied by FEI Quanta 400 FEG field emission SEM in Central Laboratory, METU. To determine optical properties, Varian UV-1900 UV-Visible spectrophotometer was used in visible region from 300 to 800 nm. Rigaku D/Max 2200/PC diffractometer are used for X-Ray diffraction analysis in the Metallurgical and Materials Engineering Department (METE) of METU. Electrical properties such as resistivity measurements of powders were measured by a Jandel universal four point probe equipped with a Keithley 182 digital voltmeter and Keithley 238 high current source, in Surface Science Research Laboratory of METE of METU. XPS studies were performed in Central Laboratory at METU and EIS analysis by Gamry G300-zwpinwin software with 1 sun illumination.

### **3.3. Electrical Characterizations of Films**

Electrical characterization of the powders has been performed by standard four-point probe technique to understand the effect of modifications on the electrical properties of each photoanode layer.

### **3.4. Assembly of DSSC**

According to literature, DSSCs were assembled in a sandwich configuration. In this work, Zr-modified semiconductor nanoparticles and commercial P25 TiO<sub>2</sub> materials employed as photoanodes, platinum-coated TCOs were employed as counter electrodes, and tri iodide in acetonitrile was employed as liquid gel type electrolyte.

#### **3.4.1. Dye Staining**

The prepared photoanodes were kept in commercially purchased N719 dye dissolved in anhydrous acetonitrile with a molarity of 50 mM for 24 h to ensure dye absorption in the dark. The dye loader vessel was sealed with parafilm to prevent it from water or dust contamination. Films were directly dipped into this solution horizontally and completely sunk in dye solution. Water contamination is a risk for dye absorption

stage. The inhibition of water contamination during the dye absorption of photoanode was ensured such that TiO<sub>2</sub> films were slowly sunk into the dye solution when their temperature is around 100°C after last heat treatment process. After the dye loading stage, the dye absorbed photoanodes were washed by excess absolute ethanol to remove unabsorbed dye molecules. When the cleaning procedure was complete, they were immediately used as DSSC photoanodes.

### **3.4.2. Counter Electrode Preparation**

Counter electrode of DSSC containing a thin layer of platinum having a catalyzed surface for electrolyte regeneration has been produced using a platinum precursor containing solution applied on TCO coated substrates. A 1 mm diameter hole was drilled on the FTO glasses by water jet in order to inject the electrolyte to the sealed cell. The same cleaning procedure as used on photoanode deposition was applied to all TCOs of counter electrodes before platinum coating stage. A drop of platinum precursor solution was applied on TCO glass substrates and it was spreaded all over the entire surface with a glass rod at 450 °C in open atmosphere oven. The reaction was complete in 15 min for the coating of a layer of platinum nanoclusters deposited on the TCO glass. The counter electrodes are sensitive to moisture and oxygen, therefore they are immediately used for the construction of DSSCs.

### **3.4.3. Cell Assembly and Characterization**

The counter and working electrodes are laminated together by 50 µm Surlyn films. The width of the edges of the frames was 1 mm. Working area of DSSCs were 0.25 cm<sup>2</sup> in this study (Figure 3.4). The assembly procedure of DSSC are given in the following steps:

- Surlyn films are cut into frames as same size active areas,
- Surlyn films were placed on counter electrode,
- The working electrode is placed on the counter electrode,
- The electrodes are laminated by Dyesol laminator at 110 °C for 3 minutes,
- The sample is cooled down to room temperature,

- Redox electrolyte is introduced into the cells from the predrilled hole on the counter electrode under vacuum,
- A drop of UV curing sealer was introduced into the hole,
- The cell was treated under UV light until curing of sealer,
- The hole was then sealed with a piece of Surlyn,
- Silver paste that dissolved in isobutyl methyl ketone was applied on both electrodes of sample as silver contacts.

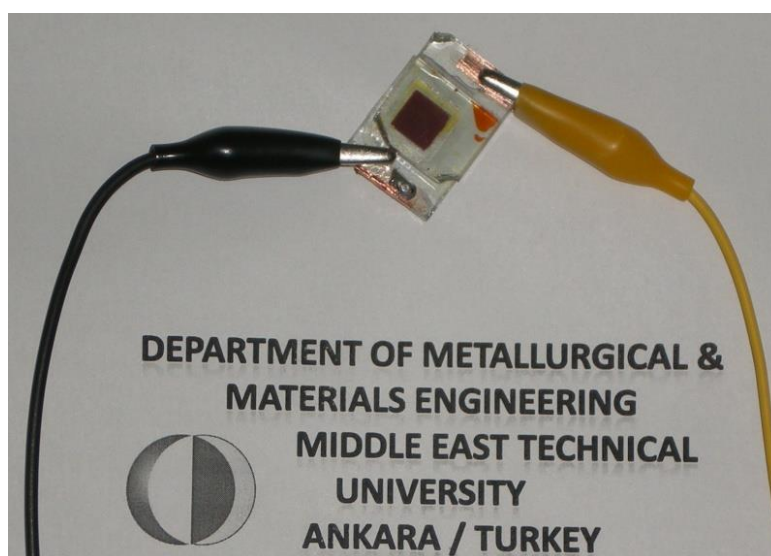


**Figure 3.4** A typical dye sensitized solar cell.

#### **3.4.4. Measurement of Dye Loading Capacity of DSSC**

The amounts of dye adsorbed on  $\text{TiO}_2$  surface were spectroscopically estimated. The concentration of dye solution is quantified by Uv-Vis spectrometer at 550 nm. The dye adsorbed on the film is desorbed from the film by soaking in 0.1 M KOH solution for 2 h. The amount of dye on  $\text{TiO}_2$  film was estimated from the absorption spectrum in 0.1 M KOH solution at 500 nm compared with quantified dye solution spectra with a known concentration.

### 3.5. Impedance Spectroscopy

Impedance spectroscopy can be given as a fundamental tool used for the study of electrochemical systems in corrosion, optical and solid-state systems. The electrochemical impedance instrument is a suitable method to interpret the results correctly by the use of an electrical model. Impedance spectroscopy is also called AC Impedance. Therefore, the complex working mechanism of DSSC can be clarified wholly for all types of DSSCs. It means that, the dielectric and electric properties of individual contributions of components under investigation can be distinguished. The role of each component can be explained in different conditions such as under dark or illumination. In addition, it is very useful technique for DSSC applications because DSSC is basically a redox electrochemical cell. Being a non-destructive technique, time dependent information about the properties of components can be measured e.g. the electrochemical reactions in batteries, fuel cells, or solar cells. If the behavior of each component of DSSC is required such as resistances and capacitances for each part, they can be determined by suitable modeling of electrochemical data [6].

It has some advantages as given below:

- Time dependent data (frequency vs R or C) is available
- Nondestructive technique
- Applied on high resistance materials easily
- Quantitative data available

Although it has some advantages, it is still too expensive, and it is hard to analyze the complex data for quantification. The modeling of electrochemical data is accomplished using theoretical electrical circuit built from component resistors and capacitors to represent electrochemical behavior of each part of DSSCs. Any changes in the values for individual components can be interpreted as their performance of electrochemical behavior. Schematic descriptions of an EIS device measurement system and Nyquist plots are given in Figure 3.5.

On the Nyquist plot, the impedance can be described as the length vector  $|Z|$ . The angle between this vector and the x-axis is  $\phi$ . Low frequency data are on the right side of the

plot and higher frequencies are on the left. This is true for *EIS* data where impedance usually falls as frequency rises (this is not true of all circuits).

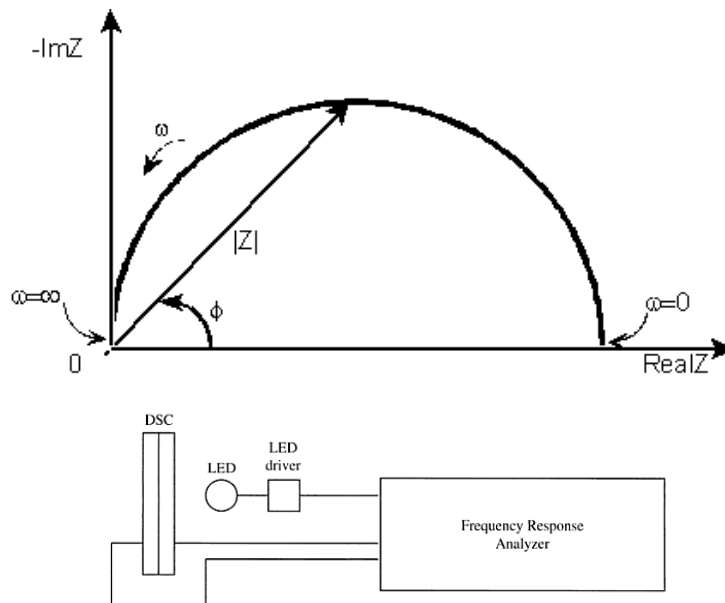


**Figure 3.5** Simple Nyquist plot a) and schematic for an impedance device (b).

The equation for  $Z(\omega)$  is composed of an imaginary part and a real part. If the imaginary part on the Y-axis, which is negative and the real part is plotted on the X-axis of a graph, we can find a Nyquist plot of electrochemical system by EIS.

$$Z = \frac{E}{I} = Z_0 \exp(i\phi) = Z_0 (\cos \phi + i \sin \phi) \dots\dots\dots (3.1)$$

The Z can be illustrated with R and C component of EIS

$$\frac{1}{Z} = \frac{1}{R} + \frac{1}{i\omega C} \dots\dots\dots (3.2)$$

The impedance spectra of DSSC at different applied potentials are given in Figure 3.6. The best technique is EIS applied on  $V_{oc}$  of DSSC.

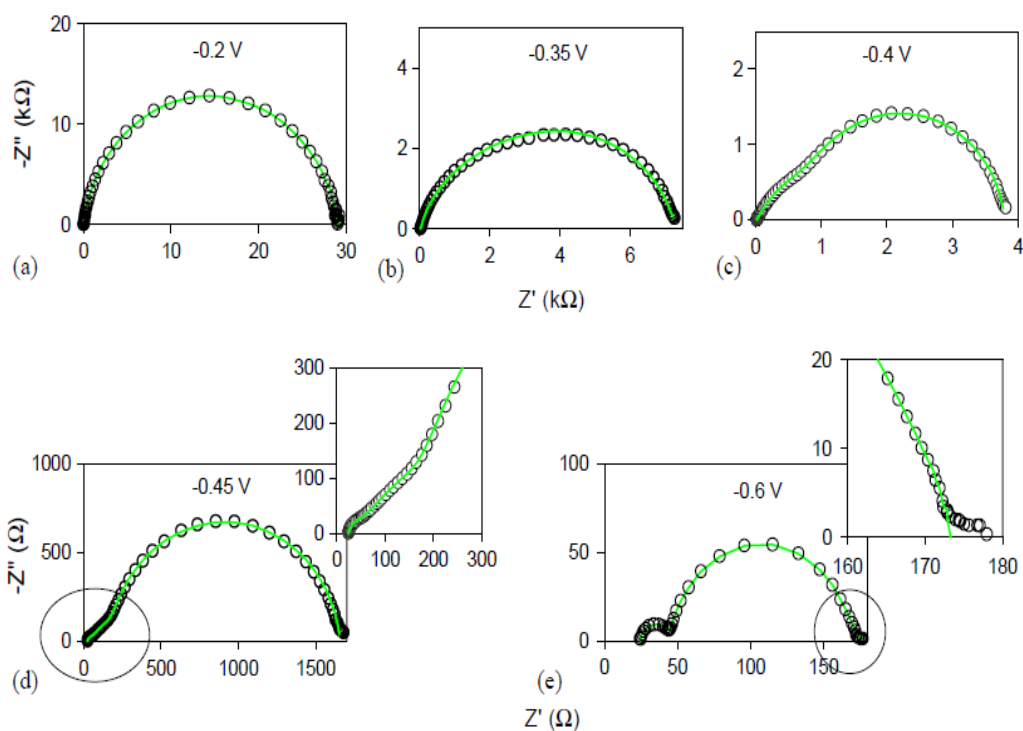


**Figure 3.6** Nyquist plots of a dye-sensitized solar cell, at different applied potentials [7].

Experimental data (example as Figure 3.6.) can be fitted to the model represented by the equivalent circuit shown in Figure 3.7. The schematic description of the network of  $\text{TiO}_2$  colloids is clarified as a columnar model. The equivalent circuit elements have the following meaning as given in Table 3.1.

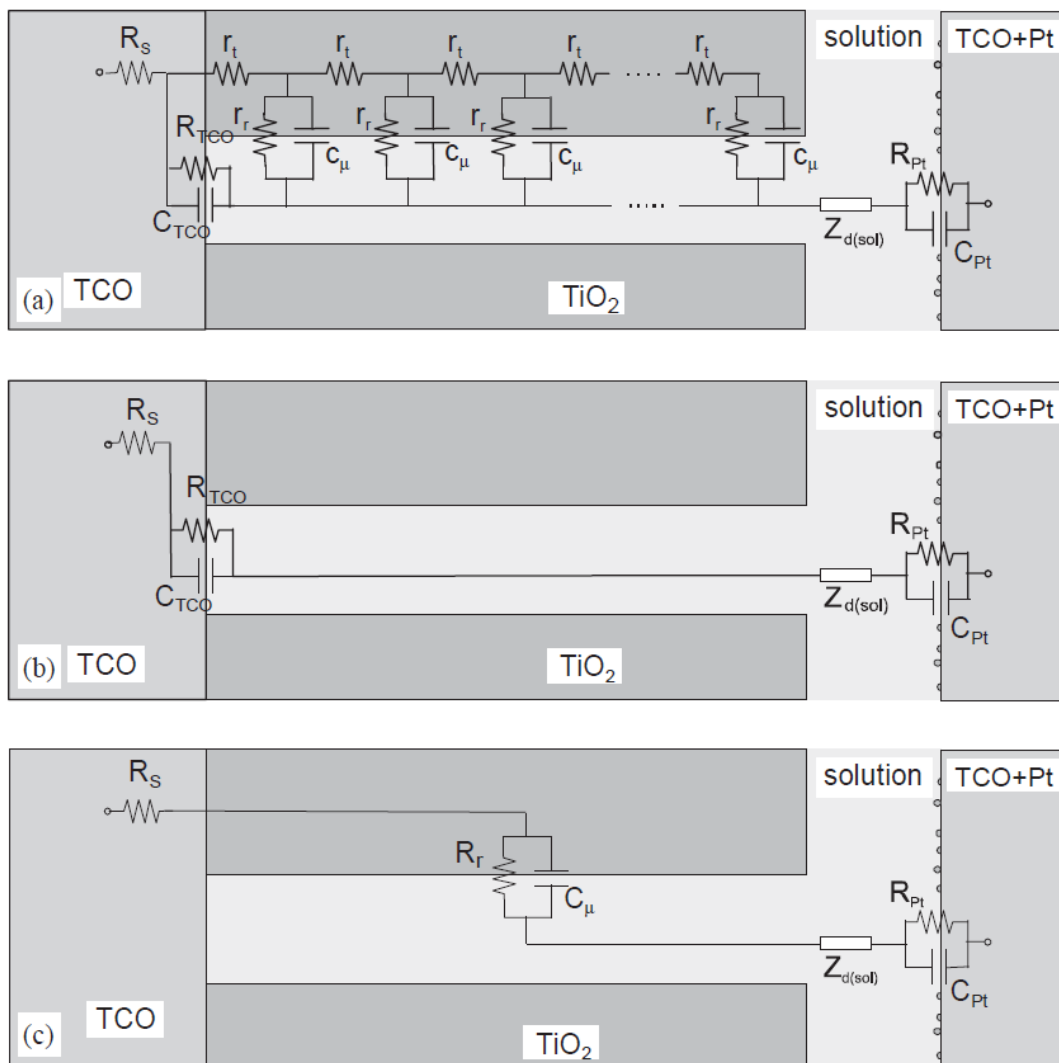


**Figure 3.7** The schematic description of possible electrochemical modeling on DSSC: Equivalent circuit for a complete solar cell (a). Clarified electrical circuit for under 0 V potentials for TiO<sub>2</sub>, as currents are low,  $Z_d$  is neglected. (b), and electrical circuit for TiO<sub>2</sub> under conductive conditions(c) [7].

**Table 3.1.** The equivalent circuit elements on EIS

<b>Elements of EIS</b>	<b>Description</b>
$C_{\mu}$	The chemical capacitance stands for the change of electron density as a function of the Fermi level [6]
$R_t$	The resistance of electron transport [8]
$R_r$	Resistance of Charge-transfer conducted to electrons recombination at the $TiO_2$ /electrolyte interface
$R_s$	Series- transport - resistance of the TCO
$R_{TCO}$	Charge-transfer resistance for electron recombination at the TCO to the electrolyte
$C_{TCO}$	The capacitances at TCO/ $TiO_2$ /electrolyte interfaces [9]
$Z_d(sol)$	The impedance of diffusion of redox species in the electrolyte [10, 11]
$R_{Pt}$	Charge-transfer resistance at photocathode [12, 13]
$C_{Pt}$	The interfacial capacitance at the counter electrode/electrolyte interface

The Bode plot is the popular method to determine recombination time by the maximum frequency calculations. The impedance is plotted with logarithmic frequency on the x-axis and both the absolute value of the impedance ( $|Z| = Z_0$ ) and phase-shift on the y-axis. The Bode plot for the RC circuit is given in Figure 3.8. The Bode plots have frequency information unlike the Nyquist plots.

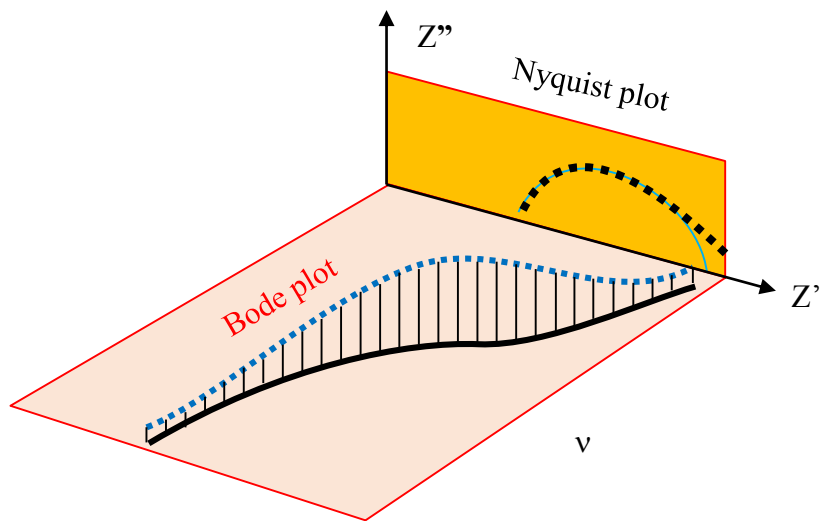


**Figure 3.8** Schematic description differences from Nyquist and Bode plots.

In Figure 3.8, the impedance data are shown as the blue points. Their projection onto the  $Z^I$ - $Z^{II}$  plane is named as the Nyquist plot that is described before. The projection onto the  $Z^{II}$  - $\nu$  (frequency) plane is named as the Bode Plots.

## REFERENCES

1. Bagheri-Mohagheghi, M.M., et al., *The effect of the post-annealing temperature on the nano-structure and energy band gap of SnO<sub>2</sub> semiconducting oxide nano-particles synthesized by polymerizing-complexing sol-gel method*. Physica B-Condensed Matter, **403**(13-16): p. 2431-2437. 2008.
2. Kitiyanan, A., et al., *The preparation and characterization of nanostructured TiO<sub>2</sub>-ZrO<sub>2</sub> mixed oxide electrode for efficient dye-sensitized solar cells*. Journal of Solid State Chemistry, **178**(4): p. 1044-1048. 2005.
3. Kitiyanan, A. and S. Yoshikawa, *The use of ZrO<sub>2</sub> mixed TiO<sub>2</sub> nanostructures as efficient dye-sensitized solar cells' electrodes*. Materials Letters, **59**(29-30): p. 4038-4040. 2005.
4. [http://www.gwent.org/gem\\_screen\\_printing.html](http://www.gwent.org/gem_screen_printing.html).
5. İçli, K.Ç., *Core- Shell Type Nanocrystalline FTO Photoanodes For DSSC*, Msc. Thesis, FBE-METU, 2010.
6. Bisquert, J., et al., *Physical chemical principles of photovoltaic conversion with nanoparticulate, mesoporous dye-sensitized solar cells*. Journal of Physical Chemistry B, **108**(24): p. 8106-8118. 2004.
7. Fabregat-Santiago, F., et al., *Influence of electrolyte in transport and recombination in dye-sensitized solar cells studied by impedance spectroscopy*. Solar Energy Materials and Solar Cells, **87**(1-4): p. 117-131. 2005.
8. Bisquert, J. and V.S. Vikhrenko, *Interpretation of the time constants measured by kinetic techniques in nanostructured semiconductor electrodes and dye-sensitized solar cells*. Journal of Physical Chemistry B, **108**(7): p. 2313-2322. 2004.
9. Fabregat-Santiago, F., et al., *Mott-Schottky analysis of nanoporous semiconductor electrodes in dielectric state deposited on SnO<sub>2</sub>(F) conducting substrates*. Journal of the Electrochemical Society, **150**(6): p. E293-E298. 2003.

10. Hauch, A. and A. Georg, *Diffusion in the electrolyte and charge-transfer reaction at the platinum electrode in dye-sensitized solar cells*. *Electrochimica Acta*, **46**(22): p. 3457-3466. 2001.
11. Kern, R., et al., *Modeling and interpretation of electrical impedance spectra of dye solar cells operated under open-circuit conditions*. *Electrochimica Acta*, **47**(26): p. 4213-4225. 2002.
12. Han, L.Y., et al., *Modeling of an equivalent circuit for dye-sensitized solar cells*. *Applied Physics Letters*, **84**(13): p. 2433-2435. 2004.
13. van de Lagemaat, J., N.G. Park, and A.J. Frank, *Influence of electrical potential distribution, charge transport, and recombination on the photopotential and photocurrent conversion efficiency of dye-sensitized nanocrystalline TiO<sub>2</sub> solar cells: A study by electrical impedance and optical modulation techniques*. *Journal of Physical Chemistry B*, **104**(9): p. 2044-2052. 2000.

## CHAPTER 4

### AN ALTERNATIVE PATH OF PRODUCING HIGHLY TRANSPARENT AND LOW RESISTANCE INDIUM TIN OXIDE (ITO) FILMS FOR DYE SENSITIZED SOLAR CELLS

#### 4.1. Motivation of Chapter 4

After the invention of dye-sensitized solar cells (DSSC) in 1991 [1], they have attracted great interest due to their large potential applications as a cheaper alternative of conventional silicon-based p–n junction solar cells [2]. The key factors of highly efficient dye sensitized solar cell production are light harvesting, charge generation and charge transport in photo electrode components. The photo electrode is composed of two films: a photo generator dye absorbed nanoporous oxide thick film and a highly transparent conducting oxide (TCO) thin film [3]. Mostly, researches have been done about working principle, problems, and solution on photovoltaic generation on DSSCs [4-16]. Nevertheless, important parameters of light conversion efficiency, which are light transmittance, charge collection, and charge extraction to the external circuit taking place on TCO, have been barely researched. FTO (F:SnO<sub>2</sub>), indium tin oxide (ITO, tin doped indium oxide, Sn:In<sub>2</sub>O<sub>3</sub>), ATO (Sn:SbO<sub>2</sub>), and AZO (Al:ZnO) are widely used TCOs on DSSC applications [17-19]. Although ITO is rather expensive than other choices, it gives still the best performance with highest transparency and lowest resistivity. ITO is a nano composite solid-solution of In<sub>2</sub>O<sub>3</sub> and SnO<sub>2</sub> in 10:1 ratio [20-23]. ITO is an advanced ceramic material, which can be used in applications including numerous optoelectronic devices due to its excellent properties of high conductivity and high transparency [24]. In addition, it is colorless under visible light in thin film layers while in bulk form it is yellowish to grey. The high electrical conductivity originates from a conducting carrier–oxygen vacancy at the matrix

( $\text{In}_2\text{O}_3$ ) which is created by Sn dopants [23]. In terms of DSSC application performance, ITO has superior optical transmittance and lower sheet resistivity than FTO. However, ITO tends to crack under thermal annealing temperatures higher than  $300^\circ\text{C}$  [25]. Thus, ITO could be hardly used on DSSC applications while widely used on other solar cells, touch panels, PDLC, LCD and LED. To overcome the problem of weak temperature resistance of ITO, it was produced by benefiting from several commercial methods such as spray pyrolysis, pulsed laser deposition and sputtering [21, 26-31]. According to the literature survey performed by the author, it has been found that several new techniques has been developed about ITO production [24, 26] based on wet chemical methods, but neither method has been suggested in terms of fully sol-gel based DSSC. In this study, the path of production of highly transparent and low resistant ITO by sol gel method and application of ITO on DSSC were shown (Figure 4.1). Structural, optical, and electrical characteristics of the ITO films were investigated. ITO-DSSC photovoltaic characterizations were studied.

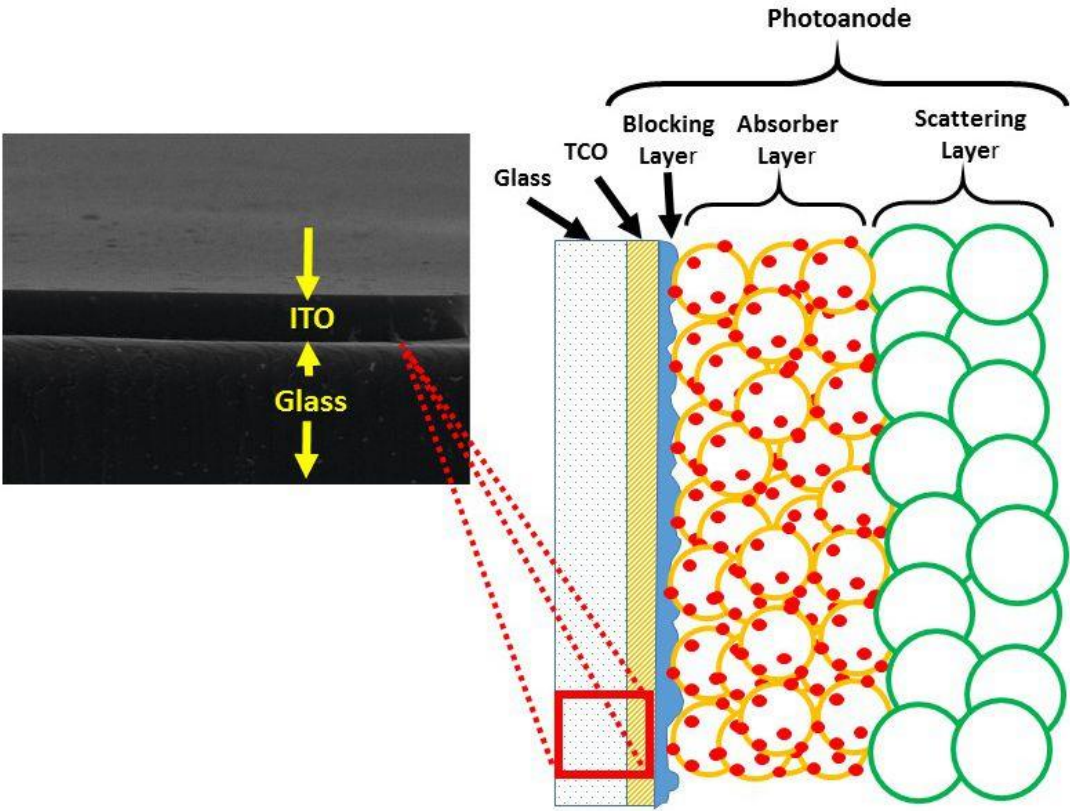


**Figure 4.1** Schematic description of chapter 4.

## 4.2. Experimental

### 4.2.1. Synthesis of ITO Gel

$\text{In}(\text{NO}_3)_3$  (Aldrich Chemical Co.) and  $\text{SnCl}_4$  (Aldrich Chemical Co.) (10:1 ratio) were mixed with a solution of ultra-pure water, acetic acid (HA) (Merck Chemical Co.) and polyethylene glycol (PG) in a 250 ml flux at 80 °C. Effect of the change in solvent concentration on the gel formation is shown in Figure 4.2. In the light of observed data, increase of water would result in increase of hydrolysis rate and hence decrease the gelation time. On the contrary, after water/PG ratio reached 10, the gelation time increased slightly. As a result,  $\text{H}_2\text{O}/\text{PG} = 10$  and  $\text{PG}/\text{HA} = 4$  concentrations were found to be the point where the reaction time is minimum, therefore these concentrations have been selected for the synthesis of ITO gel.

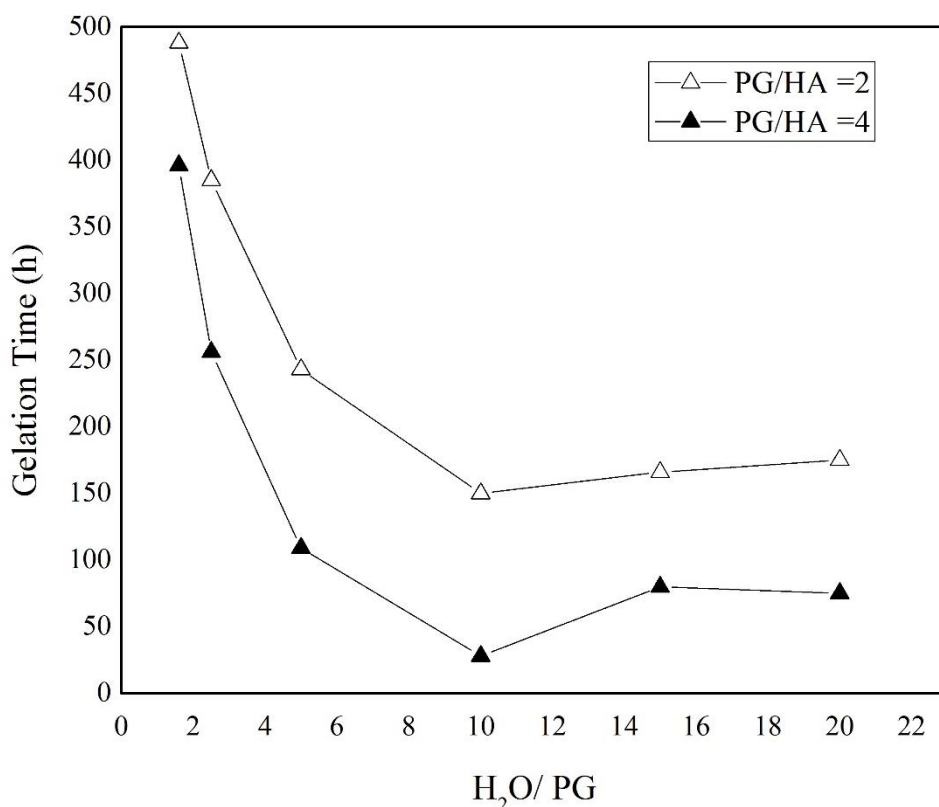


**Figure 4.2** The results for the gel formation as a function of  $\text{H}_2\text{O}/\text{PG}$  for two  $\text{HA}/\text{PG}$  weight ratios.

#### **4.2.2. Synthesis of ITO Film**

The glass substrates were sonicated in distilled water, acetone and isopropanol mixture (1:1:1 volume ratio) for 15 min. Then, they were cleaned in a detergent solution for 10 min, and then dipped into isopropanol-HCN mixture (5:1) for 35 min in an ultrasonic bath. All substrates were rinsed with distilled water and alcohol thrice, and then dried under air flow. The glass surfaces were coated by ITO gel using spin coating technique at 900 rpm for 4 s and at 2750 rpm for 30 s. Following the deposition, the ITO films were dried for 30 min at 20°C and annealed at different temperatures between 20 and 500°C for 1 h.

#### **4.2.3. Synthesis of TiO<sub>2</sub> Nanopowders**

TiO<sub>2</sub> nanopowders were synthesized by sol-gel method using tetraisopropyl orthotitanate (Aldrich Chemical Co.), isopropanol alcohol, ethylene glycol, polyethylene glycol (monolaurate) and acetic acid (HA) (Aldrich Chemical Co.). After adding a few droplets of water, hardly visible white-blue colored gel was obtained and this gel was homogenized in two steps. The first step is mechanical homogenization by SS316 blender treated with TiCl<sub>4</sub> (Daihan homogenizator). The final homogenization is carried out by applying ultrasonic homogenization with a titanium probe (Bandelin Sonoplus HD 2070) using 3 cycles for 2 min. Then, the gel was dried at 70°C in a rotary evaporator at 100 mbar. Finally, the glass-like dried gel was transferred to a crucible and annealed at 550°C for 2 h yielding nanoparticles of TiO<sub>2</sub>. The surface area of TiO<sub>2</sub> was determined as 64 m<sup>2</sup>/g by the Brunauer–Emmett–Teller (BET) method. The value of BET is higher than that of commercial P25 (BET 56 m<sup>2</sup>/g). The higher surface area means more dye to be absorbed by photoanode.

#### **4.2.4. Fabrication of the Nanocomposite ITO-TiO<sub>2</sub> Dye-sensitized Solar Cell**

ITO glasses were treated by TiCl<sub>4</sub> solution for 30 min to prevent recombination caused by contact of liquid electrolyte to ITO surface. The dye-sensitized TiO<sub>2</sub> electrodes were prepared from the TiO<sub>2</sub> paste synthesized by sol-gel method and coated on ITO film by Doctor Blade technique. Heat treatment of 10 μm thick films was conducted

at 450°C. Right after heat treatment, photoanodes were immersed in a dye (N719, Solaronix) solution of 0.5 mM in acetonitrile and kept at room temperature for 24 h. Counter electrode was prepared by dropping a solution of H<sub>2</sub>PtCl<sub>6</sub> in isopropanol and firing at 450°C. Photoanode and the transparent counter Pt electrode were assembled into a sandwich type cell. The electrolyte, which was prepared from the solution of 10:1:5 lithium iodide, iodide and 4-*tert*-butylpyridine in acetonitrile, was injected into the interspaces between the photoanode and the counter electrode and the two electrodes were brought together using Surlyn (25 μm) frames and laminated at 120°C. The active cell area was 0.25 cm<sup>2</sup>.

### 4.3. Results and Discussion

#### 4.3.1. ITO Films

In order to determine thicknesses and surface morphologies of the coated ITO films, FE-SEM analyses were performed and the results were illustrated in Figure 4.3. It is observed that smooth and crack free ITO films were successfully coated on the glass surface. On the other hand, 160 nm ITO has a few sediments.

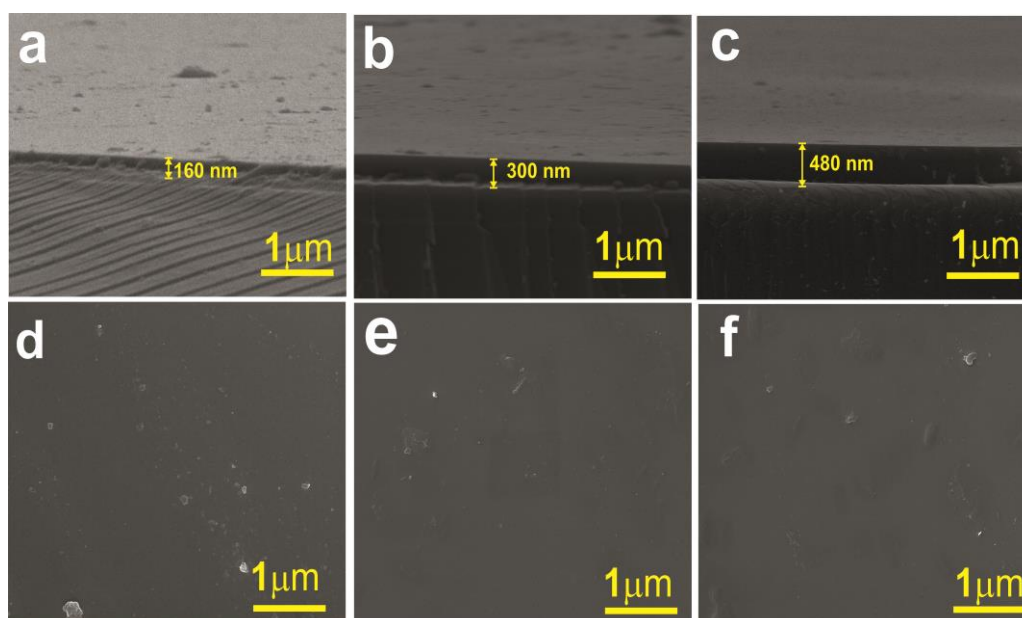


**Figure 4.3** Cross-sectional FE-SEM images of 160 nm ITO (a), 300 nm ITO (b), and 480 nm ITO (c), top view of SEM images of 160 nm ITO (d), 300 nm ITO (e), and 480 nm ITO (f).

Surprisingly, there is no agglomeration of particles and crack-free films were observed for 160 nm, 300 nm and 480 nm films. Therefore, ITO layers having different thickness can be compared easily in this study. UV-NIR transparency spectra analyses carried out for different thicknesses of ITO coated glass substrates gave the result which indicated that the transparency of 300 nm ITO coated glass substrates have showed best performance, demonstrated in Figure 4.4.a.

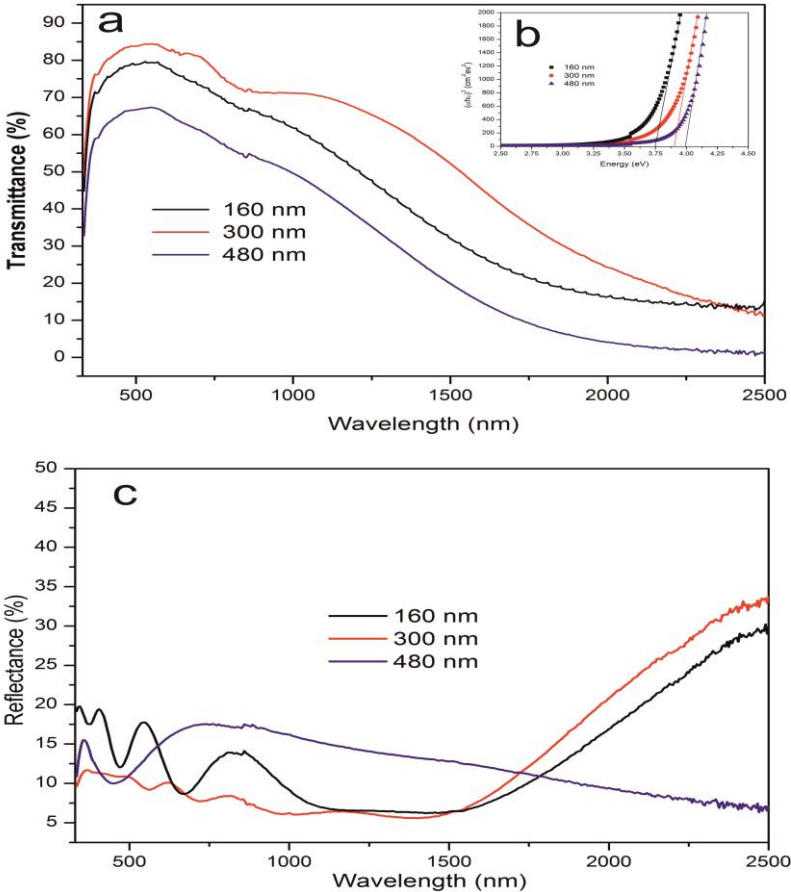


**Figure 4.4** Transmittance spectra for 160 nm ITO, 300 nm ITO, and 480 nm layers in IR - UV visible region from 300 to 2500 nm (a) and linear portion of the  $(ahv)^2$  vs photon energy  $E$ (eV) graph of 160 nm ITO, 300 nm ITO, and 480 nm (b) and reflectance spectra for 160 nm ITO, 300 nm ITO, and 480 nm layers in IR - UV visible region from 300 to 2500 nm (c).

The transparency of 300 nm ITO substrate has an average of ~80% and 85% transmission at 550 nm. On the other hand the transparency for 160 nm ITO and 480 nm ITO decreased slightly to ~80% and ~60%, respectively. As ITO has started to

absorb the light below 400 nm wavelength, the transmission of all samples went down rapidly. Transmissions approach zero when wavelength becomes closer to 330 nm.

In Figure 4.4.c, the plot of reflectivity spectra was given. The reflectivity of 300 nm ITO film at infrared region of 2500 nm in air was determined as ~33%, whereas that of 160 nm and 480 nm were found to be 28 % and 7 %, respectively. Sample coated with 300 nm ITO was reported to possess higher IR reflection properties in the infrared region, at the same time it exhibits lower reflection in the UV-visible region. However, blue shift of the absorption edges, that is, the absorption edges shifted to the short wavelength region was observed when ITO substrates became thicker. This phenomenon can be explained by the well-known Burstein-Moss (BM) shift effect,  $E_g = E_g^o + \Delta E_g^{BM}$ .  $E_g$  and  $E_g^o$  represent the band gap energy and intrinsic energy where carrier density is zero.  $\Delta E_g^{BM}$  describes the variation in the total band gap energy due to BM shift effect. The BM variation can be calculated by  $\Delta E_g^{BM} = (\hbar^2/8m_e^*) (3n_e/\pi)^{2/3}$ . Where  $\hbar$  is Planck's constant,  $m_e^*$  is the reduced effective mass of the electron carriers, and  $n_e$  is carrier concentration. It can be seen that,  $E_g^{BM}$  increases while carrier concentration  $n_e$  increases and vice versa. Due to the absorption edge shifting to high-energy region, more energy is needed for carriers to jump from valence band to the conduction band. The optical band gap of the ITO films is calculated from the absorption rate spectra using the expression,  $\alpha h\nu = A (h\nu - E_g)^{1/N}$ , where  $E_g$  can be given as the energy of the band gap, the absorption coefficient is  $\alpha$ , and frequency is  $\nu$ . The terms of  $N$  that is two for allowed direct transitions of ITO films, depends on electronic transition. The optical band gap of ITO was calculated via the plot of  $(\alpha h\nu)^2$  with energy (eV) ( $h\nu$ ), from which the linear portion is extrapolated to the point which  $\alpha h\nu$  is 0. Figure 4.4.b represents the relationship between the optical energy band gaps and ITO substrates thicknesses. The band gap increases while thicknesses increase. Optical band gaps of 160 nm ITO, 300 nm ITO and 480 nm ITO films were found as 3.75, 3.88 and 3.99 eV, respectively, at 425°C.

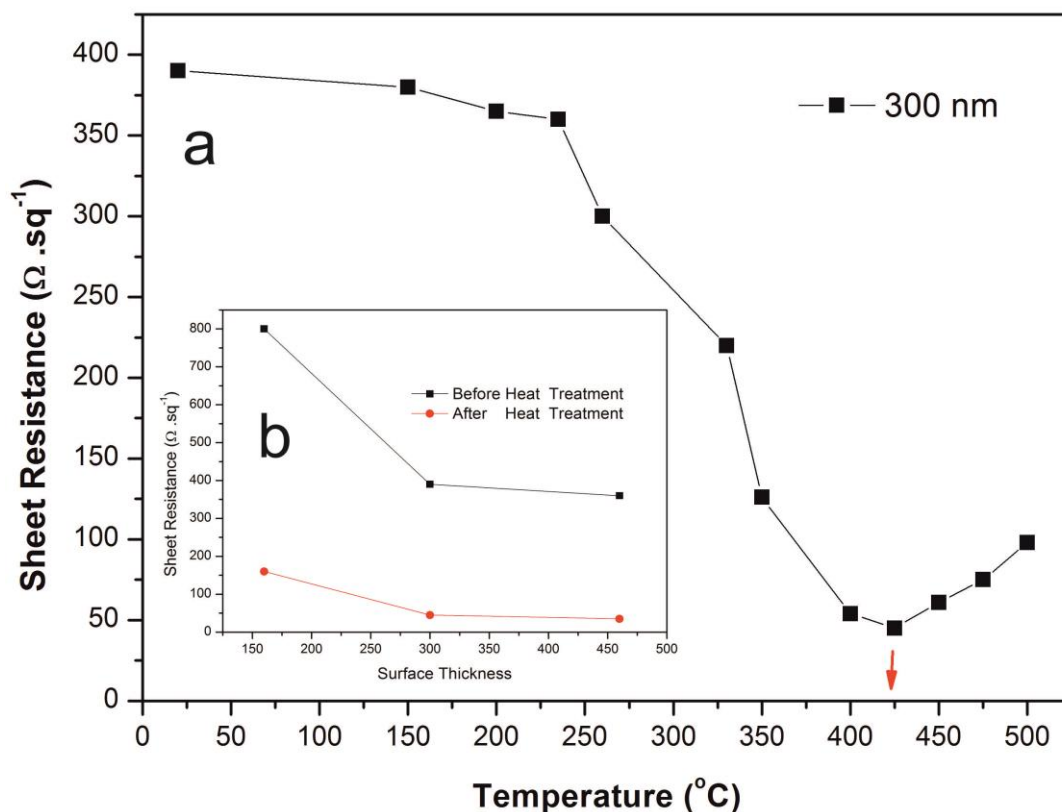


**Figure 4.5** Sheet resistance versus temperature spectra for 300 nm ITO (a), and the variation in sheet resistance, before and after heat treatment, with respect to the ITO film thickness (b).

Fig. 4.5.a shows changes in sheet resistance. 300 nm ITO film underwent a heat treatment process where each sample was heated up to different temperatures in a range of 20 $^{\circ}\text{C}$  to 500 $^{\circ}\text{C}$  with an heating rate of 10 $^{\circ}\text{C}/\text{min}$ . After the target temperature was attained, samples were kept at annealing temperature for 1 h and cooled naturally to room temperature (20 $^{\circ}\text{C}$ ). Up to 425 $^{\circ}\text{C}$ , any increase in temperature resulted in a slight decrease in resistance of ITO film, whereas after 425 $^{\circ}\text{C}$  it starts to increase rapidly. This is due to Sn atoms in the crystallite more and more diffusing homogeneously while the temperature reaches to 425 $^{\circ}\text{C}$ . The improved crystal performance and the occurrence of a decrease of the grain boundary reduce the absorption of donor SnO<sub>2</sub> in dislocations and crystal defects. To be more precise, the carrier concentration and the mobility increase, reducing the resistivity of the films. On the other hand, at temperatures higher than 425 $^{\circ}\text{C}$ , annealed ITO thin films have higher sheet resistance, for example 300 nm ITO thin films annealed at 500 $^{\circ}\text{C}$  has 98

$\Omega/\text{sq}$ , while 300 nm ITO thin films annealed at  $425^\circ\text{C}$  has  $45 \Omega/\text{sq}$ . The result obtained can be due to the aggregation of the  $\text{In}_2\text{O}_3$  particles or grain growth in the matrix at  $425^\circ\text{C}$ . According to the literature, at low annealing temperatures the Sn concentrations distribution is unhomogeneous and also tin oxide in the matrix is in the SnO state rather than  $\text{SnO}_2$  state, therefore the sheet resistance becomes higher. On the opposite, at higher temperatures, the defects of oxygen are filled by the oxygen atoms in the ITO films, which reduce the sheet resistance. Figure 4.5.b. shows the variation in sheet resistance, before and after heat treatment, with respect to the ITO thickness. Before heat treatment, the sheet resistance of the ITO film with 160 nm thickness is approximately  $800 \Omega/\text{sq}$ . As the film, thickness goes up to values about 480 nm, the sheet resistance reduces by almost 50 % (around  $360 \Omega/\text{sq}$ ). 300 nm ITO thin films have a sheet resistance of  $390 \Omega/\text{sq}$ . Following heat treatment, the sheet resistance goes down. The sheet resistance of 160 nm ITO film was reduced by almost 80 %,  $158 \Omega/\text{sq}$  in number. Stunningly, sheet resistance of 300 nm ITO film has been enhanced mostly after heat treatment, the reduction in sheet resistance of ITO reached 88 %.

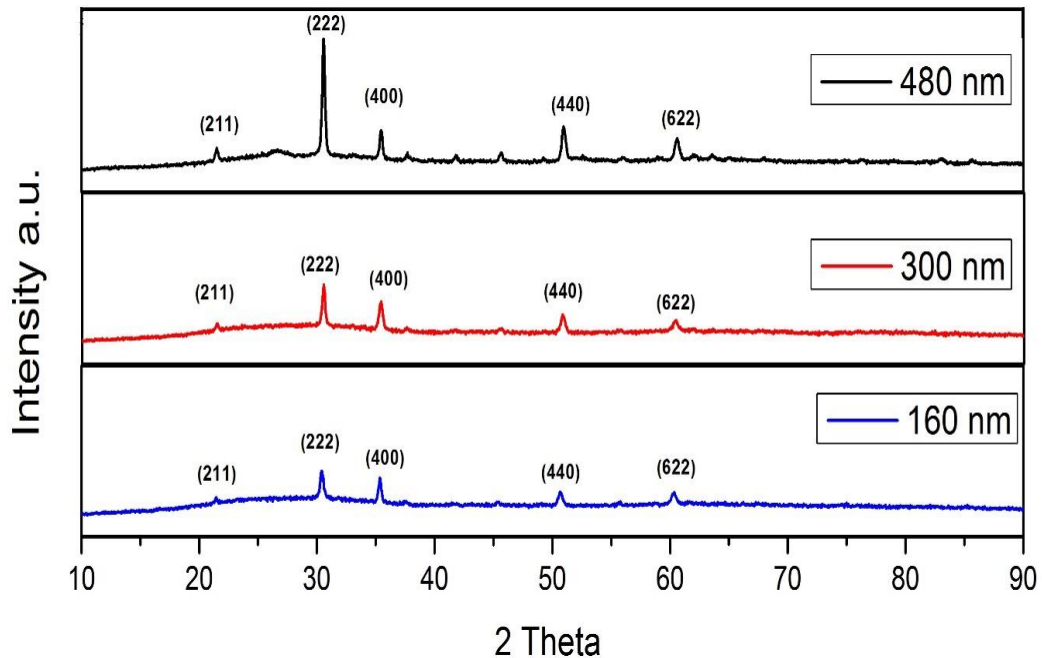


**Figure 4.6** XRD spectra for 160 nm ITO, 300 nm ITO, and 480 nm ITO films.

Figure 4.6 illustrates the XRD patterns of 160 nm, 300 nm and 480 nm ITO films grown on glass substrates. The peak in the XRD pattern reveals an oriented growth of ITO. On the XRD patterns of ITO films, sharp peaks of ITO have been detected at (211), (222), (400), (440) and (622) orientations. According to literature, the pure  $\text{In}_2\text{O}_3$  phase has a preferred orientation in the [100] direction. Such a sharp (222) peak in the 480 nm ITO XRD pattern indicates a (111) preferred orientation of the ITO film, which was reported in the previous studies in which sputtering method, evaporation method and sol-gel methods were used. Therefore, (111) preferred orientation implies that the tin source replaces indium substitutionally in the bcc lattice. This observation indicates the enhancement in crystallinity of ITO film obtained by sol-gel method.

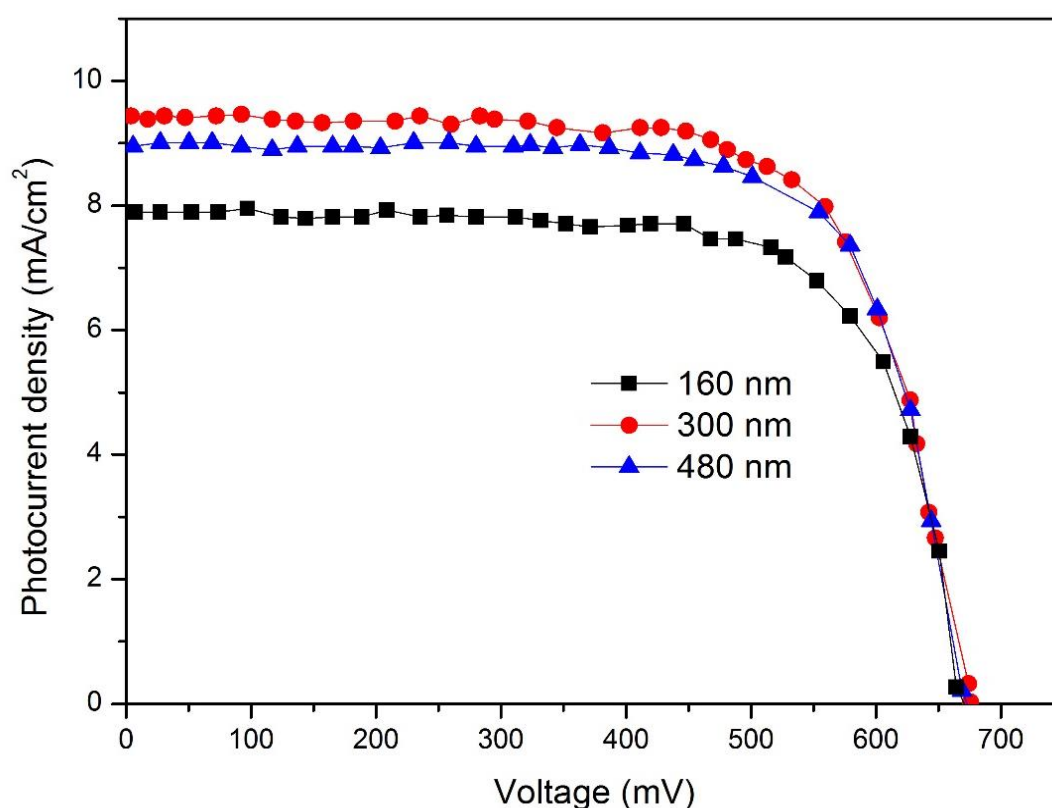


**Figure 4.7** J-V curves of DSSCs based on 160 nm ITO, 300 nm ITO and 480 nm ITO substrates under illumination AM 1.5, 100 mW/cm<sup>2</sup>.

**Table 4.1** Efficiency analysis of DSSCs based on 160 nm ITO, 300 nm ITO and 480 nm ITO substrates.

<b>Sample</b>	<b>Jsc</b> <b>(mA/cm<sup>2</sup>)</b>	<b>Voc</b> <b>(mV)</b>	<b>FF</b> <b>(%)</b>	<b>η</b> <b>(%)</b>
160 nm	7.89	677	0.71	3.80
300 nm	9.43	675	0.68	4.32
480 nm	8.46	680	0.72	4.15

The experimental results of DSSCs based on 160 nm ITO, 300 nm ITO and 480 nm ITO substrates at AM 1.5 irradiation of 1 Sun are shown in Figure 4.7. The photoelectric conversion parameters of DSSCs based on different substrates are summarized in Table 4.1. The Jsc, Voc and fill factor (FF) of the DSSC based on 300 nm ITO substrate are 9.43 mA/cm<sup>2</sup>, 675 mV and 0.68, respectively, corresponding to an energy conversion efficiency of 4.32 %. Comparing to photoelectric conversion efficiency at 3.80 % with ITO film thickness of 160 nm, the conversion efficiency obviously rises when thin film thickness is 300 nm. The photoelectric conversion efficiency of DSSC with film thickness 480 nm is reduced to 4.15 % and the photocurrent density was 8.46 mA/cm<sup>2</sup>. As seen in the J-V results, there is an extremely great relationship between transparent conductive thin film thickness and photoelectric conversion efficiency. 300 nm ITO sample shows best performance on photovoltaic efficiency. This improvement can be clarified as 300 nm ITO thickness having enough transparency and conductivity to reduce charge loss at the ITO/TiO<sub>2</sub> interface, and the improvement of the adherence between the ITO and the TiO<sub>2</sub> layer, by which the interfacial charge resistance is reduced. Therefore these combined effects are responsible for the significant increase of J<sub>SC</sub> and η on the ITO sol-gel based DSSC.

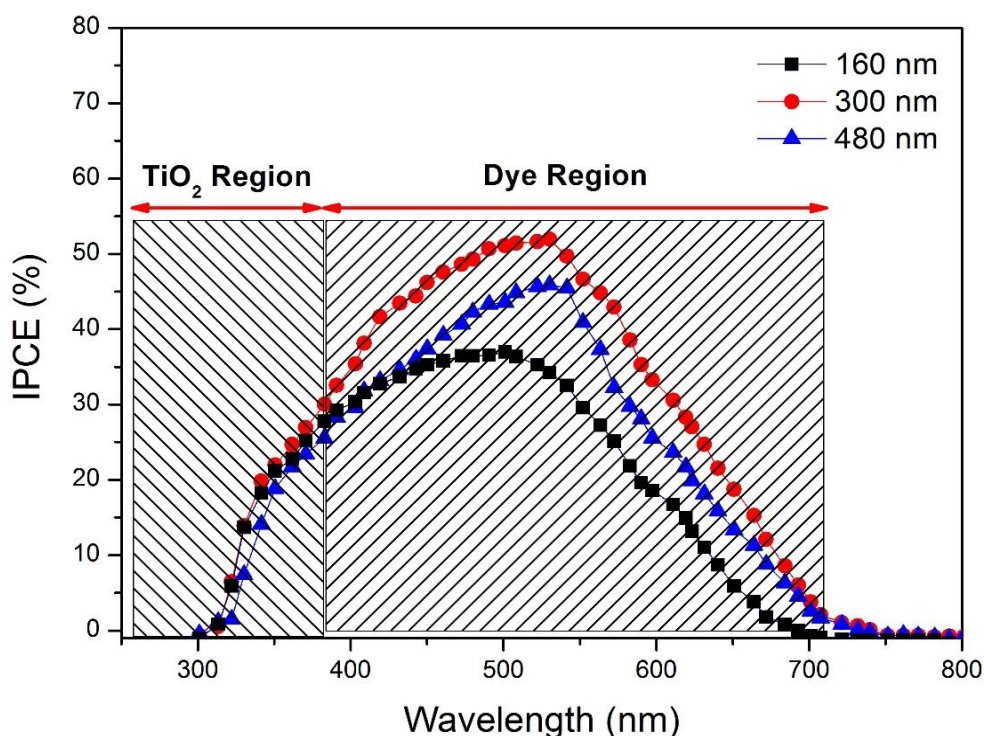


**Figure 4.8** IPCE spectra for the DSSCs based on 160 nm ITO, 300 nm ITO and 480 nm ITO substrates.

Incident Photon-to-Current Conversion Efficiency (IPCE) is known as the ratio of the spectral sensitivity of the generated photocurrent versus the light intensity at the given wavelength of incident light based on a single photon. The IPCE is an important factor in clarifying DSSC performance. In order to investigate the light harvesting effect of ITO films with different thicknesses produced by sol-gel method, IPCE measurements on various ITO-based DSSCs were performed and the results are given in Figure 4.8. The IPCE diagram can be inspected in two parts. First part is left region, which is below 390 nm wavelength. This part corresponds to absorption of photon by the band-gap of the TiO<sub>2</sub> nanoparticles. The first region is less significant because nearly 3 % of the sunlight can be utilized. There is almost no difference in IPCE efficiency for all samples in the first region. The second region, which is above 390 nm, belongs to dye sensitization effect. 300 nm ITO based DSSC has the best performance on IPCE efficiency due to lower sheet resistance and highest transparency. 160 nm ITO based DSSC however showed poor performance above 390 nm wavelength, because it has the highest surface resistivity and the photoelectrons produced by dye sensitization, accumulate on TiO<sub>2</sub> particles rather than transferring to ITO region. This situation causes recombination of photoelectrons. Although 480 nm ITO based DSSC has

lowest surface resistance, it has also lowest transparency. Therefore, it did not show good performance as 300 nm ITO based cell. All samples show poor performance in wavelengths longer than 700 nm and as a consequence, somewhat similar photocurrent density is observed.

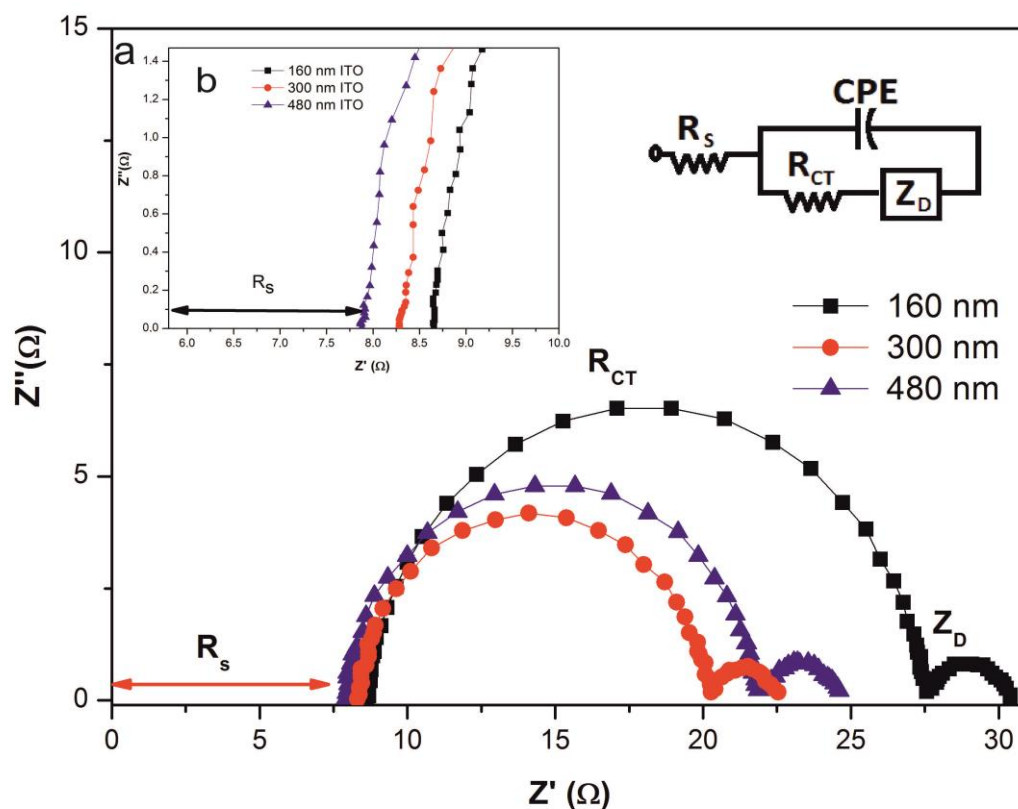


**Figure 4.9** Comparison of the resultant Nyquist plots of the symmetrical cells produced using different ITO thicknesses (a) and magnified version of the region between  $R_s$  and  $R_{CT}$  boundary (b).

The electrochemical impedance spectroscopy (EIS) has been used as an investigation tool for the electron transport resistance and recombination in DSSCs. EIS was performed using symmetric cells which were fabricated by the sol-gel produced anode and counter electrodes; because it is reasonable to assume that the resistance at the  $TiO_2$ /electrolyte interface is essentially independent of the counter electrode. Figure 4.9.a shows comparison of the resultant Nyquist plots of the symmetrical cells with different ITO thicknesses and Figure 4.9.b is magnified version of the region between  $R_s$  and  $R_{CT}$  boundary. Two semicircles were observed in the measured frequency range of  $10^{-1}$  to  $10^5$  Hz for all electrodes. The equivalent circuit of DSSC used for fitting impedance data was calculated according to literature and it can be seen inside the

graph. The resistance element  $R_s$  in the high-frequency region is related to the sheet resistance of the ITO layer. Other impedance elements can be described with the charge transport at the  $TiO_2$ /dye/electrolyte interface ( $R_{CT}$ ), and the Nernstian diffusion in the electrolyte ( $Z_D$ ). It is apparent that the  $R_{CT}$  values were changed conspicuously, but the  $Z_D$  values remained nearly constant. This means that deposition method of Pt in the preparation of the counter electrode did not influence ionic diffusion within the electrolyte. Therefore, sol-gel based ITO can be used as counter electrode successfully for all thicknesses. According to Table 4.2,  $R_s$  results mimic somehow sheet resistance results. 300 nm ITO thickness shows best performance on  $R_s$  resistance. This positive effect has been also seen on  $R_{CT}$  results. The 300 nm ITO thin film has the lowest charge transfer resistance.

**Table 4.2** Kinetic parameters of DSSCs with and without blocking layers.

Sample	$R_s$	$R_{CT}$	$Z_D$
160 nm	8.69	18.94	2.74
300 nm	8.13	12.17	2.60
480 nm	7.88	14.14	2.65

In summary, ITO samples have shown different performances in terms on electrical properties. The surface resistance decrease after heat treatment is an important recombination concern for ITO usage on DSSC. The surface resistance decreases with increasing ITO thickness and increases after 425°C. 300 nm ITO layer shows best performance and it has surface resistance of 45  $\Omega$  /sq at 425°C. This temperature is enough to create suitable mesoporous anatase  $TiO_2$  matrix for DSSC. According to UV-Vis measurements of samples, the transparency of ITO coated glass is sufficiently enough to be applied in DSSC. Moreover, 300 nm ITO sample has highest transparency. Optical band gap of 300 nm ITO sample shifted to higher energy state. In other words, Fermi level of 300 nm ITO shifted toward the higher energy side,

therefore 300 nm ITO has same surface resistance as 480 nm ITO. 300 nm ITO enhanced the photovoltaic energy conversion efficiency by as much as 13.68 %, compared to 160 nm ITO-based DSSC. 160 nm ITO based DSSC has lowest performance in this study. IPCE spectra directly illustrate the performance of external circuit produced by an incident photon. IPCE results can reflect transmittance behavior of samples to some extent. Higher photon spectral response was observed for 300 nm ITO based cell on photovoltaic circuit due to the highest transparency observed for that sample. The positive results were also confirmed by the EIS study. 300 nm ITO reduced interfacial resistance effects which increase the recombination time. 300 nm and 480 nm ITO have lower charge transport resistance  $R_{CT}$  than 160 nm ITO. The higher recombination time affects the photovoltaic properties positively. Although there are some studies on transparent conductive oxide in DSSC, only some of them have data on the conversion efficiency of produced cells. B. Yoo et.al have produced ITO/ATO/TiO<sub>2</sub> by magnetron sputtering method and measured the overall conversion efficiency about 4.57%. T. Kawashima et.al have fabricated FTO/ITO double layered TCO for using DSSC, and they obtained 3.7% conversion efficiency and 80 % transparency. Pawa et.al have fabricated DSSC using boron doped- ZnO conductive layer using sol-gel method and obtained 1.53%. The conversion efficiency found by Chen et.al was 6.7% for commercial ITO (Gem Technology Optoelectronics, Taiwan). The conversion efficiency of 4.32% obtained in this study by sol-gel processing method were better than the similar DSSCs formed using sol-gel based TCO or commercial ITO in the literature. Therefore, it can be concluded that 300 nm ITO coated glass which is produced by sol-gel technique is a promising a candidate of TCO substrates for DSSC applications.

#### **4.4. Conclusion**

In this study, in order to overcome the problems associated with rarely researched important parameters of light conversion efficiency which are light transmittance, charge collection, and charge extraction to the external circuit taking place on ITO. An alternative path of production of highly transparent and low resistance ITO layers by sol gel method and their application on DSSCs are shown. Temperature resistant, highly transparent ITO films having a well oriented structure, better optical and

electrical characteristics were investigated. Optimizing the thickness of ITO for DSSC applications has been investigated. Highly efficient fully solution based dye sensitized solar cells have been produced. The best conversion efficiency was obtained as 4.32 %.

## REFERENCES

1. Oregan, B. and M. Gratzel, *A Low-Cost, High-Efficiency Solar-Cell Based on Dye-Sensitized Colloidal TiO<sub>2</sub> Films*. *Nature*, 1991. **353**(6346): p. 737-740.
2. Nazeeruddin, M.K., et al., *Raman Characterization of Charge-Transfer Transitions in Ligand-Bridged Binuclear Polypyridyl Complexes of Ruthenium(II)*. *Journal of the Chemical Society-Dalton Transactions*, (2): p. 323-325. 1993.
3. Zakeeruddin, S.M., et al., *Design, synthesis, and application of amphiphilic ruthenium polypyridyl photosensitizers in solar cells based on nanocrystalline TiO<sub>2</sub> films*. *Langmuir*, **18**(3): p. 952-954. 2002.
4. Nazeeruddin, M.K., S.M. Zakeeruddin, and K. Kalyanasundaram, *Enhanced Intensities of the Ligand-to-Metal Charge-Transfer Transitions in Ru(III) and Os(III) Complexes of Substituted Bipyridines*. *Journal of Physical Chemistry*, **97**(38): p. 9607-9612. 1993.
5. Nazeeruddin, M.K., et al., *Engineering of efficient panchromatic sensitizers for nanocrystalline TiO<sub>2</sub>-based solar cells*. *Journal of the American Chemical Society*, **123**(8): p. 1613-1624. 2001.
6. Nusbaumer, H., et al., *Co-II(dbbiP)(2)(2+) complex rivals tri-iodide/iodide redox mediator in dye-sensitized photovoltaic cells*. *Journal of Physical Chemistry B*, **105**(43): p. 10461-10464. 2001.
7. Wang, P., et al., *A stable quasi-solid-state dye-sensitized solar cell with an amphiphilic ruthenium sensitizer and polymer gel electrolyte*. *Nature Materials*, **2**(6): p. 402-407. 2003.
8. Fantacci, S., et al., *Photophysical properties of [Ru(phen)(2)(dppz)](2+) intercalated into DNA: An integrated Car-Parrinello and TDDFT study*. *Journal of the American Chemical Society*, **127**(41): p. 14144-14145. 2005.
9. Kietzke, T., et al., *Effect of annealing on the characteristics of organic solar cells: Polymer blends with a 2-vinyl-4,5-dicyanoimidazole derivative*. *Macromolecules*, **40**(13): p. 4424-4428. 2007.

10. Ito, S., et al., *Fabrication of thin film dye sensitized solar cells with solar to electric power conversion efficiency over 10%*. Thin Solid Films, **516**(14): p. 4613-4619. 2008.
11. Kitiyanan, A., et al., *The preparation and characterization of nanostructured TiO<sub>2</sub>-ZrO<sub>2</sub> mixed oxide electrode for efficient dye-sensitized solar cells*. Journal of Solid State Chemistry, **178**(4): p. 1044-1048. 2005.
12. Burke, A., et al., *The function of a TiO<sub>2</sub> compact layer in dye-sensitized solar cells incorporating "Planar" organic dyes*. Nano Letters, **8**(4): p. 977-981. 2008.
13. Lee, J.H., N.G. Park, and Y.J. Shin, *Nano-grain SnO<sub>2</sub> electrodes for high conversion efficiency SnO<sub>2</sub>-DSSC*. Solar Energy Materials and Solar Cells, **95**(1): p. 179-183. 2011.
14. Ueno, S. and S. Fujihara, *Effect of an Nb<sub>2</sub>O<sub>5</sub> nanolayer coating on ZnO electrodes in dye-sensitized solar*. Electrochimica Acta, **56**(7): p. 2906-2913. 2011.
15. Chen, H.W., et al., *Electrophoretic deposition of ZnO film and its compression for a plastic based flexible dye-sensitized solar cell*. Journal of Power Sources, **196**(10): p. 4859-4864. 2011.
16. Cosar, B., et al., *Photovoltaic performance of bifacial dye sensitized solar cell using chemically healed binary ionic liquid electrolyte solidified with SiO<sub>2</sub> nanoparticles*. Electrochimica Acta, **87**: p. 425-431. 2013.
17. van de Lagemaat, J., N.G. Park, and A.J. Frank, *Influence of electrical potential distribution, charge transport, and recombination on the photopotential and photocurrent conversion efficiency of dye-sensitized nanocrystalline TiO<sub>2</sub> solar cells: A study by electrical impedance and optical modulation techniques*. Journal of Physical Chemistry B, **104**(9): p. 2044-2052. 2000.
18. Shah, A.V., et al., *Thin-film silicon solar cell technology*. Progress in Photovoltaics, **12**(2-3): p. 113-142. 2004.
19. Fortunato, E., et al., *Transparent conducting oxides for photovoltaics*. Mrs Bulletin, **32**(3): p. 242-247. 2007.
20. Bisht, H., et al., *Comparison of spray pyrolyzed FTO, ATO and ITO coatings for flat and bent glass substrates*. Thin Solid Films, **351**(1-2): p. 109-114. 1999.

21. Quaas, M., et al., *Influence of microstructure on oxygen diffusion in plasma-deposited In/Sn films*. Thin Solid Films, **420**: p. 306-311. 2002.
22. Warschkow, O., et al., *Defect structures of tin-doped indium oxide*. Journal of the American Ceramic Society, **86**(10): p. 1700-1706. 2003.
23. Warschkow, O., et al., *Defect cluster aggregation and nonreducibility in tin-doped indium oxide*. Journal of the American Ceramic Society, **86**(10): p. 1707-1711. 2003.
24. Tomonaga, H. and T. Morimoto, *Indium-tin oxide coatings via chemical solution deposition*. Thin Solid Films, **392**(2): p. 243-248. 2001.
25. Kundu, S. and P.K. Biswas, *Synthesis of nanostructured sol-gel ITO films at different temperatures and study of their absorption and photoluminescence properties*. Optical Materials, **31**(2): p. 429-433. 2008.
26. Alam, M.J. and D.C. Cameron, *Investigation of annealing effects on sol-gel deposited indium tin oxide thin films in different atmospheres*. Thin Solid Films, **420**: p. 76-82. 2002.
27. Xue, X.Y., et al., *Synthesis and ethanol sensing properties of indium-doped tin oxide nanowires*. Applied Physics Letters, **88**(20). 2006.
28. Savu, R. and E. Joanni, *Influence of ambient gas on the growth and properties of porous tin-doped indium oxide thin films made by pulsed laser deposition*. Thin Solid Films, **515**(20-21): p. 7813-7819. 2007.
29. Venkatachalam, S., et al., *Characterization of nanocrystalline indium tin oxide thin films prepared by ion beam sputter deposition method*. Thin Solid Films, **518**(23): p. 6891-6896. 2010.
30. Pan, H., et al., *Fiber laser annealing of indium-tin-oxide nanoparticles for large area transparent conductive layers and optical film characterization*. Applied Physics a-Materials Science & Processing, **104**(1): p. 29-38. 2011.
31. Kim, D.H., Park, K.S., *Synthesis of TiO<sub>2</sub>/ITO Nanostructure Photoelectrodes and Their Application for Dye-sensitized Solar Cells*. Journal of the Korean Ceramic Society, **48**(1): p. 4. 2011.



## CHAPTER 5

### **PRODUCTION OF HIGHLY EFFICIENT FULLY SOL-GEL BASED 1D ITO NANO STRUCTURE - TiO<sub>2</sub> NANO POWDER COMPOSITE PHOTOANODE FOR DYE SENSITIZED SOLAR CELL**

#### **5.1. Motivation of Chapter 5**

After the discovery of dye-sensitized solar cells (DSSC) in 1991 [1], DSSC became a cheap alternative to conventional silicon-based p–n junction solar cells [2, 3]. The basic components of highly efficient dye sensitized solar cell are an electrolyte system and dye absorbed photo-generator nanoporous oxide thick film covered by two highly transparent conducting oxide (TCO) thin film [4-6]. According to the previous studies conducted regarding new type sensitizer, production of new type photoanode material and recycling electrolyte, the conversion efficiency of photovoltaic generation on DSSCs has been improved [7]. Nevertheless, important parameters of light conversion efficiency resulting from the interactions between photoanode mesoporous material and TCO have been rarely studied. Widely used transparent conductor such as FTO (F:SnO<sub>2</sub>), ITO (Sn:In<sub>2</sub>O<sub>3</sub>), ATO (Sn:SbO<sub>2</sub>), and AZO (Al:ZnO) and commercial TCOs have been used in DSSC applications [8]. Indium tin oxide (ITO, tin-doped indium oxide) is a nanocomposite solid-solution of In<sub>2</sub>O<sub>3</sub> and SnO<sub>2</sub> in 10:1 ratio [9]. ITO which is an advanced ceramic material can be applied to numerous optoelectronic devices due to its excellent properties including high conductivity and high transparency that is colorless in visible light region [10, 11]. The high electrical conductivity is originated from Sn dopants which create a conducting carrier–oxygen vacancy at the matrix (In<sub>2</sub>O<sub>3</sub>) [12, 13]. Although ITO is expensive than other choices, it still gives best performance on high transparency and low resistivity [14]. There are two problems stemming from ITO usage on DSSC applications. One of them is the

production cost of ITO that could be solved by sol-gel processing method [15, 16], which is one of the basic techniques that gives cheapest solution. The second one is the maximization of interaction in the interface area between ITO and the photoanodic TiO<sub>2</sub> layer to reduce electron recombination. According to literature the energy conversion efficiency of DSSCs depends on the electron transport in the photoelectrode. Therefore, one-dimensional (1D) structures such as rods or wires of semiconductor materials can greatly improve DSSCs conversion efficiency by offering direct electrical pathways for photo-generated electrons. To produce highly efficient interfacial area between ITO-TiO<sub>2</sub>, cross like 1-D nanostructure of ITO is thought to be used. Up till today, there is not any clue about the advantage of using 1D nanostructure of ITO nanowires on DSSC reported in literature [9, 17-22]. E. Joanni et.al have produced ITO nanowires by laser ablation and measured the overall conversion efficiency about 0.15%. The conversion efficiency found by D. H. Kim et.al using metal evaporation method was 1.4% for ITO nanowires due to the reduction of grain boundaries, efficient high charge collection, and rapid electron transport. In this study, indium tin oxide (ITO) nanoparticles, nanowires and thin films have been produced on glass substrates by sol-gel technique and these were used for the production of nano-crystalline dye-sensitized solar cells (nc-DSSC) to improve the photovoltaic performance that are given in Figure 5.1. ITO film produced by sol-gel method showed enhanced photovoltaic and charge transport properties. ITO nanowire modification helps to increase the interaction in the interface area between the transparent conductive indium tin oxide (ITO)-coated glass electrode and the photoanodic TiO<sub>2</sub> layer.

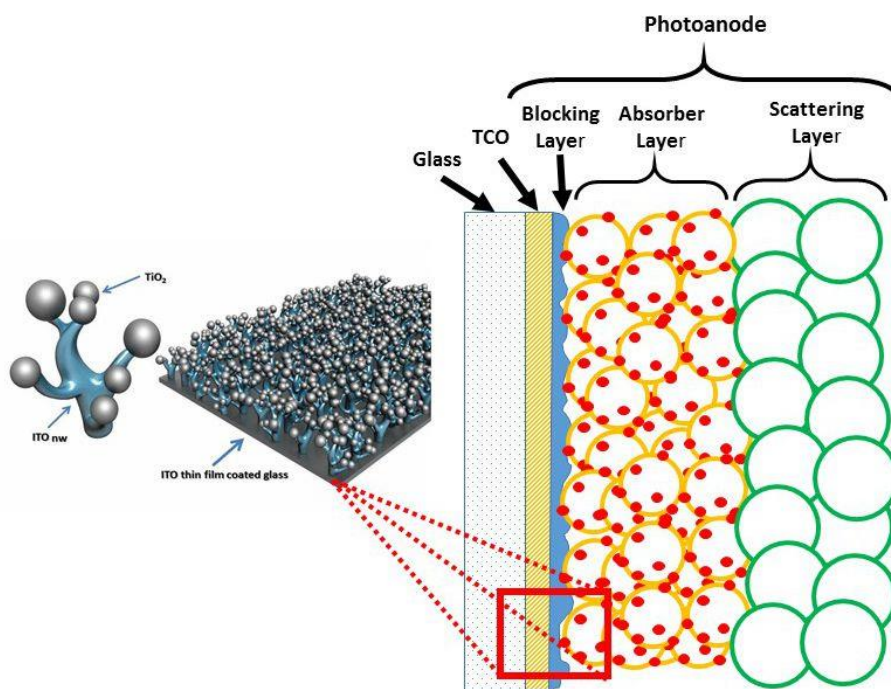


**Figure 5.1** Schematic description of chapter 5.

## 5.2. Experimental

### 5.2.1. Synthesis of ITO gel

$\text{In}(\text{NO}_3)_3$  (Aldrich Chemical Co.) and  $\text{SnCl}_4$  (Aldrich Chemical Co.) were mixed with a solution of ultra-pure water, acetic acid (HA) (Merck Chemical Co.) and polyethylene glycol (PG) in a 250 ml flux at 80 °C. The water addition affects the reaction rate adversely. Since  $\text{H}_2\text{O}/\text{PG} = 10$  and  $\text{PG}/\text{HA} = 4$  concentrations give best performance for reaction time, they have been selected for the synthesis of ITO gel.

### 5.2.2. Synthesis of ITO film

The glass substrates were sonicated in distilled water, acetone and isopropanol mixture (1:1:1 volume ratio) for 15 min. Then, they were cleaned in a detergent solution for 10 min before dipping in isopropanol-HCN mixture (5:1) for 35 min in an ultrasonic

homogenizer. All substrates were rinsed with distilled water and alcohol three times, and then dried under air flow. The glass surfaces were coated by ITO gel using spin coating technique at 900 rpm for 4 s and 2750 rpm for 30 s. Following deposition, the ITO films were dried for 20- 30 min at 20°C and annealed at 400°C for 2 h.

### 5.2.3. Synthesis of ITO nanopowders

In order to obtain better and faster ITO nanowire, nucleation step is needed. The nucleation step depends on agglomerated nanoparticles (seed). To produce the suitable seed particles, the gels were dried at 40°C for 2 h and 60°C for 2 h and then annealed at 400°C for 2 h. Then, ITO nanopowders (ITO pw) were obtained.

### 5.2.4. Synthesis of ITO nanowires

ITO nanowires (ITO nw) were obtained by seeding ITO nanopowders on ITO thin films and keeping them in a solution of 1 mM 10:1  $\text{In}(\text{NO}_3)_3$  (Aldrich Chemical Co.) and  $\text{SnCl}_4$  (Aldrich Chemical Co.) for 24 h in two steps as seen in Figure 5.2.a and b.

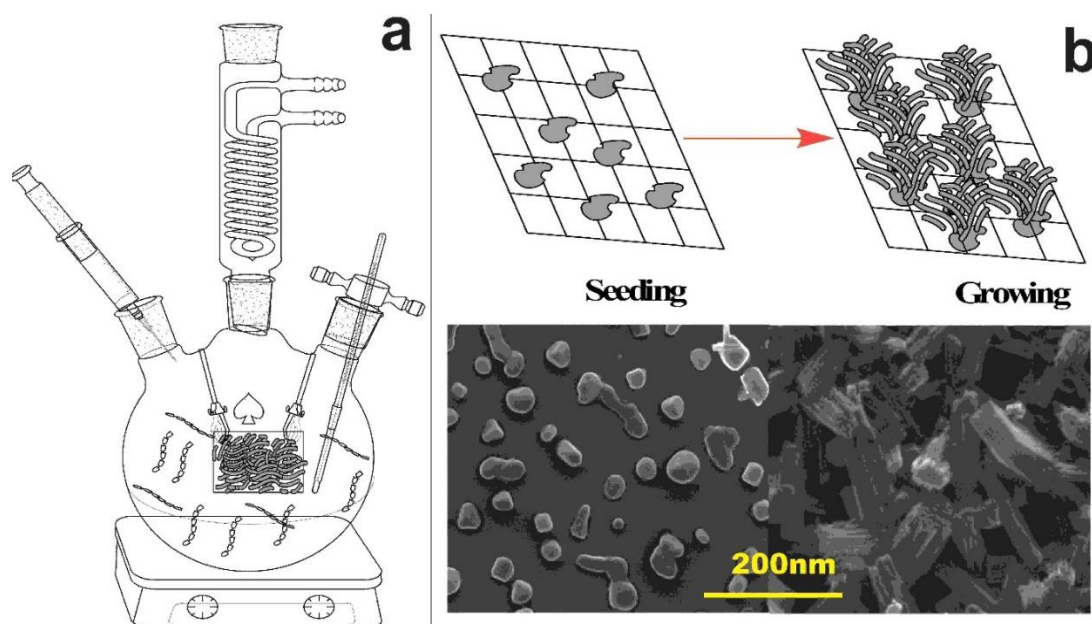


**Figure 5.2** Schematic reaction vessel for the production of ITO nanowires (a). Schematic of nanowire growth steps (b).

#### **5.2.4. a. ITO seeding step**

150 mg ITO nanopowders and 8 ml ethanol were mixed, crushed and grinded using an agate mortar. After grinding, mixture was transferred to a polytetrafluoroethylene (PTFE) beaker before adding some ethanol to add up the volume to 50 ml. Then, 0.5 ml HNO<sub>3</sub> was added to the solution in order to prevent agglomeration of these particles. Finally, the solution was mixed with a magnetic strip and sonicated with an ultrasonic horn. This ITO seeding solution was applied to ITO coated glass substrates by using spin coater twice at 2000 rpm and final annealing was done at 400°C for 30 min. Seeding step is crucial for nucleation of ITO nanowire. ITO seeded substrates can be seen in SEM micrograph presented in Figure 5.2.b.

#### **5.2.4. b. Growth Step of ITO Nanowires by Hydrothermal Method**

The annealed ITO seeded substrates were placed in a reaction vessel perpendicular to its bottom (Figure 5.2.a). Then, 1 mM 10:1 In(NO<sub>3</sub>)<sub>3</sub> and SnCl<sub>4</sub> solution were added until the substrate was completely covered. The nanowires were obtained by hydrothermal treatment at 85°C for 24 h in the solution. The Figure 5.3.a represents cross like ITO nanowires obtained by hydrothermal treatment at 85°C for 24 h. According to literature, such nanowires are often referred as one dimensional (1-D) materials. 1D material has more chance to interact with the TiO<sub>2</sub> photoanode layer than thick ITO film (bulk material). Therefore the interface area between the transparent conductive indium tin oxide (ITO) coated glass electrode and the photoanodic TiO<sub>2</sub> layer is maximized.

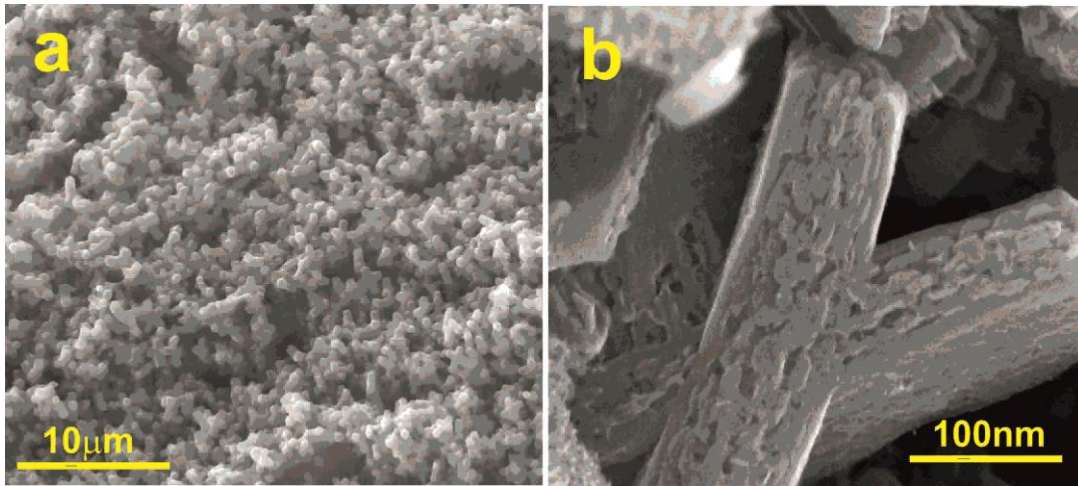


**Figure 5.3** a) SEM micrograph of ITO nanowires obtained by hydrothermal treatment at 85°C for 24 h. b) a magnified view of same nanowires.

### 5.2.5. Synthesis of TiO<sub>2</sub> Nanopowders

TiO<sub>2</sub> nanopowders were synthesized by sol-gel method using tetraisopropyl orthotitanate (Aldrich Chemical Co.), isopropanol alcohol, ethylene glycol, polyethylene glycol (monolaurate) and acetic acid (HA) (Aldrich Chemical Co.). After adding a few droplets of water, a bluish white colored gel was obtained and this gel was homogenized in two steps. The first step is the mechanical homogenization by TiCl<sub>4</sub> treated SS316 blender (Daihan homogenizator). The final homogenization is the ultrasonic homogenization by a titanium probe (Bandelin Sonoplus HD 2070) using 3 cycles at 75% power for 2 min. Then, the gel was dried at 70°C in a rotary evaporator at 100 mbar. Finally, the glass-like dried gel was transferred to a crucible and annealed at 550°C for 2 h, yielding nanoparticles of TiO<sub>2</sub>. The surface area of TiO<sub>2</sub> was determined as 64 m<sup>2</sup>/g by Brunauer–Emmett–Teller (BET) method. The value of BET is higher than that of commercial P25 (BET 56 m<sup>2</sup>/g). The higher surface area helps photoanodes to absorb more dye.

### 5.2.6. Fabrication of the Nanocomposite ITO-TiO<sub>2</sub> Dye Sensitized Solar Cell

ITO NW and bare ITO samples were treated by TiCl<sub>4</sub> solution for 30 min for protection from recombination that could result in touching of liquid electrolyte to the ITO

surface. The dye-sensitized TiO<sub>2</sub> electrodes were prepared from the TiO<sub>2</sub> paste synthesized by sol-gel method and coated on ITO film (Bare ITO) or on ITO nanowires (ITO NW) by Doctor Blade technique. The transparent counter Pt electrode was assembled into a sandwich type cell. The electrolyte, prepared from the solution of 10:1:5 lithium iodide, iodide and 4-*tert*-butylpyridine in acetonitrile, was injected into the interspaces between the photoanode and the counter electrode and the two electrodes were brought together using Surlyn (25 μm) frames and laminated at 120°C. The active cell area was 0.25 cm<sup>2</sup>.

### 5.3. Results And Discussion

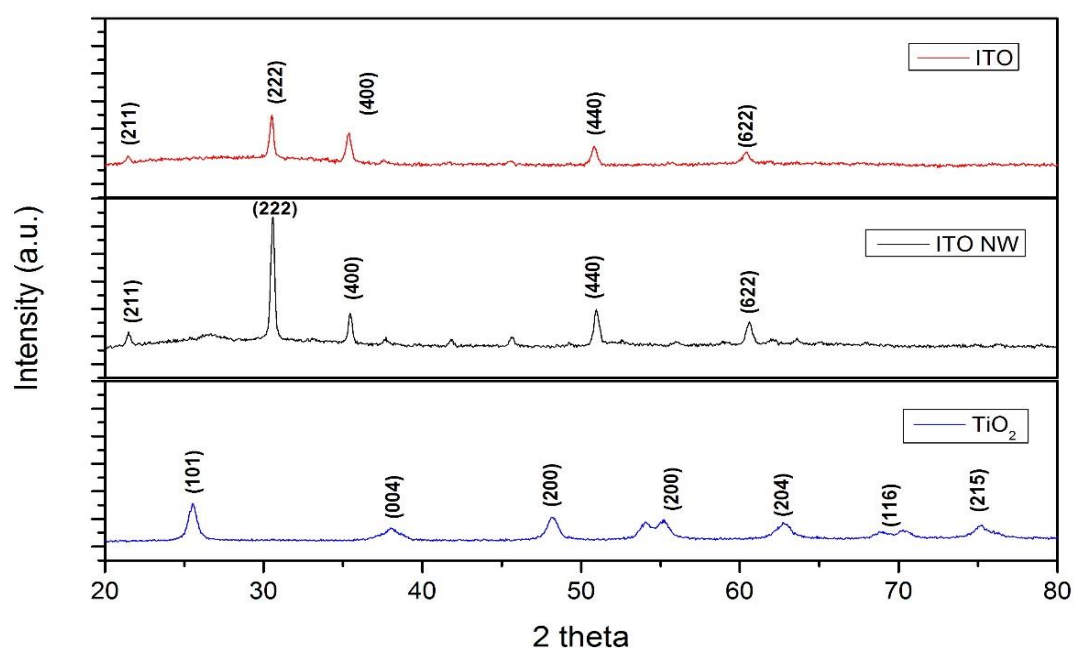


**Figure 5.4** XRD spectra for ITO, ITO NW, and TiO<sub>2</sub> particles obtained by sol-gel method.

Figure 5.4 illustrates the XRD patterns of bare ITO film, ITO NW and TiO<sub>2</sub> particles. The peaks in the XRD pattern reveal an oriented growth of ITO. On the XRD patterns of ITO films, sharp peaks of ITO have been detected at (211), (222), (400), (440) and (622) orientations. A sharp peak that represents (222) in the ITO-NW XRD pattern indicates a preferred (111) orientation of the ITO 1D structure. Therefore, the preferred (111) orientation implies that the tin source replaces indium substitutionally in the bcc lattice. This observation indicates the enhancement in crystallinity of ITO NW

obtained by sol-gel method. In addition, XRD results show that crystal structure of  $\text{TiO}_2$  powders is anatase, which matches up with JPDS no. 21-1272.

300 nm sol-gel based ITO film was used as a transparent conductive glass for DSSC application. A computer-controlled Keithley 2400 source meter with 300 W AM 1.5 simulated sunlight was employed to obtain the current density-voltage (J-V) characteristics. The active areas of all of ITO- $\text{TiO}_2$  DSSCs were  $0.25 \text{ cm}^2$ . The results of the current density-voltage (J-V) curves are given below in Table 5.1 and J-V characteristic curves are presented in Figure 5.5.

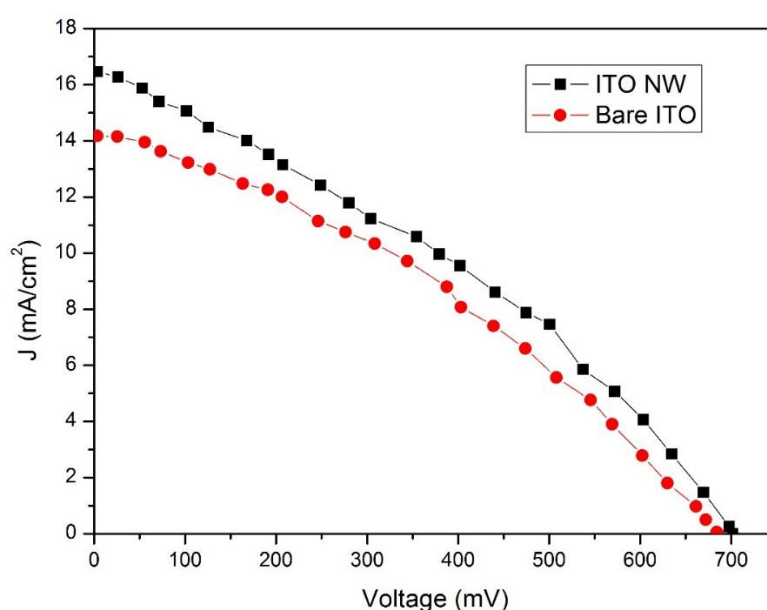


**Figure 5.5** Current density-voltage characteristics of DSSCs based on bare ITO and ITO NW.

The ITO NW based DSSC showed higher performance on efficiency than bare ITO based DSSC. The improvement on conversion efficiency could be explained by high  $V_{oc}$  and  $J_{sc}$  values.  $J_{sc}$  increases with ITO NW due to the improvement in contact surface between ITO NW and  $\text{TiO}_2$ .  $V_{oc}$  was improved by decreasing contact resistance between the ITO and  $\text{TiO}_2$  layers via 1D interaction. The ITO NW between ITO and  $\text{TiO}_2$  matrix prevents random electron transport and it is an alternative path for light generated current in the photoanode. Finally it inhibits power losses in DSSC.

In these aspects, ITO 1D nano structure production on ITO film before being coated by TiO<sub>2</sub> matrix generally improves photovoltaic efficiency. Due to TiO<sub>2</sub> anatase nano structure in conventional DSSCs, electrons cannot easily reach to the electrode surface. Hence, they accumulate on TiO<sub>2</sub> structure. Because of ITO 1D structure production on ITO film, ITO nanowires help the electrons to reach to the electrode surfaces causing an increase in the efficiency. That is why we observe higher conversion efficiency than bare ITO structures (5.03 % vs 4.32 %). ITO NW based DSSCs produced in this work showed higher conversion efficiency than literature such as 3.97% efficiency found by Iskandar et al. [24].

**Table 5.1** Efficiency analysis of ITO nanowire and TiO<sub>2</sub> nanopowder composite dye sensitized solar cells.

Sample	Fill Factor (%)	J <sub>sc</sub> (mA/cm <sup>2</sup> )	V <sub>oc</sub> (Volt)	Efficiency (%)
ITO NW	23.46	16.50	702	5.03
Bare ITO	29.21	14.25	697	4.32

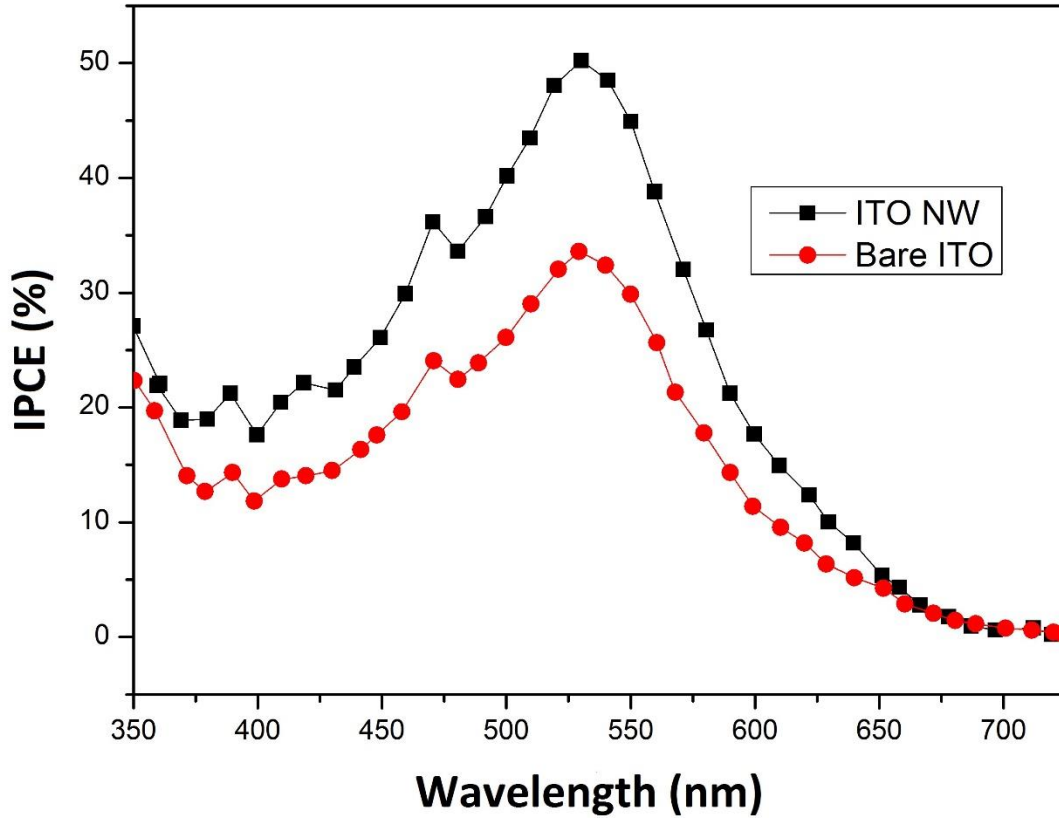


**Figure. 5.6** IPCE spectra of DSSCs based on bare ITO and ITO NW.

On the incident photon to current efficiency (IPCE) curve in Figure.5.6, the photosensitization of the TiO<sub>2</sub> electrodes in the visible region is observed. 540 nm peak is much higher than that of 460 nm, therefore, light absorption was more effective for 540 nm wavelength. The peak intensity and integrated area of the IPCE spectra in the visible region increase with ITO NW modification. Therefore, the IPCE of NW modified TiO<sub>2</sub> DSSC has risen up to 51% while the sample of bare ITO gave 32 % efficiency. The IPCE value was less than the literature values where ITO layers produced by high vacuum processes (nearly 90%-80%). It is because of recombination of electrons caused by high sheet resistance of the ITO layers produced by sol-gel method in this work (45 ohm/sq). However, the commercial sputtered ITO layers have sheet resistances of 5-8 ohm/sq. Yet, low cost and easy production were advantages of sol-gel method compared to the other high vacuum processes. The IPCE values decreased at wavelengths between 350 nm-400 nm ranges due to the light absorption of ITO layer. However, 59 % improvement has been observed in IPCE efficiency with respect to bare ITO, totally.

EIS technique has been widely used to investigate the kinetics of electrochemical and photo electrochemical processes occurring in DSSCs, supercapacitors and lithium cells. The impedance spectra of ITO NW based DSSC and bare ITO based DSSC were given in Figure 5.7.a. The experiments were performed under illumination ranging from 0.1 Hz to 100 kHz at  $V_{oc}$  values that were 702 mV for ITO NW based cells and 692 mV for bare ITO based cells. On the Nyquist plots of EIS spectra, two semicircles were observed. The small semicircle representing high frequency region has a frequency range lower than 0.1 MHz. Small semicircle was fitted to interfaces between Pt counter electrode/iodine electrolyte of chemical capacitance ( $C_{\mu}$ ) and charge transfer resistance ( $R_{ct}$ ). Second semicircle is observed on the low frequency region. The second semicircle was fitted to constant phase element and transport resistance ( $R_w$ ) of the injected electrons accumulated within  $TiO_2$  film and the charge transfer of either  $TiO_2$ /iodine electrolyte or ITO/ $TiO_2$  interface. In this respect, on the EIS model analysis in the DSSC, values of important EIS parameters ( $R_{ct}$  and  $R_w$ ) were calculated by Zsimpwin software. The calculated EIS data is given in Table 5.2.

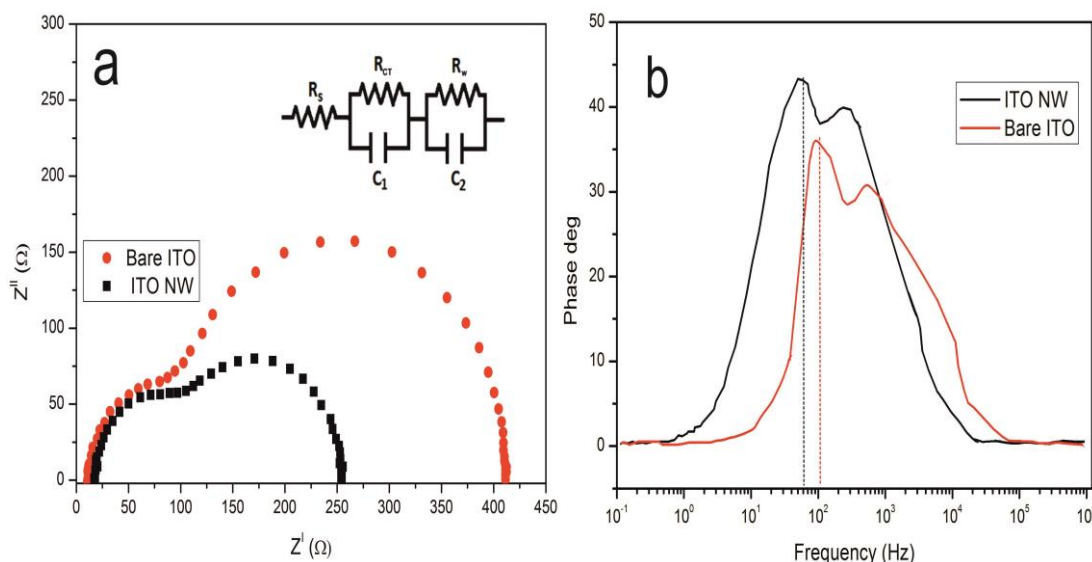


**Figure 5.7** EIS data analysis of ITO NW based DSSC and bare ITO based DSSC. Nyquist plots and EIS fitting system (in the inset) (a) and Bode plots (b).

According to Table 5.2, ITO NW based system gives the best performance by having low  $R_w$  and  $R_{ct}$  resistance values among all cells. In this study, lower  $R_w$  means that,

ITO NW system showed the most efficient charge transfer process at dye coated TiO<sub>2</sub> layer / ITO NW layer or dye coated TiO<sub>2</sub> / redox electrolyte interface. In addition, ITO NW system exhibited higher electron flow process between Pt counter electrolyte / redox electrolyte interfaces resulting in lowest Rct.

**Table 5.2** Kinetic parameters of ITO nanowire and TiO<sub>2</sub> nanopowder composite dye sensitized solar cells.

<b>Samples</b>	<b>Rs (<math>\Omega</math>)</b>	<b>Rct (<math>\Omega</math>)</b>	<b>Rw (<math>\Omega</math>)</b>	<b><math>\tau_e</math> (ms)</b>
Bare ITO	23.4	86.4	305.7	1.51
ITO NW	22.8	77.2	173.5	1.87

On the Bode phase plot of EIS spectra in Figure 5.7.b, frequency of charge transfer process at different interfaces was illustrated in frequency versus  $-\theta$  (angle) spectrum. The characteristic low frequency peaks ( $f_{max}$ ) are located at 105 Hz for bare ITO and 85 Hz for ITO NW photoanodes. The most important parameter affecting the efficiency of electron life time for recombination in DSSCs can be calculated by  $f_{max}$  value in the equation ( $\tau=1/2\pi f_{max}$ ).  $f_{max}$  value can be obtained from Bode plot characteristic peak. Recombination is inversely proportional to electron life time. Therefore ITO NW system has lower recombination possibility than bare ITO system in this study. Also, the low resistance and long electron life time enable the higher efficiency and rapid electron transport through a longer distance without higher resistance barrier. Although there are some studies on the nanowire addition on TiO<sub>2</sub> matrix in DSSC, only some of them have data on the conversion efficiency of produced cells. E. Joanni et.al [19] have produced ITO nanowires by laser ablation and measured the overall conversion efficiency about 0.15%. The conversion efficiency found by D. H. Kim et.al [23] using metal evaporation method was 1.4% for ITO nanowires. The conversion efficiency of 5.03% obtained in this study by sol-gel processing method was better than the similar DSSCs formed using ITO nanowires in the literature.

## 5.4. Conclusion

Semiconductor metal oxide nanowires (SCMONWs) which have one dimensional interaction and large surface-to-volume ratio are favorable materials for various quantum devices. Growth of these nanowires is commonly acquired by using expensive techniques requiring high vacuum and high temperature conditions, which also consume some hazardous raw materials during production. However, the sol-gel technique based on a wet chemical solution is used primarily for the fabrication of materials including metal oxides where low temperatures and non-vacuum conditions are utilized. Indium tin oxide (ITO) is generally used as a transparent conducting oxide for solar cells and LCD touch screen applications. In this work, indium tin oxide (ITO) nanoparticles, nanowires, and thin films were prepared on glass substrates by sol-gel technique and used for the production of nano-crystalline dye-sensitized solar cell (nc-DSSC), which is a recent type of relatively low-cost thin film solar cells. Structural, topographical and chemical analyses were performed using XRD, SEM and EDS. As a result of SEM analysis, it was confirmed that nanowires with 15 nm thickness and 500 nm length were obtained after 24 h treatment of ITO. 24 h treatment of ITO nanowires in nc-DSSCs resulted in an improvement of 29 % in the photon to energy conversion efficiency with respect to bare ITO system and 59 % incident photo current efficiency with respect to that of bare ITO based dye sensitized solar cells.



## REFERENCES

1. Oregan, B. and M. Gratzel, *A Low-Cost, High-Efficiency Solar-Cell Based on Dye-Sensitized Colloidal TiO<sub>2</sub> Films*. *Nature*, **353**(6346): p. 737-740. 1991.
2. Nazeeruddin, M.K., et al., *Raman Characterization of Charge-Transfer Transitions in Ligand-Bridged Binuclear Polypyridyl Complexes of Ruthenium(II)*. *Journal of the Chemical Society-Dalton Transactions*, (2): p. 323-325. 1993.
3. Barbe, C.J., et al., *Nanocrystalline titanium oxide electrodes for photovoltaic applications*. *Journal of the American Ceramic Society*, **80**(12): p. 3157-3171. 1997.
4. Zakeeruddin, S.M., et al., *Design, synthesis, and application of amphiphilic ruthenium polypyridyl photosensitizers in solar cells based on nanocrystalline TiO<sub>2</sub> films*. *Langmuir*, **18**(3): p. 952-954. 2002.
5. Nazeeruddin, M.K., et al., *Investigation of sensitizer adsorption and the influence of protons on current and voltage of a dye-sensitized nanocrystalline TiO<sub>2</sub> solar cell*. *Journal of Physical Chemistry B*, 2003. **107**(34): p. 8981-8987.
6. Gratzel, M., *Solar energy conversion by dye-sensitized photovoltaic cells*. *Inorganic Chemistry*, **44**(20): p. 6841-6851. 2005.
7. Ito, S., et al., *Fabrication of thin film dye sensitized solar cells with solar to electric power conversion efficiency over 10%*. *Thin Solid Films*, **516**(14): p. 4613-4619. 2008.
8. Bisht, H., et al., *Comparison of spray pyrolyzed FTO, ATO and ITO coatings for flat and bent glass substrates*. *Thin Solid Films*, **351**(1-2): p. 109-114. 1999.
9. Kovtyukhova, N.I. and T.E. Mallouk, *Conductive indium-tin oxide nanowire and nanotube arrays made by electrochemically assisted deposition in template membranes: switching between wire and tube growth modes by surface chemical modification of the template*. *Nanoscale*, **3**(4): p. 1541-1552. 2011.

10. Chopra, K.L., S. Major, and D.K. Pandya, *Transparent Conductors - a Status Review*. Thin Solid Films, **102**(1): p. 1-46. 1983.
11. Fabregat-Santiago, F., et al., *Mott-Schottky analysis of nanoporous semiconductor electrodes in dielectric state deposited on SnO<sub>2</sub>(F) conducting substrates*. Journal of the Electrochemical Society, **150**(6): p. E293-E298. 2003
12. Warschkow, O., et al., *Defect structures of tin-doped indium oxide*. Journal of the American Ceramic Society, **86**(10): p. 1700-1706. 2003
13. Warschkow, O., et al., *Defect cluster aggregation and nonreducibility in tin-doped indium oxide*. Journal of the American Ceramic Society, **86**(10): p. 1707-1711. 2003.
14. Park, N.G., et al., *Dye-sensitized TiO<sub>2</sub> solar cells: Structural and photoelectrochemical characterization of nanocrystalline electrodes formed from the hydrolysis of TiCl<sub>4</sub>*. Journal of Physical Chemistry B, **103**(17): p. 3308-3314. 1999
15. Kundu, S. and P.K. Biswas, *Synthesis of nanostructured sol-gel ITO films at different temperatures and study of their absorption and photoluminescence properties*. Optical Materials, **31**(2): p. 429-433. 2008
16. Cho, H. and Y.H. Yun, *Characterization of indium tin oxide (ITO) thin films prepared by a sol-gel spin coating process*. Ceramics International, **37**(2): p. 615-619. 2011.
17. Law, M., et al., *Nanowire dye-sensitized solar cells*. Nature Materials, **4**(6): p. 455-459. 2005.
18. Yoon, J.H., et al., *TiO<sub>2</sub> nanorods as additive to TiO<sub>2</sub> film for improvement in the performance of dye-sensitized solar cells*. Journal of Photochemistry and Photobiology a-Chemistry, **180**(1-2): p. 184-188. 2006
19. Joanni, E., et al., *Dye-sensitized solar cell architecture based on indium-tin oxide nanowires coated with titanium dioxide*. Scripta Materialia, **57**(3): p. 277-280. 2007.
20. Vomiero, A., et al., *Controlled growth and sensing properties of In<sub>2</sub>O<sub>3</sub> nanowires*. Crystal Growth & Design, **7**(12): p. 2500-2504. 2007.

21. Park, J.H., et al., *Wafer-Scale Growth of ITO Nanorods by Radio Frequency Magnetron Sputtering Deposition*. Journal of the Electrochemical Society, **158**(5): p. K131-K135. 2011.
22. Xue, X.Y., et al., *Synthesis and ethanol sensing properties of indium-doped tin oxide nanowires*. Applied Physics Letters, **88**(20). 2006.
23. Kim, D.H., Park, K.S, *Synthesis of TiO<sub>2</sub>/ITO Nanostructure Photoelectrodes and Their Application for Dye-sensitized Solar Cells*. Journal of the Korean Ceramic Society, **48**(1): p. 4. 2011.
24. Iskandar, F., et al., *Indium Tin Oxide Nanofiber Film Electrode for High Performance Dye Sensitized Solar Cells*. Japanese Journal of Applied Physics, **49**(1). 2010.



## CHAPTER 6

### APPLICATION OF WIDE BAND GAP ZRO<sub>2</sub> BLOCKING LAYER ON DYE SENSITIZED SOLAR CELLS

#### 6.1. Motivation of Chapter 6

Dye sensitized solar cells (DSSC) have been a potential alternative to silicon based solar cells compared to other excitonic solar cells [1-3]. The DSSC have the following advantages: its production is relatively easy and they have low cost. In addition, DSSCs also exhibit interesting optical properties like high transparency, which adds to their architectural application that make them suitable in architecture, and for work under low interior lighting conditions [4]. Working principle of DSSC can be defined as follows. The dye such as organic based or ruthenium bipyridyl complexes is excited by incident photons. Electrons of the dye are injected to the metal oxide mesoporous nanocrystalline wide band gap semiconductor such as TiO<sub>2</sub>, ZnO and SnO<sub>2</sub> deposited onto transparent conductive glass (TCO), realizing high optical transmittance and high electrical conductivity and low work function such as In-doped SnO<sub>2</sub> (ITO) or F-doped SnO<sub>2</sub> (FTO) and transported through the nanoparticles network. The dye is regenerated by redox electrolyte such as iodine/iodide. Increase in the efficiency of DSSCs is strongly related with the dye adsorption, photon absorption, charge injection, charge transport, lower recombination, dye regeneration efficiencies, open circuit voltage, fill factor and incident photon to current conversion ability of the cell [5, 6].

In the conventional DSSCs, the charge carrier recombination takes place at TiO<sub>2</sub>/dye/electrolyte and transparent-conducting oxide (TCO)/electrolyte interfaces [7, 8]. The interface between the TiO<sub>2</sub> nanoparticles and the TCO is exposed to the electrolyte due to the porous structure of the TiO<sub>2</sub> layer. The electron leakage by

backward transfer takes place from the TCO layer to the electrolyte. Thus, limiting the backward electrons at these interfaces is one of the most important ways to improve the power-conversion efficiency of DSSC [9, 10]. As it is shown in Figure 6.1, Electron Blocking Layer (EBL), which is typically composed of a thin film coating on TCO, is significant for reducing undesirable charge carrier recombination. Optimizing the thickness and quality of EBL is important for device performance.

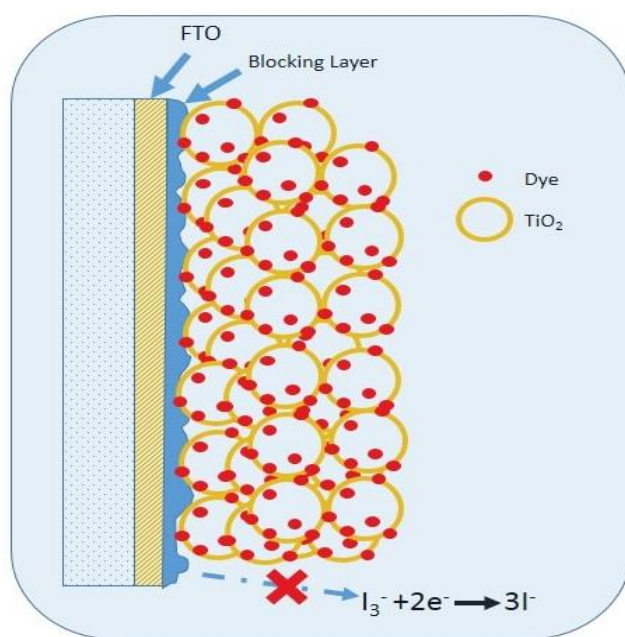


**Figure 6.1** Schematic illustration of blocking layer modified photoanode.

Generally, to prevent the backward recombination reaction, a TiO<sub>2</sub> thin layer as EBL is coated using TiCl<sub>4</sub> hydrothermal treatment or by spray pyrolysis using TiO<sub>2</sub> alcoholic solvents on TCO [11, 12]. However, TiO<sub>2</sub> layer deposited on TCO causes a decrease in the transparency values resulting in reduced interior light inside the cell. Therefore, several metal oxides, which have wider band gap than TiO<sub>2</sub> such as Al<sub>2</sub>O<sub>3</sub>, ZnO, CuO and Nb<sub>2</sub>O<sub>5</sub> have been employed as EBL on TCO layer [13-18]. According to our best knowledge, no work related to ZrO<sub>2</sub> as EBL has been reported. Generally, the EBL prepared by spray-pyrolysis, spin-coating method or hydrothermal treatment on TCO results in decreased series resistance, increased shunt resistance, and minimized electron leakage meaning an enhancement in the photovoltaic (PV) performance. In order to obtain highly efficient cell, EBL thickness, its crystal

structure, resistivity and optical properties of FTO and blocking layer structure have to be clarified [19].

In this work (Figure 6.2), EBL performance of  $ZrO_2$  has been realized for the first time in the literature. The work also highlighted the experimental conditions for the production of highly transparent  $ZrO_2$  – EBL that has low charge carrier resistance for the minimization of DSSC efficiency loss. In addition, optical properties at the interfacial region between mesoporous  $TiO_2$  and  $ZrO_2$  – EBL have been investigated using Uv-Vis analysis. Current density–voltage characteristics (J–V), electrochemical impedance spectroscopy (EIS) and incident photon-to-current efficiency (IPCE) have been studied to better understanding of the kinetics governing the photovoltaic properties.

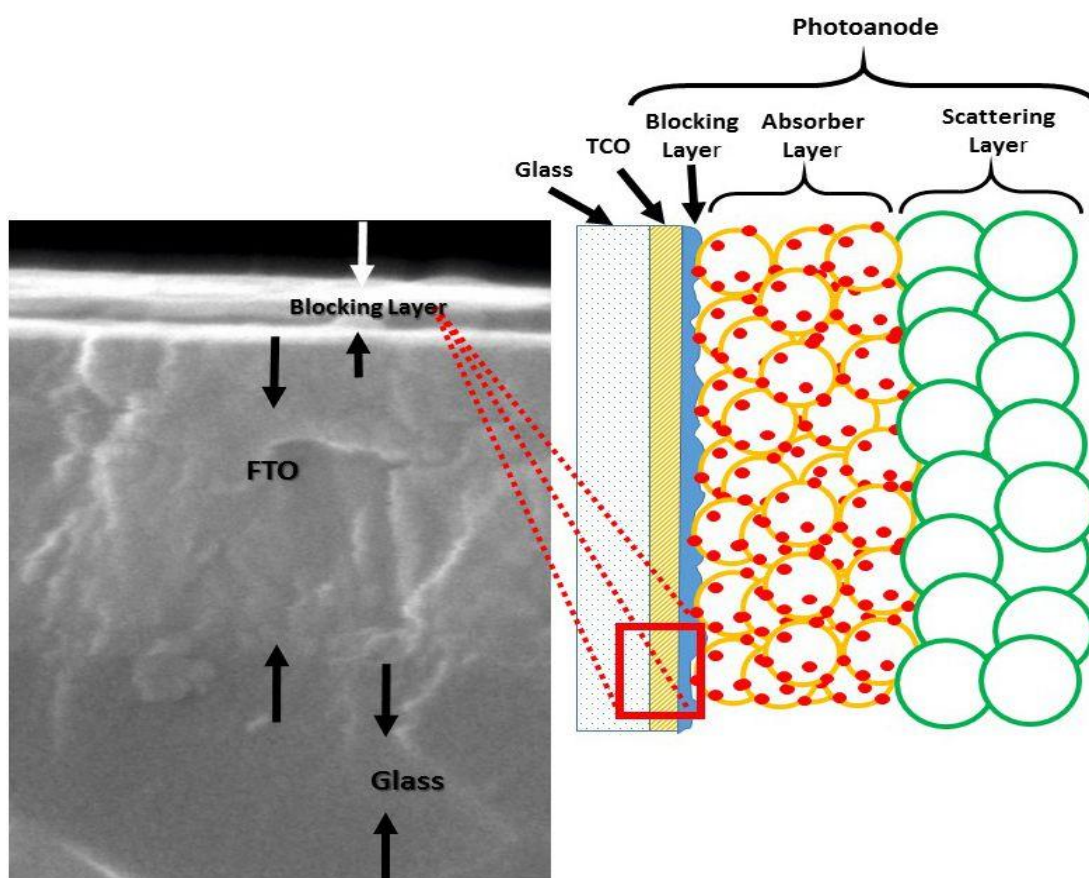


**Figure 6.2** Schematic description of chapter 6.

## 6.2. Experimental

### 6.2.1. Production of Blocking Layers

In this study, hydrothermal process has been applied in the following stages. First of all, each of commercial FTO substrates (TEC15, Pilkington) was ultrasonically cleaned in a sequence of detergent solution, deionized water, acetone, and isopropanol for 15 min under sonication and subsequently dried with nitrogen gas. Blocking layer deposition on FTO surface was conducted before the preparation of TiO<sub>2</sub> photoanode. The TiO<sub>2</sub> blocking layer was coated on the conductive side of the FTO glass by applying TiCl<sub>4</sub> hydrothermal treatment [11]. The coating of the ZrO<sub>2</sub> blocking layer was again done on the conductive side of FTO glass using a hydrothermal treatment in the following steps. FTO glass was immersed in 5 mM zirconium (IV) n-propoxide (sigma-Aldrich) dissolved in ethanol (sigma-Aldrich) at 80 °C in a Teflon lined autoclave and annealed at 500 °C for 2 h.

#### 6.2.1. DSSC Cell Production

The DSSC photoanodes were prepared with TiO<sub>2</sub> paste (Dyesol DSL-90T) by screen printing method using a 90 T mesh on ZrO<sub>2</sub>/FTO, TiO<sub>2</sub>/FTO and bare FTO [20]. The cell active area, measured by surface profilometer, was 0.25cm<sup>2</sup> and thickness of the TiO<sub>2</sub> film was 14 μm. The screen-print coated samples are dried at 120 °C for 30 min and slowly annealed under open air atmosphere consecutively at 325 °C for 5 min, at 375 °C for 15 min, 450 °C for 15 min, and 500 °C for 15 min. After heat treatment, photoanodes are immersed in 0.5 mM N719 (Solaronix) dye solution at room temperature for 24 h in the dark. H<sub>2</sub>PtCl<sub>6</sub>·6H<sub>2</sub>O solution was used for the preparation of counter electrodes. A droplet of 5 mM H<sub>2</sub>PtCl<sub>6</sub>·6H<sub>2</sub>O in ethanol was coated on FTO surface by spin coater, then it was heated at 400 °C for 15 min. The photoanode and the counter electrode were sealed together using a 25 μm thick Surlyn film at 100 °C. The electrolyte solution (Solaronix AN50) was injected into closed cell through the drilled holes on the counter electrode glass. Finally, the drilled holes were sealed using Surlyn, afterwards the cell was tested immediately [21].

### 6.3. Results and Discussion

#### 6.3.1. FE-SEM and XPS Analysis of Coated and Uncoated FTO Surfaces

In order to determine the thicknesses and surface morphologies of the coated and uncoated FTO films, FE-SEM analyses were conducted and the results were presented in Figure. 6.3. It is clearly seen that  $ZrO_2$  was more successfully coated than  $TiO_2$  on FTO surface. The reason can be given as the sedimentation of  $TiO_2$  film on FTO surface due to  $TiCl_4$  treatment. The maximum thickness of the bare FTO is 490 nm determined by FE-SEM. Thickness of  $TiO_2$  blocking layer was 56 nm, while  $ZrO_2$  was 48 nm. The difference between blocking layer thicknesses is not significant, therefore  $TiO_2$  and  $ZrO_2$  blocking layers can be compared in this study [22].

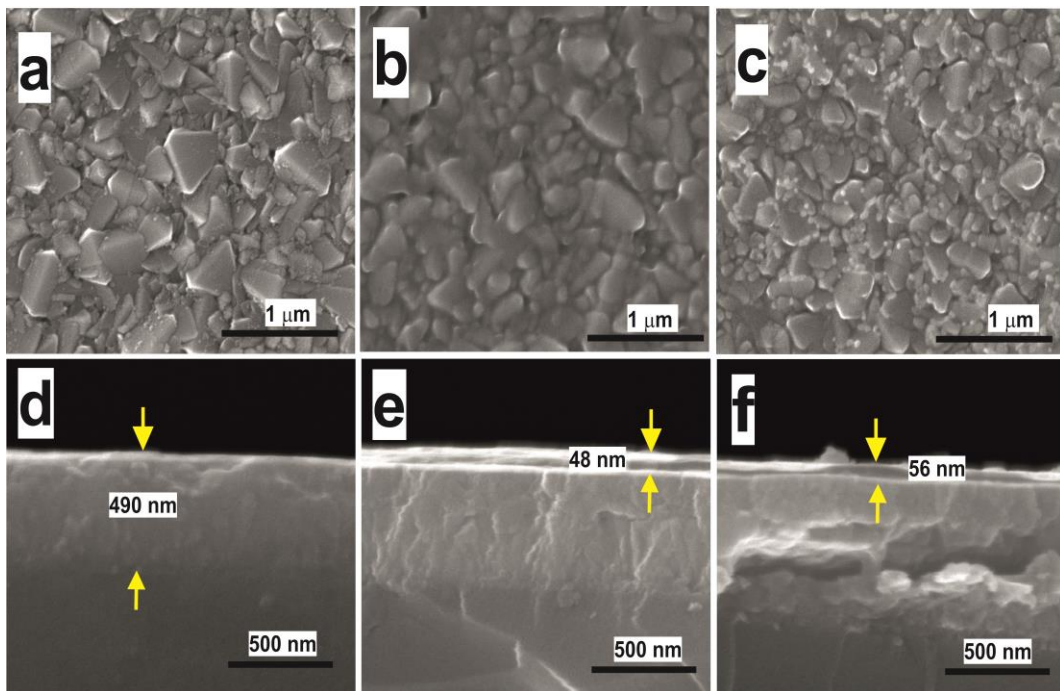


**Figure 6.3** Top view FE-SEM images of bare FTO (a),  $ZrO_2$ / FTO (b), and  $TiO_2$ / FTO (c); cross-sectional FE-SEM images of bare FTO (d),  $ZrO_2$ / FTO (e), and  $TiO_2$ / FTO (f).

The thickness of the FTO layers was about 490 nm, and those of  $ZrO_2$  and  $TiO_2$  were about 48 and 56 nm, respectively.

X-ray photoelectron spectroscopy (XPS or ESCA) has been considered as one of the best techniques for studying the dispersion of  $ZrO_2$  films on various substrates due to its high surface sensitivity and to gain knowledge on the type of interaction and stoichiometry, involved between  $ZrO_2$  film and different substrates [23, 24]. Thus, XPS has been utilized for the general characterization of  $ZrO_2$  on FTO. The XPS survey analysis of  $ZrO_2$ /FTO sample is shown in Figure 6.4.a. In addition, Figure 6.4.b presents the Zr 3d XPS spectrum obtained from 48 nm thick  $ZrO_2$  film deposited on FTO. The 3d doublet splitting is observed at 2.4 eV and Zr 3d 5/2 appears at binding energy (BE) of 182.9 eV, which corresponds to  $ZrO_2$  [25] and confirms the presence of  $ZrO_2$  on FTO.

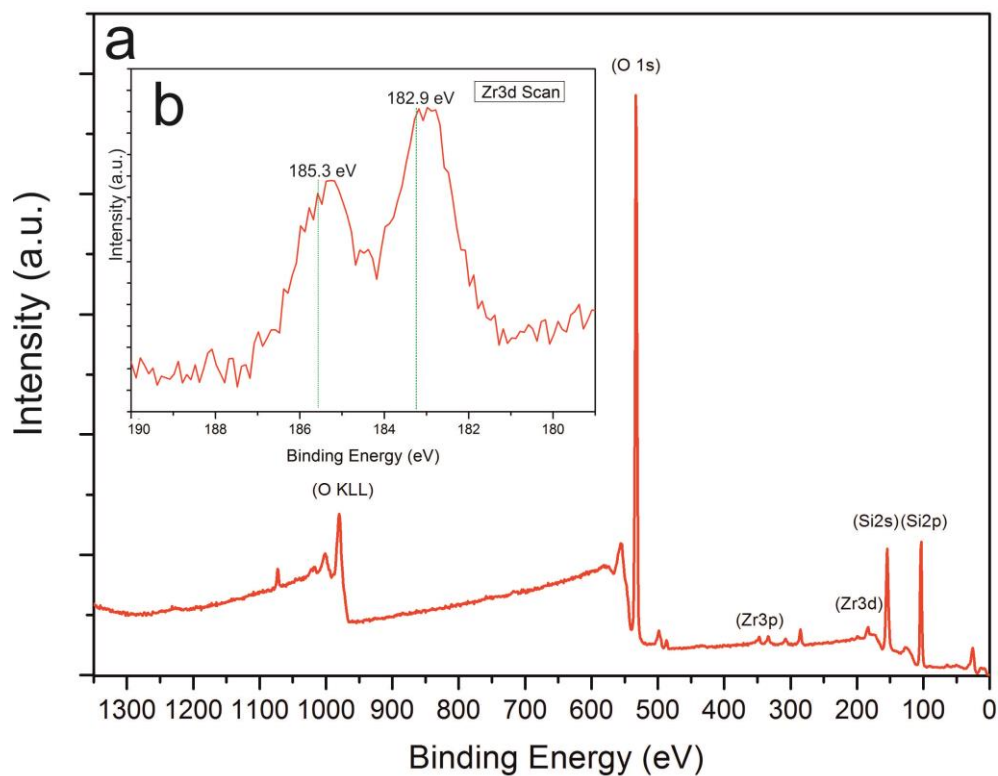


**Figure 6.4** XPS survey spectrum with surface composition of  $ZrO_2$ /FTO sample (a) and Zr 3d XPS spectra of  $ZrO_2$ /FTO sample (b).

### 6.3.3. UV-Vis Spectrophotometer Analysis of Coated and Uncoated FTO Surfaces

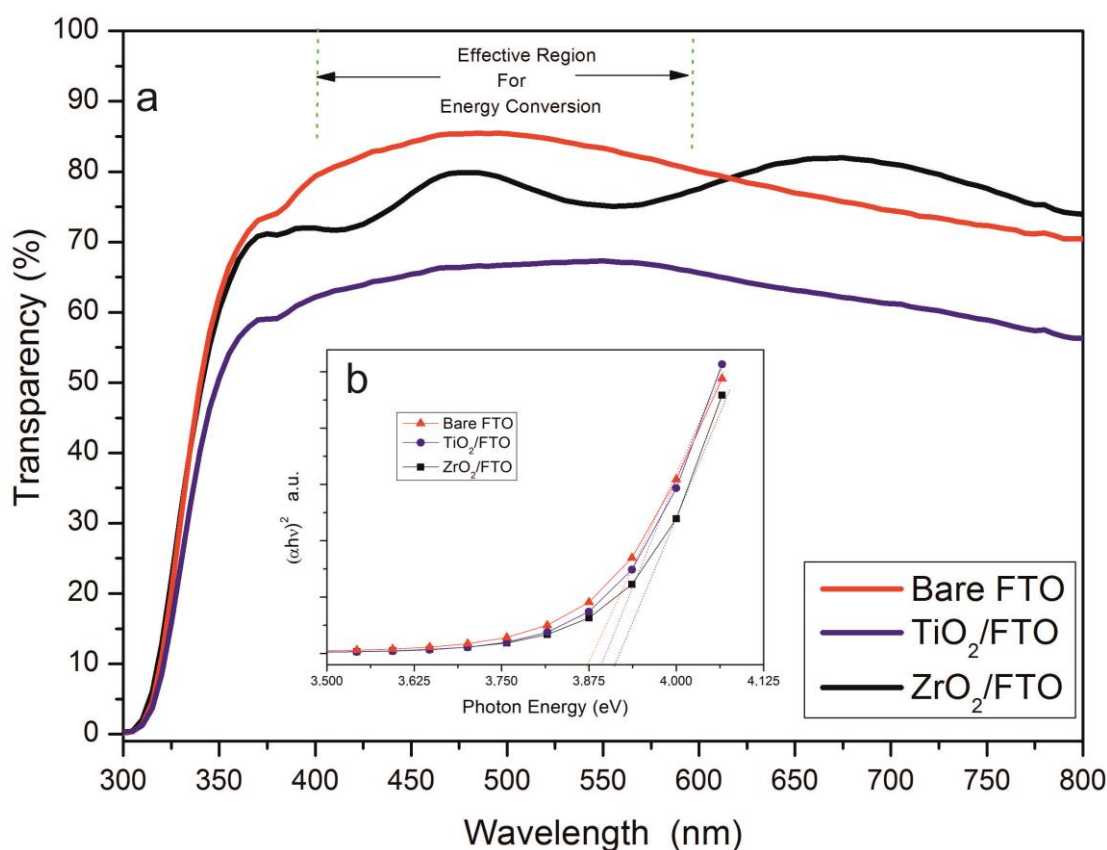


**Figure 6.5** Transmittance spectra for bare FTO, 48 nm ZrO<sub>2</sub>/FTO and 56 nm TiO<sub>2</sub>/FTO layers in visible region from 300 to 800 nm (a) and linear portion of the  $(ahv)^2$  vs photon energy E (eV) graph of bare FTO, 48 nm ZrO<sub>2</sub>/FTO and 56 nm TiO<sub>2</sub>/FTO layers (b).

UV-Visible measurements were conducted to measure visible light transmission of the samples in visible region from 300 to 800 nm using UV-1900 UV-Vis Spectrometer. Figure 6.5.a shows the UV-Vis spectra of bare FTO, 48 nm ZrO<sub>2</sub>/FTO and 56 nm TiO<sub>2</sub>/FTO layers. Coated FTOs have lower transparency than bare FTO in the range of 300-620 nm. ZrO<sub>2</sub>/FTO shows the highest transparency above 620 nm wavelength which leads to photons to have more chance to reach TiO<sub>2</sub>-Dye region. In other words, more photoelectrons can be produced.

The band gap of coated and uncoated FTO films can be calculated from the transmission data in the lower wavelength region. By extrapolating the linear portion of the  $(\alpha h\nu)^2$  vs photon energy E (eV) graph gives the direct band gap of the sample. Figure 6.4.b. is the plot of  $(h\nu\alpha)^2$  vs photon energy E (eV) from which the direct optical band gap is calculated. The optical band gap is 3.885 eV for ZrO<sub>2</sub>/FTO, while it is 3.875 eV for bare and 3.880 eV for TiO<sub>2</sub>/FTO. It can be noticed that there was a blue shift in the UV-absorption edge of the ZrO<sub>2</sub>/FTO electrode relative to the bare FTO. Higher band gap means that ZrO<sub>2</sub>/FTO can absorb only limited incident light, and allow more light to be transmitted to TiO<sub>2</sub> – Dye region [26]. According to the Burstein–Moss effect, occupied donor electrons block the lowest state in the conduction band, which is responsible for the increased optical band-gap. The blue shift in the optical band-gap of the ZrO<sub>2</sub>/FTO electrode indicates that the surface Fermi level is shifted toward the higher energy side [27, 28]. This positive effect can be seen on the electrical properties of ZrO<sub>2</sub>/FTO surface as it is provided in Table 6.1. After annealing process, the sheet resistance of ZrO<sub>2</sub>/FTO becomes lower than annealed TiO<sub>2</sub>/FTO meaning that ZrO<sub>2</sub> preserved conductivity of FTO during the annealing process.

**Table 6.1** Sheet resistance analysis of electrodes produced using bare FTO, ZrO<sub>2</sub>/FTO and TiO<sub>2</sub>/FTO layers before and after heat treatment.

Sample	Sheet Resistance	
	(Ω/sq)	
	Before Annealing	After Annealing
ZrO <sub>2</sub> /FTO	16.7	17.5
TiO <sub>2</sub> /FTO	17.9	22.1
Bare FTO	14.1	14.9

#### 6.3.4. Photocurrent density–photo voltage measurements of DSSCs

The photocurrent density–voltage (J–V) measurements of the DSSCs were conducted by a Keithley model 2440 source measure unit. A solar simulator (Newport) equipped

with a 300 W Xenon lamp is used as a sun-light source, which light intensity was calibrated by Si solar cell under AM 1.5G one sun light intensity.

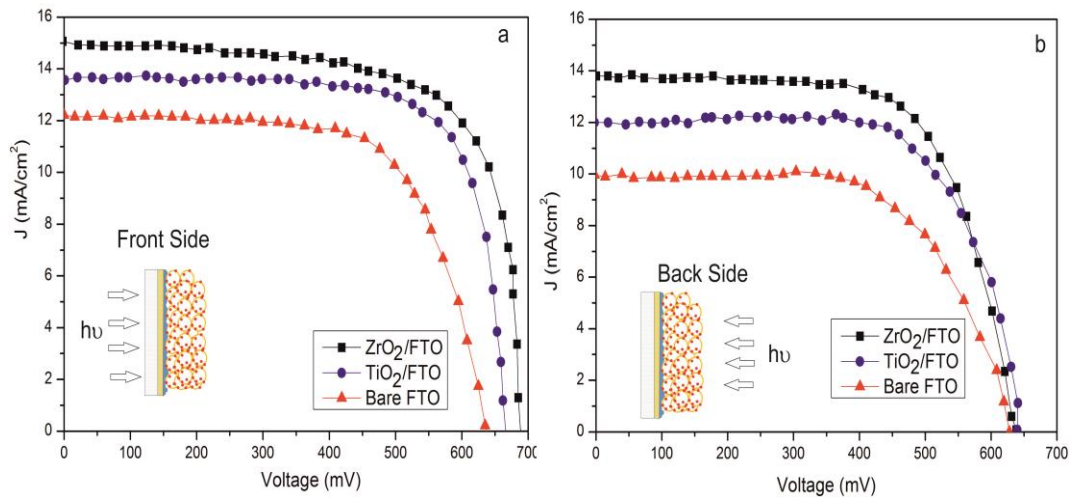


**Figure 6.6** J-V curves of DSSCs employing bare FTO, ZrO<sub>2</sub>/FTO and TiO<sub>2</sub>/FTO layers electrodes with **front** (a) and **backside** (b) illumination (AM 1.5, 100 mW/cm<sup>2</sup>).

Figure 6.6.a shows the photocurrent density - voltage curves of the DSSCs employing the bare FTO, TiO<sub>2</sub>/FTO, and ZrO<sub>2</sub>/FTO substrates using backside and front illumination, Table 6.2 summarizes their photovoltaic properties. In this study, a remarkable improvement in the overall efficiency of 43.9 % was ascribed on the front side illumination. However, it was found in the literature that the increase in the efficiency is approximately 30% - 53% using a compact layer on DSSC produced by high vacuum processes [29-31]. The increase in the  $J_{sc}$ ,  $V_{oc}$  and photovoltaic efficiency ( $\eta$ ) of the DSSCs incorporating the TiO<sub>2</sub>/FTO and ZrO<sub>2</sub>/FTO samples can be linked to a decrease in charge recombination by the blocking layer. Cell conversion efficiency ( $\eta$ ) of 6.77 % was obtained for the DSSC using ZrO<sub>2</sub> blocking layer, whereas TiO<sub>2</sub> blocking layer reached 5.72 % efficiency and the DSSC without a compact layer only attained efficiency of 4.71 %.

It can be seen that photocurrent density-voltage curves show different behavior according to direction of illumination. Surprisingly, ZrO<sub>2</sub> compact layer does not only improve the photovoltaic properties of DSSCs but also enhances the properties of

backside illumination. On the backside illumination, the short current density (Jsc) of ZrO<sub>2</sub>/FTO decreases by 8.79 % (from 15.13 to 13.80 mA/cm<sup>2</sup>). On the other hand, the short current density of bare FTO and TiO<sub>2</sub>/FTO decreases by 11.49 % (from 13.57 to 12.01 mA/cm<sup>2</sup>) and 16.46 % (from 12.08 to 10.09 mA/cm<sup>2</sup>), respectively. The considerable improvements on short current density of ZrO<sub>2</sub>/FTO can be attributed to optical transmittance and blue shift of energy band gap. The Voc of DSSC was improved from 640 mV to 680 mV after ZrO<sub>2</sub> blocking layer treatment and it was improved to 660 mV after employing TiO<sub>2</sub> blocking layer. These results may imply that both ZrO<sub>2</sub> and TiO<sub>2</sub> layers could improve Voc, which is typically associated with reduced recombination.

**Table 6.2** Efficiency analysis of DSSCs employing bare FTO, ZrO<sub>2</sub>/FTO and TiO<sub>2</sub>/FTO layer electrodes with front and backside illumination.

Sample	Backside illumination				Front illumination			
	Voc (mV)	Jsc (mA/cm <sup>2</sup> )	FF (%)	η (%)	Voc (mV)	Jsc (mA/cm <sup>2</sup> )	FF (%)	η (%)
ZrO <sub>2</sub> /FTO	630	13.80	59.02	5.13	680	15.13	65.86	6.77
TiO <sub>2</sub> /FTO	640	12.01	55.01	4.22	660	13.57	63.88	5.72
Bare FTO	630	10.09	51.22	3.25	640	12.08	60.97	4.71

### 6.3.5. Incident Photon to Current Efficiency (IPCE) Measurements of DSSCs

The IPCE is defined as the ratio of the number of electrons in the external circuit produced by an incident photon at a given wavelength. IPCE is directly related to the impact of blocking layer on the number of collected incident photons and the electrons produced in the circuit of the cell. In order to investigate the effect of the blocking layer on the spectral response improvement, the IPCE measurements were performed on DSSC cells and the results are given in Figure 6.7.

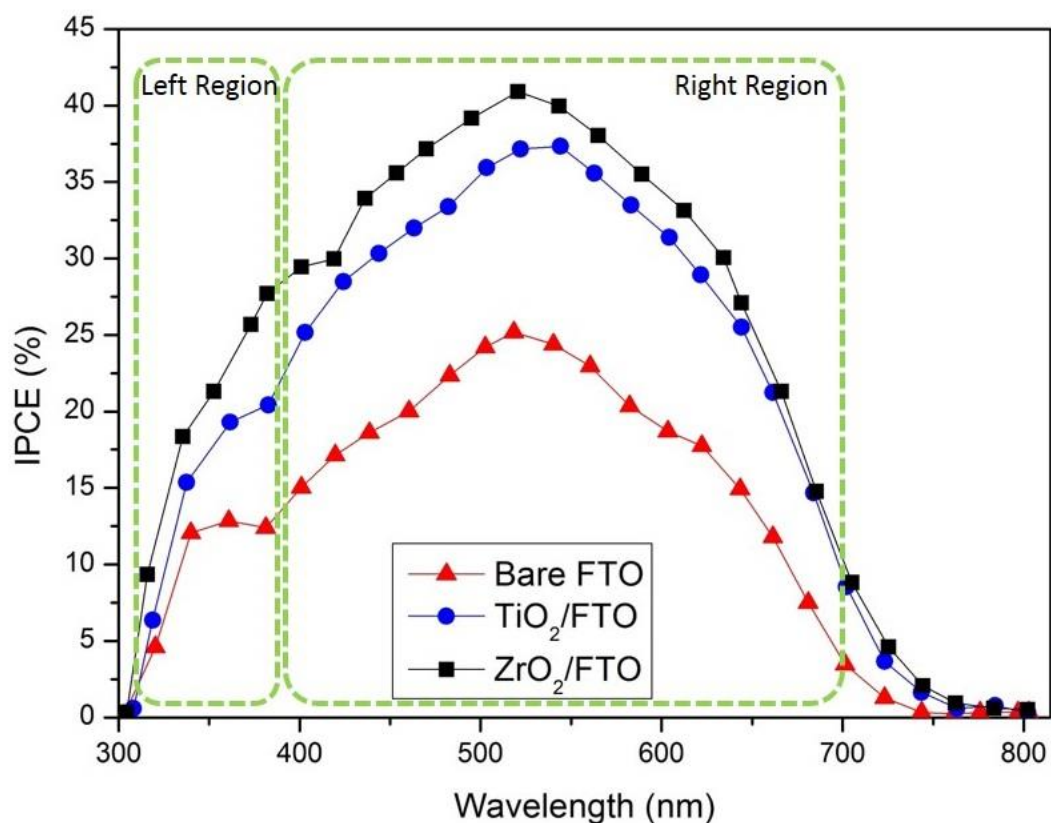


**Figure 6.7** IPCE spectra for the DSSCs with and without blocking layers.

The IPCE spectra indicated a similar behavior with the transmittance spectra of the samples given in Figure 6.7. The IPCE spectra can be analysed in two regions. The IPCE value of bare FTO decreases above 350 nm due to the absorption of uncoated FTO layer. The IPCE spectra one way or another simulates the transmittance behavior of samples. First region (left region) is below 390 nm in the IPCE spectra, has a small peak at 370 nm wavelength for the TiO<sub>2</sub> coated FTO glass. The peak in this first region is directly associated with the absorption in the band gap of TiO<sub>2</sub> nanoparticles [32]. Because of smaller molar absorption coefficient of photons in this first region, dye sensitization effect is less significant for DSSCs. N719 dye mainly absorbs photons and shows higher sensitization effect in the second region (right region) [33]. ZrO<sub>2</sub> coated FTO sample has a different peak than others at 420 nm. This peak is related to the red-shifted N719 dye peak, where the same peak appears below 400 nm for bare FTO. Therefore, red shift is an advantage on photovoltaic efficiency of the cell [34]. The second peak, which is accepted as N719 main peak in the literature, was observed at 550 nm on the right region [35]. DSSC produced using ZrO<sub>2</sub> blocking layer gave rise to IPCE efficiency of 39 % while bare FTO gives 23 % IPCE efficiency. ZrO<sub>2</sub>

blocking layer has an enhancing performance on IPCE spectra. Therefore, ZrO<sub>2</sub> blocking layer coated DSSCs showed 69 % total IPCE improvement when compared to bare FTO.

### 6.3.6. Electrochemical impedance spectroscopy of the DSSCs

“The electrochemical impedance spectroscopy (EIS) has been used as an investigation tool for the electron transport resistance and recombination in DSSCs [36, 37]. The Nyquist plots of the DSSCs with and without blocking layers were presented in Figure 6.8 under one sun illumination with the open-circuit conditions. In Figure 6.8.a, two semicircles were observed in the measured frequency range of 10<sup>-1</sup> to 10<sup>5</sup> Hz for both electrodes. Figure 6.8.b represents equivalent circuit of DSSC used for fitting impedance data which is calculated according to literature [38]. The resistance element R<sub>s</sub> in the high-frequency region is related to the sheet resistance of the FTO layer [36]. The other impedance elements can be described for the high frequency region of 10<sup>3</sup>–10<sup>5</sup> Hz ( $\omega_1$ ), low frequency region 1–10<sup>3</sup> Hz ( $\omega_2$ ), and 0.1–1 Hz ( $\omega_3$ ) region which can be associated with the charge transport in the conducting layer/TiO<sub>2</sub> or Pt counter electrode/electrolyte interfaces (Z<sub>1</sub>), the TiO<sub>2</sub>/dye/electrolyte interface (Z<sub>2</sub>), and the Nernstian diffusion in the electrolyte (Z<sub>3</sub>) [39]”.

The first semicircle, which is the resistance of the Z<sub>1</sub> component (R<sub>1</sub>), varies significantly with the addition of blocking layer. Due to an identical Pt counter electrode employed for each sample, the difference in the TiO<sub>2</sub>/FTO interface is fully responsible for the difference in Z<sub>1</sub> component (R<sub>1</sub>). According to Table 6.3, ZrO<sub>2</sub>/FTO has lower R<sub>1</sub> values. The photovoltaic efficiency has been positively affected with lower R<sub>1</sub>.

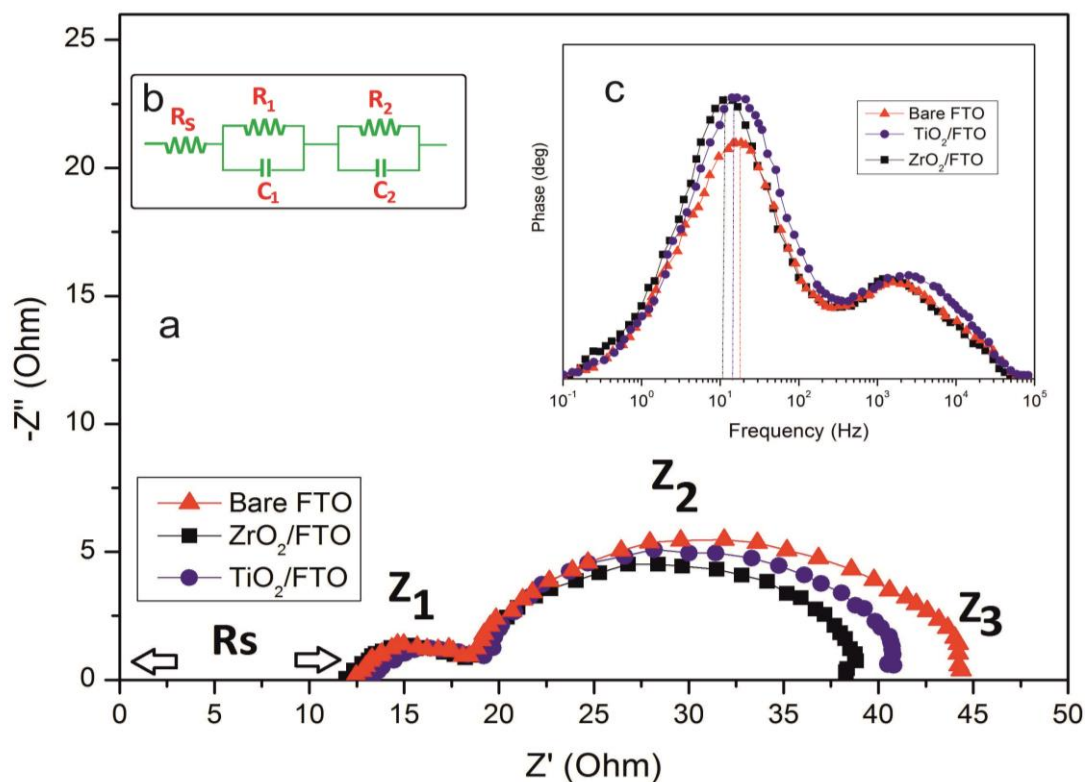


**Figure 6.8** Representative Nyquist plots displaying impedance data taken at open circuit potential (a), equivalent circuit of DSSC used for fitting impedance data (b), and Bode plots displaying impedance data (c).

The second semicircle represents the electron lifetime ( $\tau$ ) which is found using the frequency of maximum  $Z''$  at the  $Z_2$  semicircle.  $\tau$  can be calculated on the Bode plot. Lower  $R_2$  values correspond to lower electron transport resistance in DSSC. The  $ZrO_2/FTO$  has lower resistivity values which results in lower charge transport resistance. In this study, the second semicircle has more effect on DSSC photovoltaic efficiency than the first semicircle. Inset graph C of Figure 6.8 shows that  $ZrO_2/FTO$  has the highest electron lifetime. The frequency of charge transfer process at different blocking layer interfaces was shown in frequency versus – phase (angle) plot in Figure 6.8.c as the Bode phase plot of EIS spectra. The characteristic low frequency peaks ( $f_{max}$ ) are located at 18.49 Hz for bare FTO, 16.43 Hz for  $TiO_2/FTO$  and 10.92 Hz for  $ZrO_2/FTO$ . The most important parameter affecting electron lifetime for recombination in DSSCs can be calculated using Bode plot characteristic peak from  $f_{max}$  value using the equation of  $\tau = 1/2\pi f_{max}$  [39]. Recombination is inversely proportional to electron lifetime. Therefore,  $ZrO_2/FTO$  has lower recombination chance than other systems in this work. In addition, low resistance and long electron

lifetime enable the higher efficiency and rapid electron transport through a longer distance without facing with a high resistance barrier at least to a minimal extent. Table 6.3 summarizes the results of the EIS analysis fitted by using an equivalent circuit shown in the inset of Figure 6.7.

**Table 6.3** Kinetic parameters of the DSSCs with and without blocking layers.

Sample	$R_s$ ( $\Omega$ )	$R_1$ ( $\Omega$ )	$R_2$ ( $\Omega$ )	$\tau$ (s)
ZrO <sub>2</sub> /FTO	11.9	5.01	16.03	0.0146
TiO <sub>2</sub> /FTO	12.3	5.24	22.96	0.0097
Bare FTO	12.5	6.02	26.44	0.0086

To summarize, ZrO<sub>2</sub>/FTO layer having a sheet resistance of 16.7  $\Omega$ /sq and thickness of 48 nm was deposited on a commercial FTO substrate applying hydrothermal treatment. The decrease in conductivity after heat treatment is an important recombination parameter. ZrO<sub>2</sub> blocking layer also suppresses the resistivity of FTO, which was caused by annealing process. However, commercial TiO<sub>2</sub> blocking layer did not show better performance than ZrO<sub>2</sub> blocking layer on electrical properties. According to UV-Vis measurements of samples, the transparency of TiO<sub>2</sub>/FTO and ZrO<sub>2</sub>/FTO is sufficient enough to be used in DSSCs. Optical band gap of ZrO<sub>2</sub>/FTO sample shifted to higher energy state. In other words, Fermi level of FTO is shifted towards the higher energy side, and ZrO<sub>2</sub> has lower surface resistance than annealed TiO<sub>2</sub>/FTO. IPCE spectra directly illustrate the performance of external circuit electrons produced by an incident photon. IPCE results can reflect transmittance behavior of samples to some extent. Higher photon spectral response was observed on ZrO<sub>2</sub> blocking layer due to higher transparency of ZrO<sub>2</sub> blocking layer than TiO<sub>2</sub> blocking layer. DSSCs produced using ZrO<sub>2</sub> blocking layer showed 69 % improvement of total IPCE in comparison to bare FTO. These positive results were also confirmed by EIS study. ZrO<sub>2</sub> blocking layer reduced interfacial resistance effects, which increases the recombination time. ZrO<sub>2</sub> and TiO<sub>2</sub> have also prevented from the back-reaction of recombination that is caused by the electrolyte. The longer

recombination time affects photovoltaic properties positively. Finally,  $\text{ZrO}_2$  blocking layer enhanced the photovoltaic energy conversion efficiency by as much as 43.9 % for front side illumination, compared to the bare-FTO-based DSSC. The bare FTO based DSSC has the lowest performance in this study. Therefore, it can be concluded that  $\text{ZrO}_2$  blocking layer is a promising material for conventional TCO substrates.

#### **6.4. Conclusion**

A  $\text{ZrO}_2$  thin film was deposited on a fluorine-doped tin oxide (FTO) electrode by hydrothermal treatment and its application as a new blocking layer material for dye-sensitized solar cells (DSSCs) was investigated. According to current-voltage (*I-V*) characteristics and electrochemical impedance spectra (EIS), it was found that the  $\text{ZrO}_2$  layer functioned as both a blocking layer and a heat treatment protector for transparent conducting oxide (TCO) layer. The use of  $\text{ZrO}_2$  layer as blocking layer increases the electron lifetime and decreases the recombination from TCO to the electrolyte. In addition to photovoltaic performance,  $\text{ZrO}_2$  keeps resistivity of TCO stable after heat treatment compared to  $\text{TiO}_2$  blocking layer. As a result, the overall energy conversion efficiency of the DSSC with  $\text{ZrO}_2$  blocking layer was enhanced by 47 % for front side illumination compared to that of bare FTO substrate and 30 % compared to that of commercial  $\text{TiO}_2$  blocking layer for backside illumination. This study demonstrated that  $\text{ZrO}_2$  could be a promising alternative to the conventional  $\text{TiO}_2$  blocking layer for high efficiency DSSCs.



## REFERENCES

1. B. O'Regan, M.G., *Nature*,. **353**(737). 1991
2. Gratzel, M., *Inorganic Chem.*,. **44**(6841). 2005
3. Gratzel, M., *Nature* . **414**(338). 2001
4. Pettersson, H., et al., *Manufacturing method for monolithic dye-sensitized solar cells permitting long-term stable low-power modules*. *Solar Energy Materials and Solar Cells*,. **77**(4): p. 405-413. 2003
5. Nazeeruddin, M.K., et al., *Investigation of sensitizer adsorption and the influence of protons on current and voltage of a dye-sensitized nanocrystalline TiO<sub>2</sub> solar cell*. *Journal of Physical Chemistry B*, **107**(34): p. 8981-8987. 2003.
6. Snaith, H.J. and L. Schmidt-Mende, *Advances in liquid-electrolyte and solid-state dye-sensitized solar cells*. *Advanced Materials*, **19**(20): p. 3187-3200. 2007.
7. Cameron, P.J., L.M. Peter, and S. Hore, *How important is the back reaction of electrons via the substrate in dye-sensitized nanocrystalline solar cells?* *Journal of Physical Chemistry B*, **109**(2): p. 930-936. 2005.
8. Bisquert, J., et al., *Physical chemical principles of photovoltaic conversion with nanoparticulate, mesoporous dye-sensitized solar cells*. *Journal of Physical Chemistry B*, **108**(24): p. 8106-8118. 2004.
9. Lee, S., et al., *Enhancement of the photoelectric performance of dye-sensitized solar cells by using a CaCO<sub>3</sub>-coated TiO<sub>2</sub> nanoparticle film as an electrode*. *Solar Energy Materials and Solar Cells*, **90**(15): p. 2405-2412. 2006.
10. Ruhle, S. and D. Cahen, *Electron tunneling at the TiO<sub>2</sub>/substrate interface can determine dye-sensitized solar cell performance*. *Journal of Physical Chemistry B*, **108**(46): p. 17946-17951. 2004.
11. Choi, H., et al., *The effect of TiCl<sub>4</sub>-treated TiO<sub>2</sub> compact layer on the performance of dye-sensitized solar cell*. *Current Applied Physics*, **12**(3): p. 737-741. 2012.

12. Jiang, C.Y., et al., *Influences of alcoholic solvents on spray pyrolysis deposition of TiO<sub>2</sub> blocking layer films for solid-state dye-sensitized solar cells*. Journal of Solid State Chemistry, **198**: p. 197-202. 2013.
13. Palomares, E., et al., *Control of charge recombination dynamics in dye sensitized solar cells by the use of conformally deposited metal oxide blocking layers*. Journal of the American Chemical Society, **125**(2): p. 475-482. 2003.
14. Zaban, A., et al., *Bilayer nanoporous electrodes for dye sensitized solar cells*, in *Chemical Communications*. p. 2231-2232. 2000.
15. Xia, J.B., et al., *Sputtered Nb<sub>2</sub>O<sub>5</sub> as a novel blocking layer at conducting Glass/TiO<sub>2</sub> interfaces in dye-sensitized ionic liquid solar cells*. Journal of Physical Chemistry C, **111**(22): p. 8092-8097. 2007.
16. Xia, J.B., et al., *Fabrication and characterization of thin Nb<sub>2</sub>O<sub>5</sub> blocking layers for ionic liquid-based dye-sensitized solar cells*. Journal of Photochemistry and Photobiology a-Chemistry, **188**(1): p. 120-127. 2007.
17. Xia, J.B., et al., *Sputtered Nb<sub>2</sub>O<sub>5</sub> as an effective blocking layer at conducting glass and TiO<sub>2</sub> interfaces in ionic liquid-based dye-sensitized solar cells*. Chemical Communications, 2: p. 138-140. 2007.
18. Sahay, R., et al., *Synthesis and characterization of CuO nanofibers, and investigation for its suitability as blocking layer in ZnO NPs based dye sensitized solar cell and as photocatalyst in organic dye degradation*. Journal of Solid State Chemistry, **186**: p. 261-267. 2012.
19. Guai, G.H., et al., *Tailor and functionalize TiO<sub>2</sub> compact layer by acid treatment for high performance dye-sensitized solar cell and its enhancement mechanism*. Renewable Energy, **51**: p. 29-35. 2013.
20. Cosar, B., et al., *Photovoltaic performance of bifacial dye sensitized solar cell using chemically healed binary ionic liquid electrolyte solidified with SiO<sub>2</sub> nanoparticles*. Electrochimica Acta., **87**: p. 425-431. 2013.
21. Icli, K.C., H.I. Yavuz, and M. Ozenbas, *Production of core-shell type conducting FTO/TiO<sub>2</sub> photoanode for dye sensitized solar cells*. Journal of Solid State Chemistry, **210**(1): p. 22-29. 2014.

22. Lee, S., et al., *Nb-Doped TiO<sub>2</sub>: A New Compact Layer Material for TiO<sub>2</sub> Dye-Sensitized Solar Cells*. Journal of Physical Chemistry C, **113**(16): p. 6878-6882. 2009.
23. Guo, Y.J., et al., *XPS investigation of diffusion of two-layer ZrO<sub>2</sub>/SiO<sub>2</sub> and SiO<sub>2</sub>/ZrO<sub>2</sub> sol-gel films*. Optik, **120**(18): p. 1012-1015. 2009.
24. Botzakaki, M.A., et al., *ALD deposited ZrO<sub>2</sub> ultrathin layers on Si and Ge substrates: A multiple technique characterization*. Microelectronic Engineering, **112**: p. 208-212. 2013.
25. Guittet, M.J., J.P. Crocombette, and M. Gautier-Soyer, *Bonding and XPS chemical shifts in ZrSiO<sub>4</sub> versus SiO<sub>2</sub> and ZrO<sub>2</sub>: Charge transfer and electrostatic effects*. Physical Review B, **63**(12): p. art. no.-125117. 2001.
26. Qi, J.H., et al., *Dye-sensitized solar cell based on AZO/Ag/AZO multilayer transparent conductive oxide film*. Journal of Alloys and Compounds, **556**: p. 121-126. 2013.
27. Burnstein, E., Phys. Rev, **93**(632). 1954.
28. Sernelius, B.E., et al., *Band-Gap Tailoring of ZnO by Means of Heavy Al Doping*. Physical Review B, **37**(17): p. 10244-10248. 1988.
29. Ito, S., et al., *High-efficiency (7.2%) flexible dye-sensitized solar cells with Ti-metal substrate for nanocrystalline-TiO<sub>2</sub> photoanode*. Chemical Communications, **38**: p. 4004-4006. 2006.
30. Lim, S.P., et al., *Aerosol assisted chemical vapour deposited (AACVD) of TiO<sub>2</sub> thin film as compact layer for dye-sensitized solar cell*. Ceramics International, 2014.
31. Duong, T.T., et al., *Enhancing the efficiency of dye sensitized solar cells with an SnO<sub>2</sub> blocking layer grown by nanocluster deposition*. Journal of Alloys and Compounds, **561**: p. 206-210. 2013.
32. Gratzel, M., Journal of Photochemistry and Photobiology C: Photochemistry Reviews, **4**(2): p. 145-153. 2003.
33. Miyasaka, T., *Toward Printable Sensitized Mesoscopic Solar Cells: Light-Harvesting Management with Thin TiO<sub>2</sub> Films*. Journal of Physical Chemistry Letters, **2**(3): p. 262-269. 2011.

34. Abdullah, M.H. and M. Rusop, *Multifunctional graded index TiO<sub>2</sub> compact layer for performance enhancement in dye sensitized solar cell*. Applied Surface Science, **284**: p. 278-284. 2013.
35. Abdullah, M.H. and M. Rusop, *RF sputtered tri-functional antireflective TiO<sub>2</sub> (arc-TiO<sub>2</sub>) compact layer for performance enhancement in dye-sensitised solar cell*. Ceramics International, **40**(1): p. 967-974. 2014.
36. Boschloo, G. and A. Hagfeldt, *Activation energy of electron transport in dye-sensitized TiO<sub>2</sub> solar cells*. Journal of Physical Chemistry B, **109**(24): p. 12093-12098. 2005.
37. Mahrov, B., et al., *Photovoltage study of charge injection from dye molecules into transparent hole and electron conductors*. Applied Physics Letters, **84**(26): p. 5455-5457. 2004.
38. Adachi, M., et al., *Determination of parameters of electron transport in dye-sensitized solar cells using electrochemical impedance spectroscopy*. Journal of Physical Chemistry B, **110**(28): p. 13872-13880. 2006.
39. Fabregat-Santiago, F., et al., *Influence of electrolyte in transport and recombination in dye-sensitized solar cells studied by impedance spectroscopy*. Solar Energy Materials and Solar Cells, **87**(1-4): p. 117-131. 2005.

## CHAPTER 7

### OPTIMIZING NEW TYPE NANO-COMPOSITE Zr DOPED TiO<sub>2</sub> SCATTERING LAYER FOR EFFICIENT DYE SENSITIZED SOLAR CELLS

#### 7.1. Motivation of Chapter 7

Dye sensitized solar cell (DSSC) is a new type electrochemical photovoltaic solar cell which can be a candidate for an alternative device to replace silicon based solar cells [1]. Due to its high efficiency-cost ratio, DSSC has been popular in last two decades [2]. A conventional DSSC is composed of a transparent conductive substrate, a nanometer sized semiconductor absorber layer, a sensitizing dye, a redox electrolyte and a counter electrode [3]. Although a total conversion efficiency of can be obtained about 10 % in small areas, which is nearly 0.25 cm<sup>2</sup>, the efficiency, which has become limited by significant loss of radiation, should be improved for producing large scale modules in order to be commercialized [4-9]. In general, absorber layer, which is given Figure 7.1.a, composed of nanopowders with sizes 20 -30 nm having large surface areas is the place where effective photocurrent generation occurs [2, 10-13]. However, 20-30 nm semiconductor particles show low light absorption, weak light scattering and charge trapping at grain boundaries. The charge trapping problem at grain boundaries can be solved by using a photo electrode, composed of TiO<sub>2</sub> nanoparticles treated with TiCl<sub>4</sub>, which is known as an electron blocking layer (EBL) [14]. The difficulty arising from ineffective light absorption and weak light scattering of absorber layer should be addressed to increase the use of incident light and power generation [15-18]. In the past decades, in order to overcome limited efficiency barrier problem, several scattering layers (SL) such as bilayer structure based on TiO<sub>2</sub> nanowire-covered nanotube, double-layer structure with TiO<sub>2</sub>, TiO<sub>2</sub> hollow sphere nanoparticles, multilayer structure of TiO<sub>2</sub> particles with different size, carbon spheres/TiO<sub>2</sub>

nanoparticle composites, ZnO particles and silver nanoparticle doped TiO<sub>2</sub>, nanofiber films and ZrO<sub>2</sub> particles, which is a new way to extend the light path, have been performed to enhance the light harvesting efficiency [4, 16, 17, 19-24].

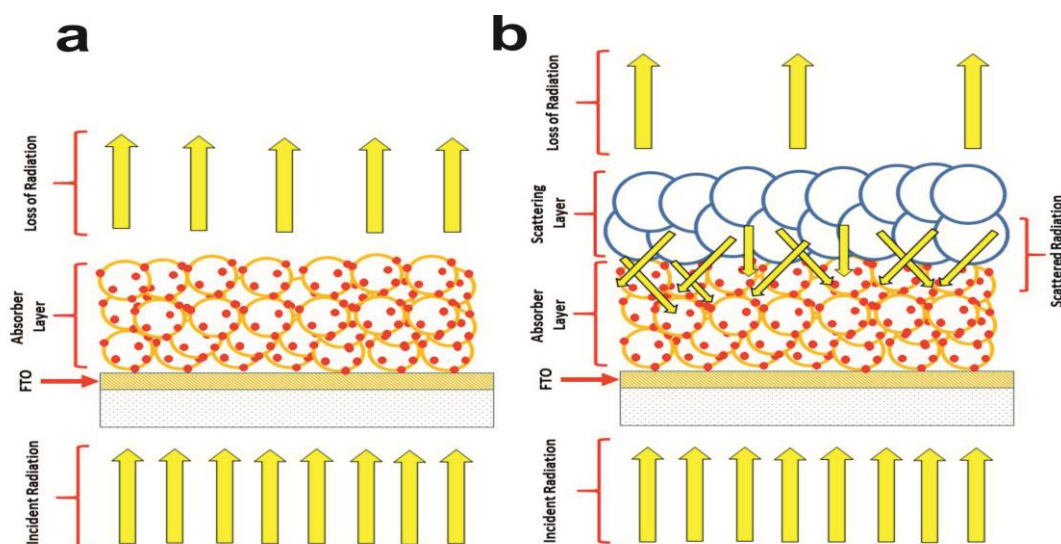


**Figure 7.1** Comparison of DSSC schematics. DSSC with an absorber layer of anatase (a), DSSC with an absorber layer and scattering particles (b).

A suitable scattering layer has different characteristics like larger particle size (>100 nm) than the particles in the absorber layer and it should not have any reducing effect on dye loading characteristics of absorber layer. Nevertheless, traditional scattering layers reduce the dye loading capacity of the absorber layer, which is a challenge to achieve highly efficient cells. In working out this problem, production of scattering layer that has positive effect on dye loading capacity of DSSC is important [17, 20, 21]. Different grain growth mechanisms and preservation of anatase-to-rutile phase transitions have been reported for Zr doped TiO<sub>2</sub>, for the use of phase-stable anatase nanoparticles in, e.g., catalytic applications and DSSC applications. To produce a suitable effective SL, the classical SL, which is composed of larger anatase rutile mixed particles can be modified by Zr doping. In this study, 10% Zr doped TiO<sub>2</sub> (ZDT) has been synthesized by hydrothermal method and used as a scattering layer to improve photo conversion efficiency of DSSC as illustrated in Figure 7.2.

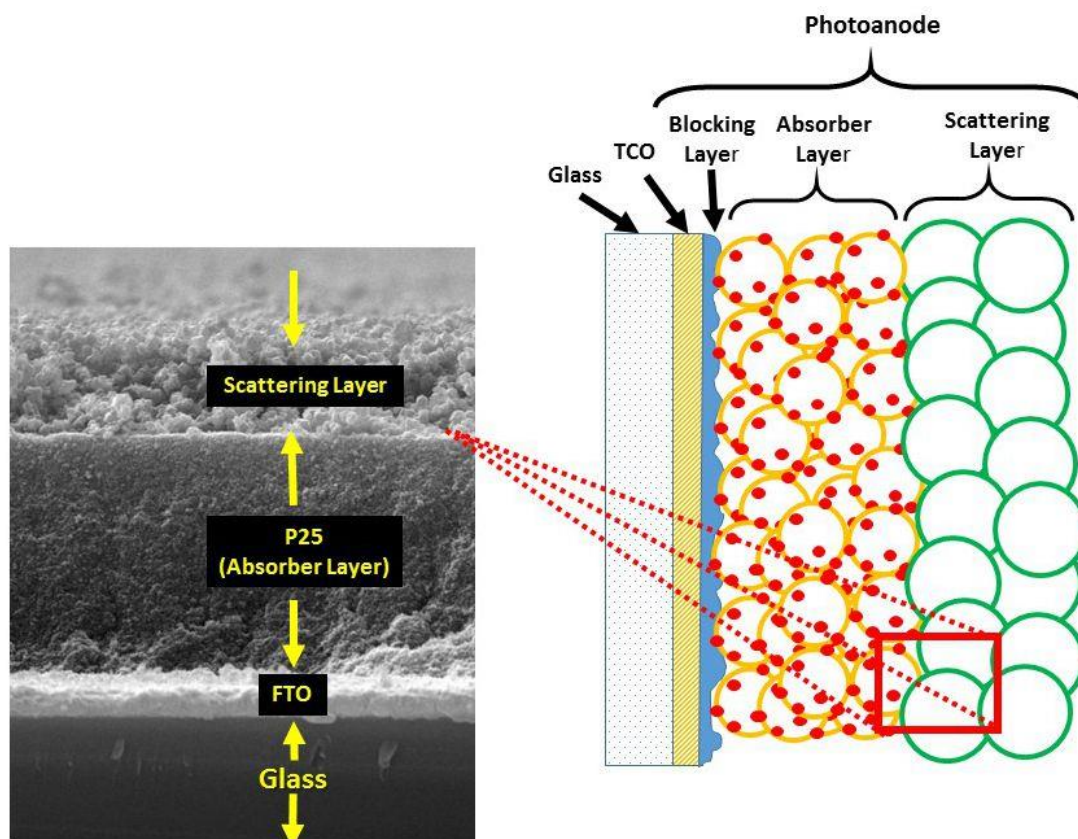


**Figure 7.2** Schematic description of chapter 7

## 7.2. Experimental

### 7.2.1. Scattering Particle Preparation

Zr doped  $\text{TiO}_2$  scattering particles (ZDT) were obtained from homogeneous solution precipitation technique and following hydrothermal treatment in autoclave. 0.1 M Ti (but) and 0.01 M Zr butox were dissolved in 2 metoxy methanol, isopropanol mixture (50:50 wt%). The solution was heated up to  $80^\circ\text{C}$  for 2 h under reflux. A bluish gel was formed when the solution was cooled to room temperature. The bluish gel was transferred into titanium autoclave where hydrothermal treatments were performed at  $190^\circ\text{C}$  for 24 h. Hydrothermally treated wet gel was then centrifuged and washed to remove excess ions. Finally, homogenously precipitated particles were annealed under open atmosphere at  $500^\circ\text{C}$  for 1 h. After annealing, the particles were homogenized by ultrasonic and mechanic homogenizer. Undoped  $\text{TiO}_2$  scattering particles (T) were

obtained using the same procedure as above except the addition of 0.01 M Zr during hydrothermal treatment. The screen printing paste of SL and absorber layer was prepared with the addition of ethyl cellulose and terpineol (20:10:70).

### **7.2.2. DSSC Sample Preparation**

The preparation details of photoanode for DSSC were described using the following procedure. FTO substrates were treated by 0.05 M titanium tetrachloride aqueous solution at 70°C in order to eliminate back transfer leakage of photo generated electrons. Absorber layer (0-SL) was prepared by P25 purchased from Evonik® and were deposited on FTO coated glass substrates (TEC-15, 15 ohm/sq) by using screen printing technique. ZDT scattering layer (ZDT-SL) and undoped TiO<sub>2</sub> scattering layer (T-SL) were deposited on 0-SL by the same technique.

To understand the effect of ZDT particles used as scattering layer on photovoltaic performance better, they were compared with T-SL and 0-SL photoanodes. All of the photoanodes were heated at 500°C for 45 min to burn organic binders and sinter nanoparticles. Each of the photoanode samples were immersed in 50 mM N719 (Solaronix) dye solution in dried acetonitrile for 24 h. Counter electrodes were prepared by dipping them in 0.01 M hexachloroplatinic acid - isopropanol solution and by annealing at 450°C. Two electrodes were laminated using Surlyn (25 micron) frames at 120°C. Electrolyte (0.6 M butylmethylimidazolium iodide, 0.03 M I<sub>2</sub>, 0.1 M guanidinium thiocyanate, 0.5 M 4-tert- butylpyridine) was injected through a hole on the counter electrode.

### 7.3. Results and Discussion

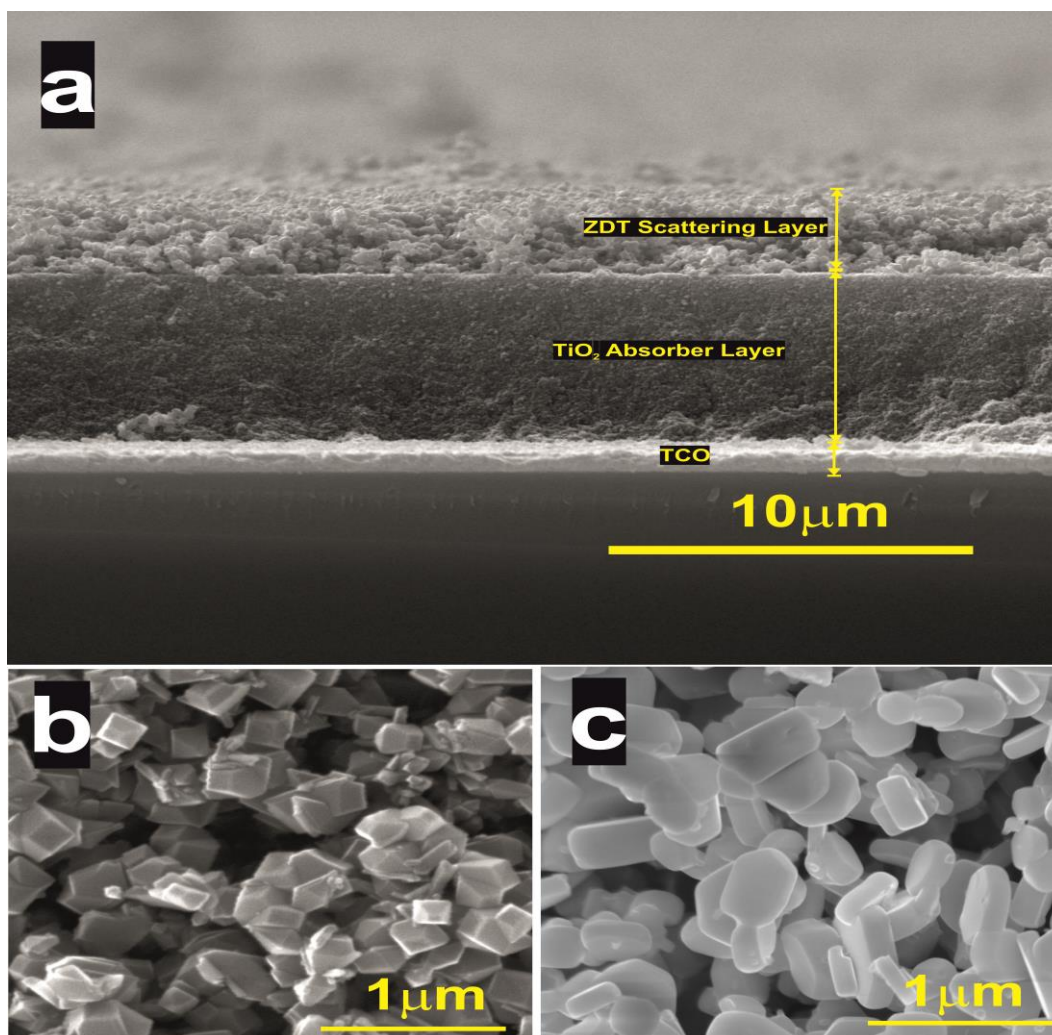


**Figure 7.3** FE-SEM image of cross sectional view of double-layer film containing P25 TiO<sub>2</sub> particles as the under-layer and ZDT particles as the over-layer (a), and top view of ZDT (b) and T (c) scattering particles.

Figure 7.3.a shows detailed SEM photoanode images of the composite structure that consists of ZDT scattering layer coated on top of TiO<sub>2</sub> mesoporous layer. As can be seen from Figure 7.3.a, TiO<sub>2</sub> mesoporous layer displays a morphology with smooth and porous surface while ZDT scattering layer structure has higher roughness than TiO<sub>2</sub> layer. Nevertheless, any mismatch or cracks have not been detected between TiO<sub>2</sub> and ZDT at full length of boundary. In Figure 7.3.b, top view of ZDT particles, where scattering effect is seen on charge collection, was illustrated. Polyhedron particles with different sizes (100 nm – 200 nm) were seen. 800-1200 nm particles were detected on

undoped  $\text{TiO}_2$  particles given in Fig.7.3.c. According to previous studies in the literature, different sized composite material was found as suitable for DSSC application to obtain more photo current generation. The bigger particles were used as scattering structure. Although photo-generation on scattering layer is not considered to be important due to the electron path length, smaller particles can be used as photons for current generation. Therefore, ZDT particles could show light scattering effect if applied to the top of absorber layer of DSSC for enhancing the light harvesting efficiency.

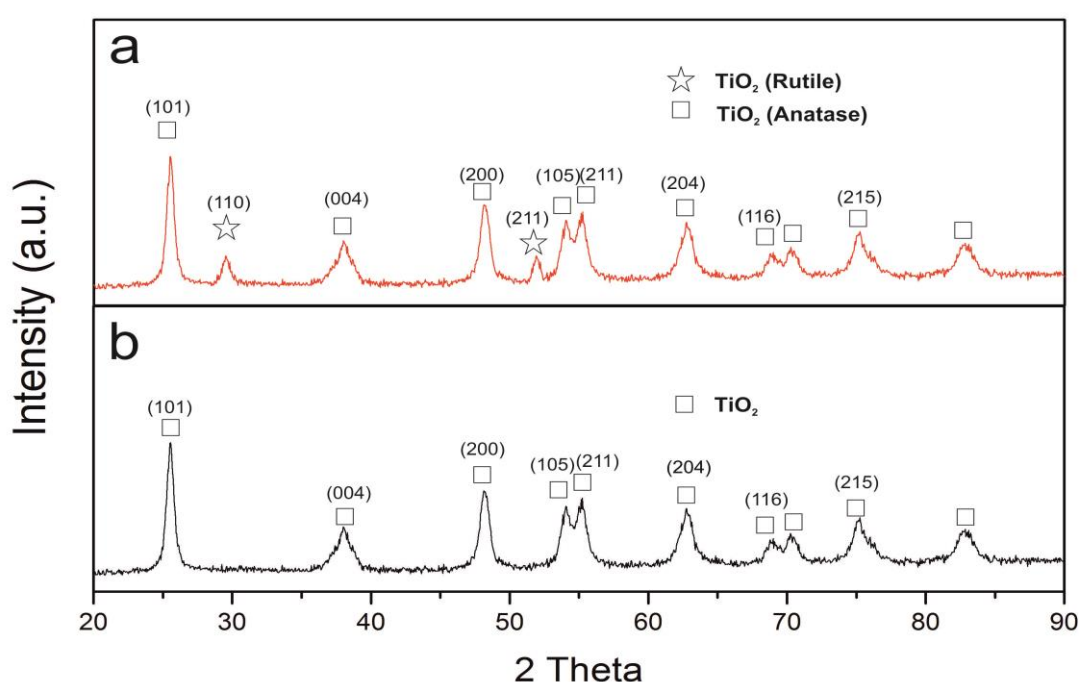


**Figure 7.4** Indexed XRD patterns of undoped  $\text{TiO}_2$  particles (a) compared to Zr doped  $\text{TiO}_2$  particles (b).

Figure 7.4.a shows XRD diffraction pattern of  $\text{TiO}_2$  scattering layer films annealed at a temperature of  $500^\circ\text{C}$ . XRD results indicate that crystal structure of  $\text{TiO}_2$  powders show anatase (JCPDS: 21-1272) and rutile phases (JCPDS: 76-1940). On the contrary, after 10 % Zr addition, there was no rutile phase as observed in Figure 7.4.b. While rutile is more stable and abundant in nature, in nanoscale photo-generation, anatase is more effective. Zr addition on  $\text{TiO}_2$  delays the formation of rutile phases. 10% Zr addition does not have any effect on anatase structure of  $\text{TiO}_2$  which matches up with JCPDS no. 21-1272.  $\text{ZrO}_2$  phases were not detected in XRD.

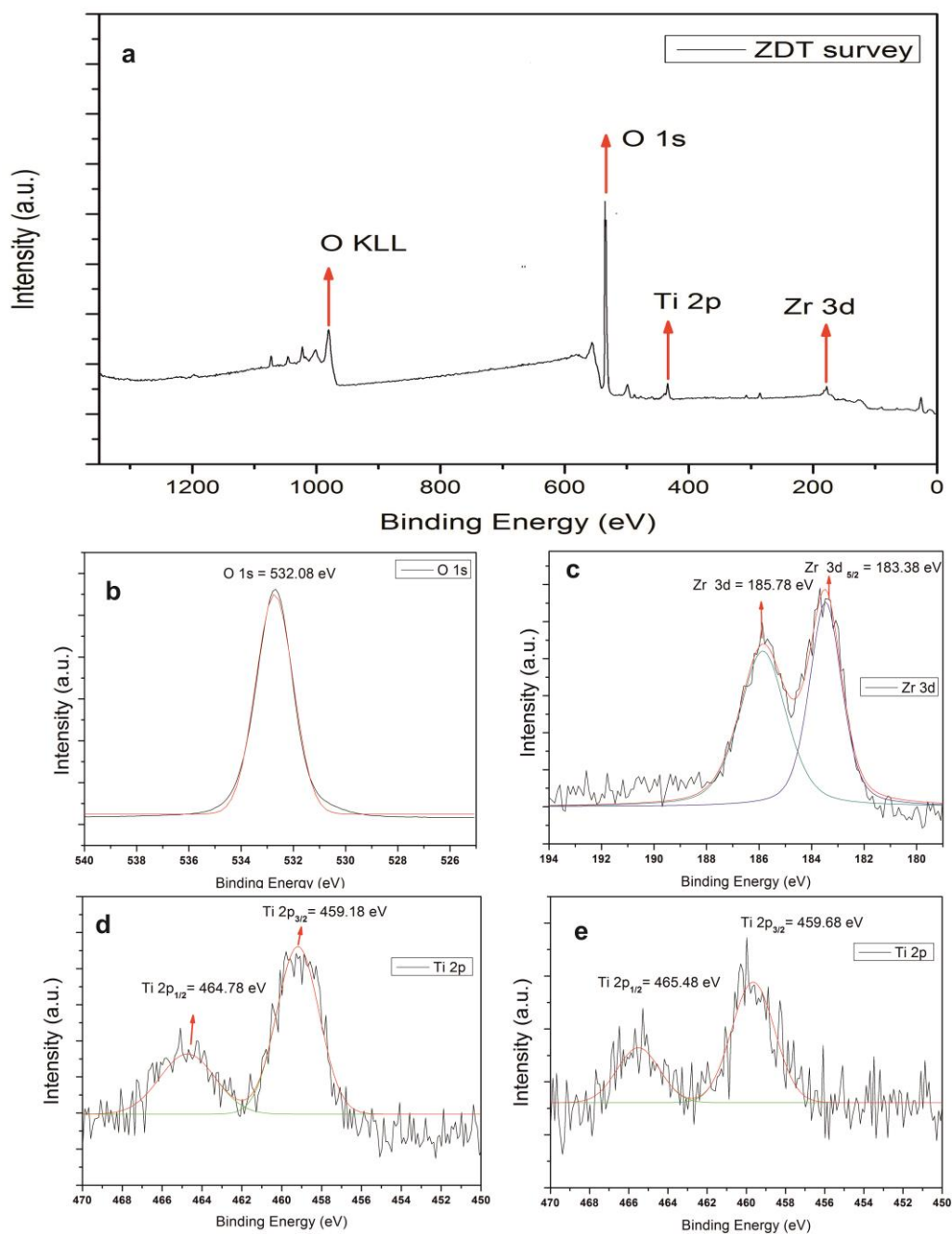


**Figure 7.5** XPS survey spectrum of ZDT photo electrode (a) and high-resolution XPS spectrum of O 1s peak (b), Zr 3d peak (c), and comparison of T-SL Ti 2p peak (d) and ZDT-SL Ti 2p peak (e).

X-ray photoelectron spectroscopy (XPS) is surface-sensitive quantitative spectroscopic analyses that the elemental composition, empirical formula, chemical state and electronic state of the material are analysed by a beam of X-rays. Figure 7.5.a

shows the XPS spectrum of ZDT scattering film. Figure 7.5.b demonstrates the high-resolution XPS spectrum of the O 1s, belonging to ZDT scattering film. One peak is located at 532.08 eV after fitting of the curve that is assigned to lattice oxygen (O–Ti). The high resolution XPS spectrum of Ti 2p observed in Figure 7.5.e shows two peaks at 459.68 eV and 465.48 eV, which can be assigned to the oxidation core levels of  $Ti^{4+}$  2p<sub>3/2</sub> and  $Ti^{4+}$  2p<sub>1/2</sub> for ZDT, respectively. Peaks of  $Ti^{4+}$  2p<sub>3/2</sub> and  $Ti^{4+}$  2p<sub>1/2</sub> oxide core levels for undoped  $TiO_2$  are at 459.18 eV and 464.78 eV in Figure 7.5.d. The binding energy was shifted towards the higher energy state. This can be illustrated with Zr doping effect at the chemical states of  $TiO_2$  matrix. In addition, spin-orbit split doublet peaks were identified in Figure 7.5.c at 183.38 eV and 185.78 eV belonging to the Zr 3d 5/2 and Zn 3d 3/2 electron sites, respectively. To summarize the effect of XPS and XRD, no  $ZrO_2$  was seen in XRD pattern, in addition, XPS is a clue that all Zr is doped into  $TiO_2$  lattice. ZDT particles are excellent samples for successfully doped  $TiO_2$  particles produced by hydrothermal process.

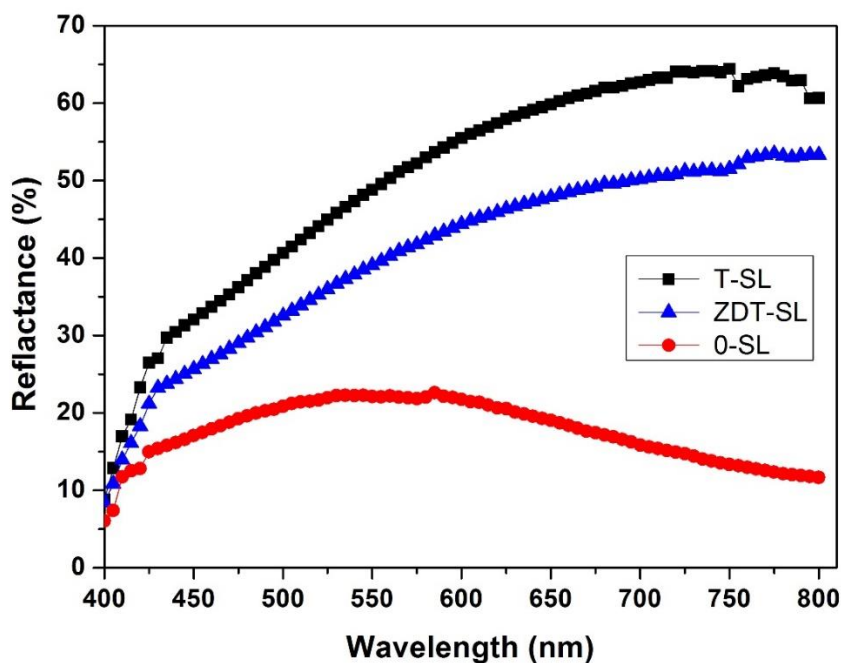


**Figure 7.6** Diffuse reflectance spectra of the photoanode without dye loading.

The reflectance spectra of different composite photoanodes without dye loading are presented in Figure 7.6. The reflectance of samples increases with the use of scattering

layer on top of the absorber layer. An essential improvement has been determined on reflectance parameters after applying ZDT scattering layer. A maximum reflectance of more than 65% was observed in the case of TiO<sub>2</sub> scattering layer (T-SL), whereas about 22% reflectance was found for the sample without scattering layer (0-SL). TiO<sub>2</sub> scattering layer (ZDT-SL) modified with zirconium has moderate performance in reflectance analysis, nearly 52%, due to having smaller particle sizes than T-SL. Smaller particles are known to decrease the reflectance of materials. Nevertheless, decreasing the particle sizes on scattering layer protects or improves dye loading capacity of photoanode. If scattering layer does not have a negative effective on dye loading capacity, it could improve the photo generation to enhance highly efficient dye sensitized solar cell. The dye loading capacity is given in Table 7.1. ZDT-SL DSSC photoanode has the best dye loading capacity, the more dye absorption means the more photo generation. The dye capacity of ZDT-SL DSSC photoanode is  $1.85 \times 10^{-7}$  mol/cm<sup>2</sup> while 0-SL DSSC photoanode is  $1.68 \times 10^{-7}$  mol/cm<sup>2</sup>.

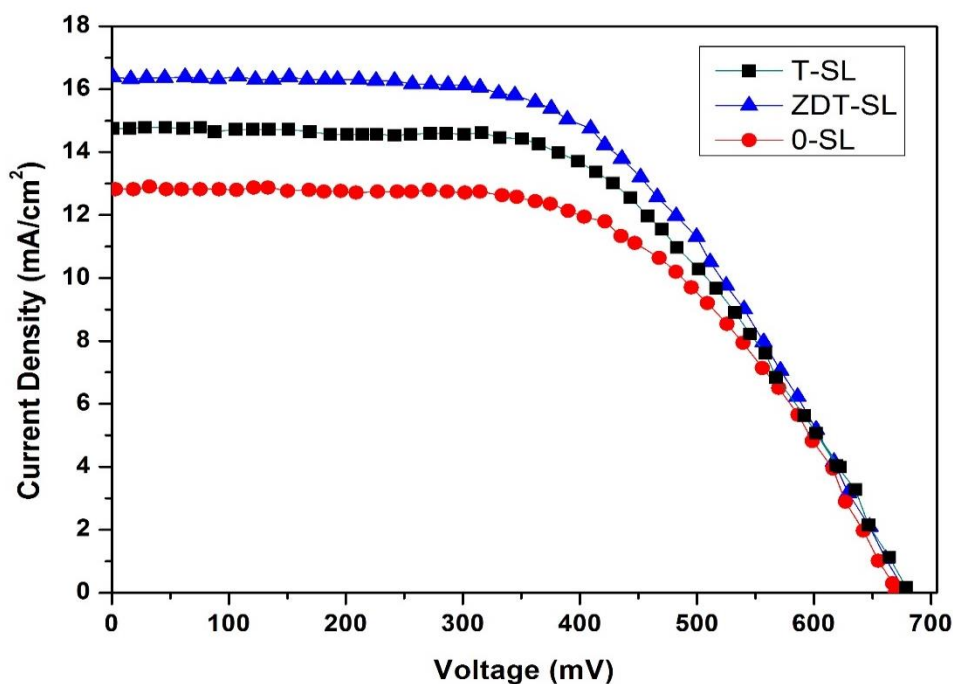


**Figure 7.7** Current density-voltage characteristics of devices with T-SL, ZDT-SL and 0-SL electrodes.

The T-SL DSSC photoanode has a dye loading capacity 30% less than ZDT DSSC photoanode. This positive effect of dye loading capacity was also observed on

photovoltaic measurements. The results of the current density-voltage (J-V) curves are given below in Table 7.1 and J-V characteristic curves are shown in Figure 7.7. The best improvement is found as 16.38 mA/cm<sup>2</sup> in DSSC with ZDT scattering layer. However, with 0-SL and T-SL, it is found to be 12.81 mA/cm<sup>2</sup> and 14.75 mA/cm<sup>2</sup>, respectively. All of the samples have nearly same Voc. The best photon to current conversion efficiency (6.03 %) is obtained by ZDT-DSSC sample while 0-SL sample only yields 4.98 % efficiency. The highest efficiency obtained in ZDT-DSSC sample can be explained by several reasons. First of all, the light-scattering ability of the ZDT particles could improve the light absorption by confinement and a longer path length of light within the TiO<sub>2</sub> film. It was leading to an improvement in dye excitation, which effects electron transport efficiency and reduces rates of recombination. The second reason is given that ZDT could play an active role on photoelectron generation directly. The third reason is that ZDT has positive effect on dye loading process.

**Table 7.1** Efficiency analysis of devices with T-SL, ZDT-SL and 0-SL electrodes.

<b>Sample Name</b>	<b>Thickness μm</b>	<b>Dye Absorption (10<sup>-7</sup> mol/cm<sup>2</sup>)</b>	<b>J<sub>sc</sub> (A/cm<sup>2</sup>)</b>	<b>V<sub>oc</sub> (mV)</b>	<b>FF (%)</b>	<b>η (%)</b>
<b>T-SL</b>	11.2	1.42	14.75	678	55.6	5.58
<b>ZDT-SL</b>	11.3	1.85	16.38	681	54.1	6.03
<b>0-SL</b>	7.6	1.68	12.81	669	57.9	4.98

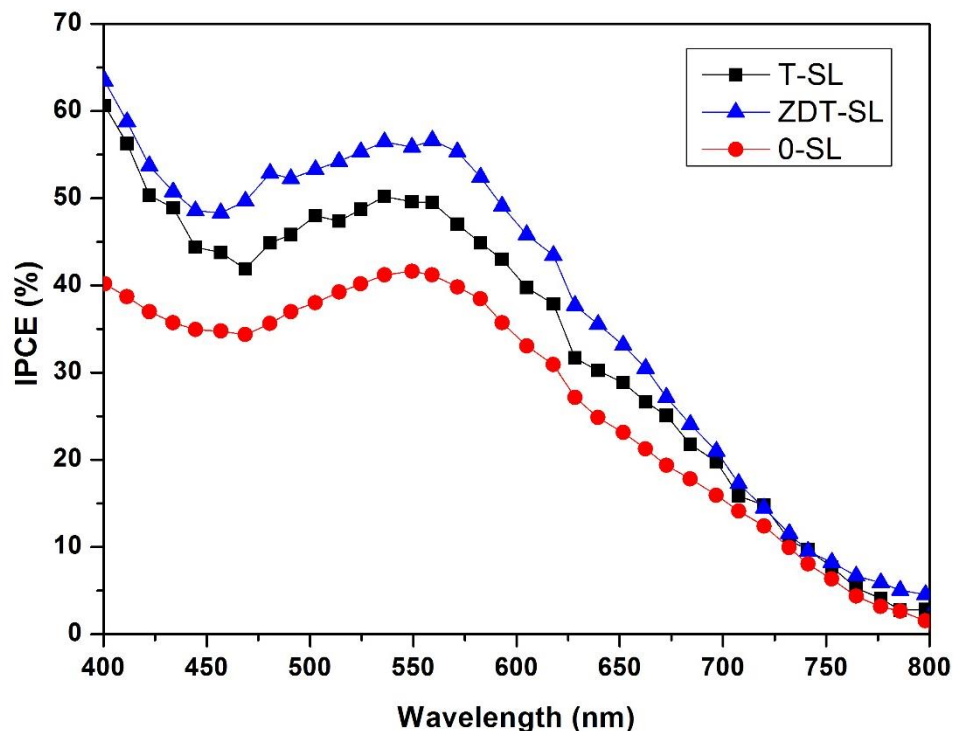


**Figure 7.8** Incident photon-to-current efficiency measurements of devices with T-SL, ZDT-SL and 0-SL electrodes.

Incident photon-to-current efficiency (IPCE) curves are given in Figure 7.8 to better understand photo sensitization of the different photo-electrodes and provide more evidence for the scattering effect at the given wavelength. Both T-SL and ZDT-SL cells showed significant increase in IPCE over the long-wavelength range (530–750 nm) compared with the reference cell 0-SL. This enhancement is a consequence of the scattering effect of Zr doped TiO<sub>2</sub> particles in ZDT DSSC and the sub-micrometer-sized mesoporous TiO<sub>2</sub> particles in T-SL. Although T-SL has a strong back-scattering effect, the ZDT-SL DSSC cell had a bit higher IPCE than the T-SL cell in the long-wavelength range. The ZDT has positive effect on dye loading amounts than that of T-SL photoanode. In addition, ZDT acts as a successful scattering layer on TiO<sub>2</sub> absorber layer. Consequently, ZDT has higher IPCE values at both long and short wavelengths.

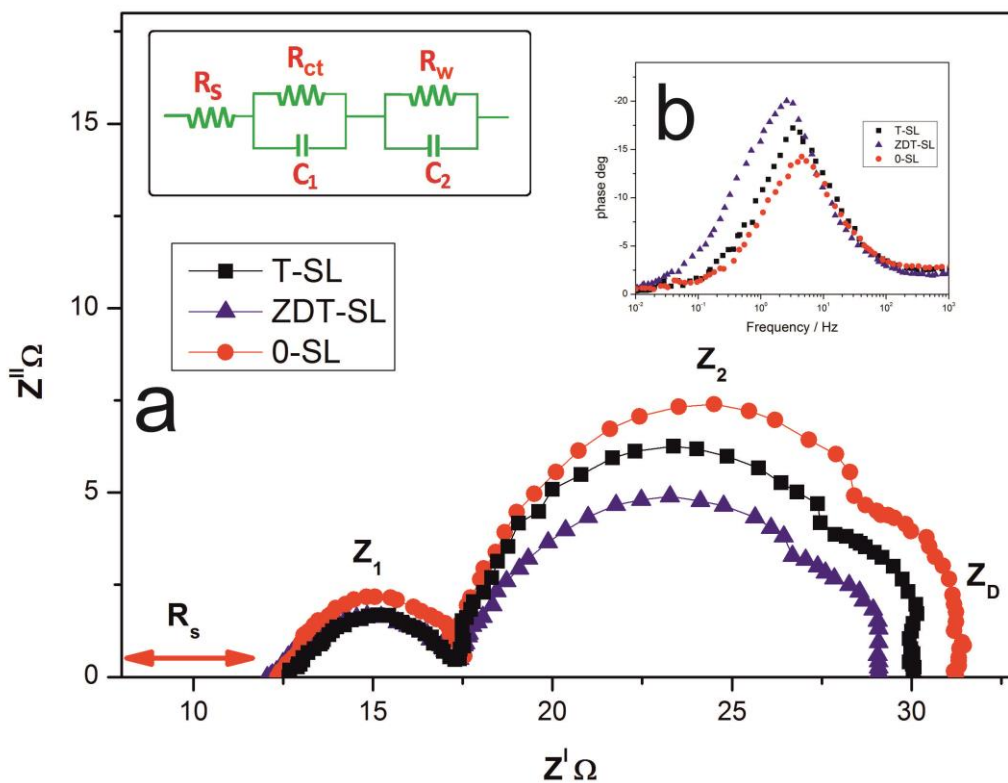


**Figure 7.9** EIS spectra of the solar cells fabricated using 0-SL, T-SL and ZDT-SL photoanode: Nyquist (a) and Bode (b) plots.

EIS technique has been widely employed to investigate the kinetics of electrochemical and photo electrochemical processes occurring in DSSCs. The impedance spectra of ZDT-SL, T-SL and 0-SL were given in Figure 7.9. The experiments were conducted under illumination ranging from 0.1 Hz to 100 kHz at  $V_{oc}$  values 678 mV for T-SL, 681 mV for ZDT-SL and 669 mV for 0-SL. On the Nyquist plots of EIS spectra (Figure 7.9.a), two semicircles were observed. A small semicircle, which has a frequency range lower than 0.1 MHz, represents high frequency region ( $Z_1$ ). Small semicircle was linked to interfaces between Pt counter electrode/iodine charge transfer resistances ( $R_{ct}$ ). On the low frequency region ( $Z_2$ ) second semicircle was observed. The second semicircle was linked to a constant phase element and transport resistance ( $R_w$ ) of the injected electrons accumulation within photoanode film and the charge transfer in either the photoanode/iodine electrolyte or ITO/photoanode interface. On the light of EIS model analysis performed by the help of Zsimpwin software, values of important kinetic parameters in the DSSC were issued in Table 7.2. ZDT-SL gives the best performance among all cells. It has low  $R_w$  resistance value, which means the

existence of the most efficient charge transfer process in all charge interface network on the cell. No significant difference was observed for Rct resistance values.

**Table 7.2** Kinetic parameters of devices with T-SL, ZDT-SL and 0-SL electrodes

<b>Samples</b>	<b>Rs (<math>\Omega</math>)</b>	<b>Rct (<math>\Omega</math>)</b>	<b>Rw (<math>\Omega</math>)</b>	<b><math>f_{\max}</math> (Hz)</b>	<b><math>\tau_e</math> (ms)</b>
0-SL	12.41	5.39	14.73	4.12	35.64
T-SL	12.58	5.88	12.58	3.48	45.72
ZDT-SL	12.34	5.05	11.31	3.01	52.90

On the Bode phase plot of EIS spectra, in Figure 7.9.b, frequency of charge transfer process at different photoanodes were shown in frequency versus theta (angle) graph. The characteristic low frequency peaks ( $f_{\max}$ ) are located at 4.12 Hz for 0-SL and 3.48 Hz for T-SL and 3.01 Hz for ZDT-SL. The most important parameter affecting the efficiency of electron life time for recombination and diffusion length at photoanode can be calculated from Bode plot characteristic peak from  $f_{\max}$  value equation of ( $\tau=1/2\pi f_{\max}$ ) in reference to Table 7.2. The  $f_{\max}$  of the DSSC with ZDT-SL photoanode was shifted from 4.12 Hz to 3.01 Hz, which corresponds to a longer electron lifetime as 52.90 ms. The highest electron life time can be defined as highest electron mobility, most fluently photo generated electron transportation and less recombination on DSSC. Highest electron mobility could bring about enhanced Jsc in devices based on ZDT-SL photoanode.

#### **7.4. Conclusion**

Dye sensitized solar cell (DSSC) has attracted researchers as it is a highly efficient, low-cost way to produce photovoltaic cell. For many years, TiO<sub>2</sub> and ZnO absorber nanomaterials such as nanoparticles, nanowires and nanotubes and the organometallic ruthenium dye families such as N719, N3 and C101 are well known most efficient

materials to obtain highly efficient photoanodes. However, the maximum conversion efficiency of DSSC has a barrier around 10% recorded. To alter this barrier, the scattering layer, which is a new subject matter to extend the light path, is performed to enhance the light harvesting efficiency. The suitable scattering layer has different characteristics than absorber layer such as higher particle size ( $>100$  nm) and it should not have any reducing effect on dye loading characteristics of absorber layer. Nevertheless, traditional scattering layers reduce the dye loading capacity of the absorber layer which is a challenge to achieve highly efficient cells. In this study, 10% Zr doped  $\text{TiO}_2$  (ZDT) has been synthesized by hydrothermal method and used as a scattering layer to improve photo conversion efficiency of DSSC. Average size of ZDT is found as 300 nm by SEM. 25% total improvement on photovoltaic efficiency and highest IPCE value have been obtained using ZDT scattering layer (ZDT-SL) compared to traditional DSSC. Surprisingly 5% improvement has been seen on dye loading capacity of photoanode. Positive improvements were observed on lifetime measurements by Electrochemical Impedance Spectroscopy (EIS). Recombination time is approximately doubled by the application of ZDT scattering layer. In addition, ZDT-SL has higher diffusion length than conventional DSSC. In the light of this study, ZDT-SL can be an alternative material for scattering layer applications for highly efficient dye sensitized solar cells.

## REFERENCES

1. Oregan, B. and M. Gratzel, *A Low-Cost, High-Efficiency Solar-Cell Based on Dye-Sensitized Colloidal TiO<sub>2</sub> Films*. *Nature*, **353**(6346): p. 737-740. 1991.
2. Gao, F., et al., *Enhance the optical absorptivity of nanocrystalline TiO<sub>2</sub> film with high molar extinction coefficient ruthenium sensitizers for high performance dye-sensitized solar cells*. *Journal of the American Chemical Society*, **130**(32): p. 10720-10728. 2008.
3. Nazeeruddin, M.K., et al., *Raman Characterization of Charge-Transfer Transitions in Ligand-Bridged Binuclear Polypyridyl Complexes of Ruthenium(II)*. *Journal of the Chemical Society-Dalton Transactions*, (2): p. 323-325. 1993.
4. Kern, R., et al., *Long term stability of dye-sensitised solar cells for large area power applications*. *Opto-Electronics Review*, **8**(4): p. 284-288. 2000.
5. Dai, S., et al., *Dye-sensitized solar cells, from cell to module*. *Solar Energy Materials and Solar Cells*, **84**(1-4): p. 125-133. 2004.
6. Anderson, N.A. and T. Lian, *Ultrafast electron injection from metal polypyridyl complexes to metal-oxide nanocrystalline thin films*. *Coordination Chemistry Reviews*, **248**(13-14): p. 1231-1246. 2004.
7. Gratzel, M., *Solar energy conversion by dye-sensitized photovoltaic cells*. *Inorganic Chemistry*, **44**(20): p. 6841-6851. 2005.
8. Nazeeruddin, M.K., et al., *Investigation of sensitizer adsorption and the influence of protons on current and voltage of a dye-sensitized nanocrystalline TiO<sub>2</sub> solar cell*. *Journal of Physical Chemistry B*, **107**(34): p. 8981-8987. 2003.
9. Wang, P., et al., *A new ionic liquid electrolyte enhances the conversion efficiency of dye-sensitized solar cells*. *Journal of Physical Chemistry B*, **107**(48): p. 13280-13285. 2003.

10. Ito, S., et al., *Fabrication of thin film dye sensitized solar cells with solar to electric power conversion efficiency over 10%*. Thin Solid Films, **516**(14): p. 4613-4619. 2008.
11. Cameron, P.J., L.M. Peter, and S. Hore, *How important is the back reaction of electrons via the substrate in dye-sensitized nanocrystalline solar cells?* Journal of Physical Chemistry B, **109**(2): p. 930-936. 2005.
12. Stangl, R., J. Ferber, and J. Luther, *On the modeling of the dye-sensitized solar cell*. Solar Energy Materials and Solar Cells, **54**(1-4): p. 255-264. 1998.
13. Yen, C.Y., et al., *Preparation and properties of a carbon nanotube-based nanocomposite photoanode for dye-sensitized solar cells*. Nanotechnology, **19**(37). 2008.
14. Burke, A., et al., *The function of a TiO<sub>2</sub> compact layer in dye-sensitized solar cells incorporating "Planar" organic dyes*. Nano Letters, **8**(4): p. 977-981. 2008.
15. Barbe, C.J., et al., *Nanocrystalline titanium oxide electrodes for photovoltaic applications*. Journal of the American Ceramic Society, **80**(12): p. 3157-3171. 1997.
16. Ferber, J. and J. Luther, *Computer simulations of light scattering and absorption in dye-sensitized solar cells*. Solar Energy Materials and Solar Cells, **54**(1-4): p. 265-275. 1998.
17. Nitz, P., et al., *Simulation of multiply scattering media*. Solar Energy Materials and Solar Cells, **54**(1-4): p. 297-307. 1998.
18. Tennakone, K., et al., *The possibility of ballistic electron transport in dye-sensitized semiconductor nanocrystalline particle aggregates*. Semiconductor Science and Technology, **14**(11): p. 975-978. 1999.
19. Usami, A., *Rigorous solutions of light scattering of neighboring TiO<sub>2</sub> particles in nanocrystalline films*. Solar Energy Materials and Solar Cells, **59**(3): p. 163-166. 1999.
20. Usami, A., *Theoretical simulations of optical confinement in dye-sensitized nanocrystalline solar cells*. Solar Energy Materials and Solar Cells, **64**(1): p. 73-83. 2000.

21. Usami, A., *A theoretical simulation of light scattering of nanocrystalline films in photoelectrochemical solar cells*. Solar Energy Materials and Solar Cells, **62**(3): p. 239-246. 2000.
22. Yoon, J.H., et al., *TiO<sub>2</sub> nanorods as additive to TiO<sub>2</sub> film for improvement in the performance of dye-sensitized solar cells*. Journal of Photochemistry and Photobiology a-Chemistry, **180**(1-2): p. 184-188. 2006.
23. Ferber, J., et al., *Internal reflection mode scanning near-field optical microscopy with the tetrahedral tip on metallic samples*. Applied Physics a-Materials Science & Processing, **69**(6): p. 581-589. 1999.
24. Ferber, J., R. Stangl, and J. Luther, *An electrical model of the dye-sensitized solar cell*. Solar Energy Materials and Solar Cells, **53**(1-2): p. 29-54. 1998.



## CHAPTER 8

### CONCLUSION AND SUGGESTIONS

During this work, each of photoanode parts was successfully constructed. The effect on photovoltaic properties of each photoanode was investigated. The crucial outputs can be summarized as given below.

- As conclusion, of TCO parts of photoanode, in this study, an alternative path of producing highly transparent and lower resistance ITO by sol gel method and application on DSSC was shown. Temperature resistant, highly transparent ITO films having a well oriented structure, better optical and electrical characteristics were investigated. 300 nm ITO film shows the best performance for the DSSC applications. Moreover, 300 nm ITO photoanode exhibited better IPCE, probably due to the improvement of photon harvesting. These results indicate that 300 nm ITO coated glass substrate is an alternative transparent conductive glass material for application in dye-sensitized solar cell.
- Semiconductor metal oxide nanowires (SCMONWs), favorable materials for various quantum devices having one dimensional (1D) interaction and large surface to volume ratio, were synthesized by a novel technique. The sol-gel technique can be an alternative production method for 1D materials. In this study, ITO nanopowders, nanowires and films on glass substrates (TCO) were successfully produced using sol-gel technique. ITO nanowire treatment between the conductive transparent ITO film and TiO<sub>2</sub> matrix improved photovoltaic efficiency. This efficiency increase is due to the increase in the

- Voc and Jsc values. In addition, from EIS measurements, it was understood that diffusion length and recombination time increase with 1D ITO treatment. Finally, highly efficient electron transport, improved conversion efficiency on dye sensitized solar cell and maximized performance of sol-gel based DSSC has been obtained by 1D ITO treatment.
- The recombination reactions at FTO/electrolyte and TiO<sub>2</sub>/electrolyte interfaces were investigated using two surface passivation approaches of ZrO<sub>2</sub> and TiO<sub>2</sub> layers using hydrothermal deposition method in DSSCs. The photovoltaic current characteristics and open-circuit voltage behavior were investigated for coated and uncoated FTO surfaces. The recombination can be prevented using both TiO<sub>2</sub> and ZrO<sub>2</sub> blocking layers. On the other hand, ZrO<sub>2</sub> showed better performance than TiO<sub>2</sub> layer on reducing total recombination. ZrO<sub>2</sub> affects the electrical properties of FTO positively. Because ZrO<sub>2</sub> shows higher transparency than TiO<sub>2</sub> blocking layer, ZrO<sub>2</sub>/FTO photoanode exhibited better IPCE, probably due to the improvement of photon harvesting and electron collection efficiency caused by electron back transfer blocking effect. These results indicate that the blocking layer of the FTO surfaces using ZrO<sub>2</sub> treatment prevents the recombination substantially in the dye-sensitized solar cells.
- Zr doped TiO<sub>2</sub> particles (ZDT) synthesized by hydrothermal method help to delay formation of rutile which are unwanted phases in DSSC applications and obtain relatively smaller particles than bare TiO<sub>2</sub> particles (T-SL). Better dye absorption and longer electron life time have been obtained by devices with ZDT-SL. Jsc (16.38 mA/cm<sup>2</sup>) and IPCE (55 % at 550 nm) were remarkably increased. Although T-SL particles have higher reflectivity than ZDT-SL due to larger particles sizes, they showed moderate performance on scattering layer applications on DSSC. ZDT-SL based DSSC has 6.03 % efficiency while 0-SL has performed 4.98 % conversion efficiency. Compared to the traditional DSSC, using scattering layer on photoanode improves the light conversion efficiency. In this study, ZDT particles are found to be a candidate for scattering layer for highly efficient DSSC applications.

Finally, each part of photoanode modification increased the energy conversion efficiency of solar cells compared to commercial photoanodes. However, best efficiency harvested in this work is lower than in literature based on TiO<sub>2</sub> cells, which have commercial TCO produced by high vacuum processes. The fully sol-gel based DSSC was produced and it showed well performance on PV measurements. It has higher efficiency than the cells based on wet chemical methods in literature.

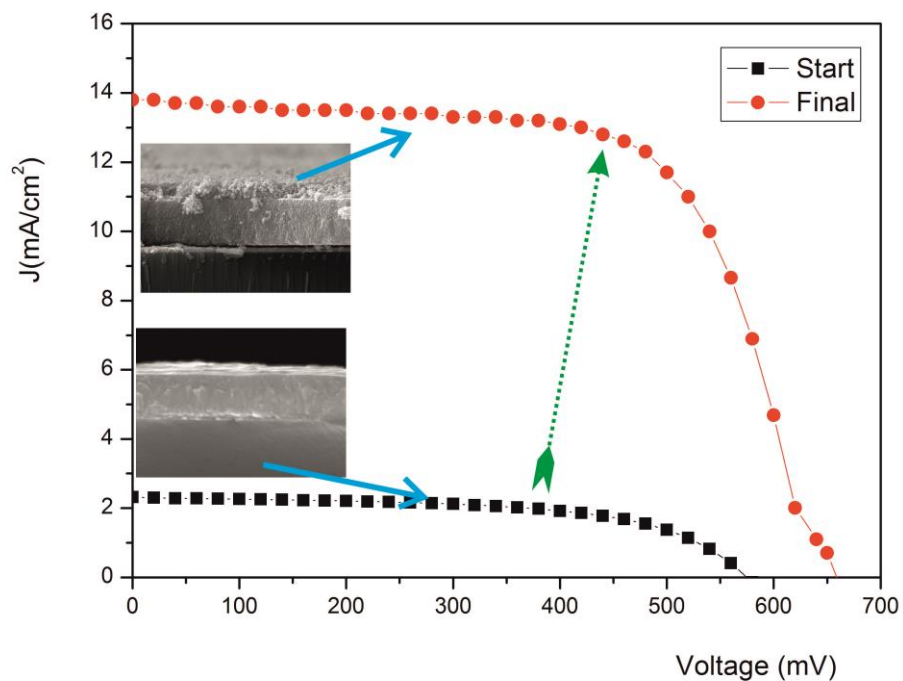


**Figure 8.1** Comparison between modified and classical photoanode PV performance results.

**Table 8.1** Final modeling results of Zr modified TiO<sub>2</sub> nanocomposite DSSC.

Transparent Conductive Layer	Blocking Layer	Absorber Layer	Scattering Layer	Efficiency (%)
FTO	ZrO <sub>2</sub>	5 % Zr-TiO <sub>2</sub>	10 % Zr- TiO <sub>2</sub>	7.45 %

Figure 8.1 summarizes keystone of this work. 1.02 % efficiency was obtained by single absorber layer, however 7.45 % efficiency was obtained by modification of photoanode at the end of the work. The efficiency can be increased by using much purer sensitizers which can absorb all of the sunlight spectrum. The phonon scattering or quantum dot sensitizers can be alternatives to reach higher efficiencies. The platinum catalyzer layer can be replaced by efficient cheaper catalyzers such as C60 or CNT to enhance higher efficiency/cost ratio

## . CURRICULUM VITAE

### PERSONAL INFORMATION

Surname, Name: Yavuz , H.İbrahim

Nationality: Turkish (TC)

Date and Place of Birth: 26 August 1981, Adana

Marital Status: Married

Phone: +90 312 210 59 17

Fax: +90 312 210 22 91

Email: yavuz @metu.edu.tr

### EDUCATION

Degree	Institution	Year of Graduation
<b>Ph.D.</b>	Metallurgical and Materials Engineering Middle East Technical University, Ankara, TURKEY	2014
<b>MS</b>	Department of Chemistry Education Çukurova University, Adana, TURKEY	2004
<b>BS</b>	Department of Chemistry Çukurova University, Adana, TURKEY	2003
<b>High School</b>	Adana 5 Ocak High School, Adana	1998

## WORK EXPERIENCE

**Research Assistant** 2006- 2014

METU Department of Metallurgical and Materials Engineering Middle East  
Technical University, Ankara, TURKEY

## FOREIGN LANGUAGES

English

## PUBLICATIONS

### Thesis

- **Halil Ibrahim Yavuz**, PhD Thesis, METU, September 2014 Design of High-Efficiency Dye-Sensitized Nanocrystalline Solar Cells

### Journal Articles

1. Icli, K.C., **Yavuz, H.I.**, Ozenbas, M. , Production of core-shell type conducting FTO/TiO<sub>2</sub> photoanode for dye sensitized solar cells , Journal of Solid State Chemistry, Volume 210, 2013, Pages 22-29
2. Cosar, B., Icli, K.C., **Yavuz, H.I.**, Ozenbas, M. ,Photovoltaic performance of bifacial dye sensitized solar cell using chemically healed binary ionic liquid electrolyte solidified with SiO<sub>2</sub> nanoparticles, Electrochimica Acta, Volume 87, 1 January 2013, Pages 425-431
3. Ghaffari, M., Cosar, M.B., **Yavuz, H.I.**, Ozenbas, M., Okyay, A.K., Effect of Au nano-particles on TiO<sub>2</sub> nanorod electrode in dye-sensitized solar cells, Electrochimica Acta, Volume 76, 1 August 2012, Pages 446-452
4. Irmak, S., **Yavuz, H.I.**, Erbatur, O., Degradation of 4-chloro-2-methylphenol in aqueous solution by electro-Fenton and photoelectro-Fenton processes,

Applied Catalysis B: Environmental, Volume 63, Issue 3-4, 31 March 2006, Pages 243-248

5. Kusvuran, E., Irmak, S., **Yavuz, H.I.**, Samil, A., Erbatur, O., Comparison of the treatment methods efficiency for decolorization and mineralization of Reactive Black 5 azo dye, Journal of Hazardous Materials, Volume 119, Issue 1-3, 17 March 2005, Pages 109-116
6. Kusvuran, E., Gulnaz, O., Irmak, S., Atanur, O.M., **Yavuz, H.I.**, Erbatur, O. Comparison of several advanced oxidation processes for the decolorization of Reactive Red 120 azo dye in aqueous solution , Journal of Hazardous Materials, Volume 109, Issue 1-3, 18 June 2004, Pages 85-93

### Conference Papers (International)

1. **Halil Ibrahim Yavuz**, Ahmet Macit Ozenbas, The Efficiency Improvement in DSSCs by the Utilization of Indium Tin Oxide Nanowire Transparent Film Electrode Produced by Sol-Gel Method, SS19.59, *2013 MRS Fall Meeting & Exhibit*, (2013), Boston, Massachusetts, USA
2. **H. İ. Yavuz**, M. Ozenbas, Production and comparison of fully solution based 1D-2D-3D (ITO-TiO<sub>2</sub>) composite dye sensitized solar cell. "*26th European Photovoltaic Solar Energy Conference*", (2011), p.551-553, Hamburg, GERMANY
3. B. Cosar , **Halil I. Yavuz** and Ahmet M. Ozenbas, The Development of Bifacial Dye Sensitized Solar Cells Based on Solid Electrolyte J7.25, *2011 MRS Fall Meeting & Exhibit*, November 28 - December 2, (2011), Boston, Massachusetts, USA
4. **Halil I. Yavuz**, Mustafa B. Cosar and Ahmet M. Ozenbas, Preparation of TiO<sub>2</sub>-ZrO<sub>2</sub> Mixed Oxide Electrode for Dye Sensitized Solar Cells. . J7.27, *2011 MRS Fall Meeting & Exhibit*, November, (2011), Boston, Massachusetts, USA
5. Kerem C. Icli, **Halil I. Yavuz** and Ahmet M. Ozenbas; Core-Shell Type Nanocrystalline FTO Photoanodes for Dye Sensitized Solar Cells. J7.28, *2011 MRS Fall Meeting & Exhibit*, (2011), Boston, Massachusetts, USA
6. **Halil Ibrahim Yavuz** and Ahmet M. Ozenbas Application of Indium Tin Oxide Nanowires, Nanopowders and Thin Films for Dye Sensitized Solar

Cells. ; MM6.19, *2010 MRS Fall Meeting & Exhibit November* , (2010), Boston, Massachusetts, USA.

7. **Halil I. Yavuz** and Ahmet M.\_The Effect of Cation Modification on TiO<sub>2</sub> Nanoparticles for Dye Sensitized Solar Cells. Ozenbas. N7.34, Colloidal Nanoparticles for Electronic Applications--Light Emission, Detection, Photovoltaics, and Transport, *MRS 2009 Fall*, (2009), Boston, Massachusetts, USA.
8. **Halil I. Yavuz** and Ahmet M. Ozenbas, Production of Semiconductor Indium Tin Oxide (ITO) Nanowires by Sol-Gel Technique. , Symposium BB: Green Chemistry in Research and Development of Advanced Materials, *MRS 2009 Fall*, AM BB3.8 November 30 - December 4, (2009), Boston, Massachusetts, USA
9. **H. İ. Yavuz**, M. Özenbaş, Production of Metal Oxide Nanoparticles for Dye-Sensitized Solar Cells."Materials Research Society, Fall Meeting (December 1-5, 2008), Abstract Book", (2008), p.PP9.22, Boston, Massachusetts, USA
10. **H. İ. Yavuz**, M. Özenbaş, Production of Metal Oxide Nanoparticles for Dye-Sensitized Solar Cells."International Workshop on Advanced Materials and Devices for Photovoltaic Applications, *NANOMAT 2008*", (2008), p.41.

### Conference Papers (National)

1. **H.İ. Yavuz**, M. Özenbaş, The application of new type ZrO<sub>2</sub> modified TiO<sub>2</sub> inorganic nano-composite materials for dye sensitized solar cells. "8. *Nanobilim ve Nanoteknoloji Kongresi*", (2012), s.61
2. **H.İ.Yavuz**, M. Özenbaş, Improvement of photovoltaic efficiency on dye sensitized solar cells by Zr based cation modified layers. "*SolarTR-2 Solar Electricity Conference*", (2012), s.74.
3. M. Burak Coşar, **H. İbrahim Yavuz**, A. Macit Özenbaş, The Design of Nanocrystalline SnO<sub>2</sub> Dye Sensitized Solar Cell. "*SolarTR-1 Turkish Solar Energy Conference*", , (2010), s.62.

4. Onur Dinçer, **H. İbrahim Yavuz**, A. Macit Özenbaş, The Effect of ZnO Quantum Dot Modification on Dye Sensitized Solar Cells. "*SolarTR-1 Turkish Solar Energy Conference*",(2010), s.59.
5. **H. İbrahim Yavuz**, A. Macit Özenbaş, Production of ITO Nanoparticles, Nanowires and Thin Films for Dye Sensitized Solar Cells. "*Proceedings of 15 the International Metallurgy and Materials Congress*", (2010), s.181-186.
6. **H. İbrahim Yavuz**, A. Macit Özenbaş, Preparation of ITO/TiO<sub>2</sub> Nanocomposite Structures for Dye Sensitized Solar Cells. "*Solar TR-1 Turkish Solar Energy Conference*", (2010), s.60
7. **H. İ. Yavuz**, M. Özenbaş, Production of Metal Oxide Nanoparticles for Dye-Sensitized Solar Cells. "*14 th International Metallurgy and Materials Congress IMMC 2008 Congress e-Book*, (2008), s.830-838.

## **HOBBIES**

Scuba, Movies, Motor Sports, Football, Camping